Simulating the differentiation of stem cells

using a 2D and 3D mathematical model

S.D. Harrevelt

Technische Universiteit Delft

TU Delft Delft University of Technology

Challenge the future

SIMULATING THE DIFFERENTIATION OF STEM CELLS

USING A 2D AND 3D MATHEMATICAL MODEL

by

S.D. Harrevelt

in partial fulfillment of the requirements for the degree of

Master of Science
in Applied Mathematics

at the Delft University of Technology,
to be defended publicly on Wednesday May 20, 2015 at 15:00 AM.

Supervisor:	Dr. ir. F.J. Vermolen	
Thesis committee:	Prof. dr. ir. C. Vuik,	TU Delft
	Dr. ir. W. T. van Horssen,	TU Delft

This thesis is confidential and cannot be made public until May 15, 2015.

An electronic version of this thesis is available at http://repository.tudelft.nl/.

TU Delft Delft University of Technology

PREFACE

After a figurative nine month long roller-coaster ride, with many highs and lows, cork screws and loops, the cart has slowed down and is in need of a little rest. It was unexpected how much I learned during these nine months, where I assumed that most of the time I would be doing some mind-numbing programming, the contrary actually happened. The exercise of thinking, visualizing and explaining mathematics has taught me how to process information and communicate about mathematics in an efficient way.
Now it is time for me to choose a different ride. The road before me is long, since I have only begun living compared to a more *experienced* human being. However, I would like to thank some people that have aided me to reach this point thus far.

First of all, I want to thank my parents for giving me the opportunity and confidence that I needed to get where I am today. Next up are my brother and sister who helped to distract me from my thesis work every now and then.

My supervisor, F.J. Vermolen, thank you for your continuous support and feedback on my writing skills, these have helped me immensely if I look back upon my earlier versions of this thesis.

Frans, we had a good time. Thanks for all the discussions, be it about mathematics, philosophy, politics or just random crabs. And I am glad that you shared such an exquisite taste in music.

Then at last, I would like to apologize to all of my friends for whom I could not spare as much time as I wanted to. Thanks for your understanding, hopefully we can all celebrate this in June.

S.D. Harrevelt
Delft, May 2015

Contents

1 Introduction **1**

2 Biology **3**
2.1 General cell biology . . . 3
2.1.1 Cell composition . . . 3
2.1.2 Cell movement . . . 5
2.1.3 Cell cycle . . . 6
2.1.4 Cell differentiation . . . 7
2.1.5 Stem cells . . . 7
2.2 Phenotypes . . . 9
2.2.1 Myogenesis - the myocyte . . . 9
2.2.2 Adipogenesis - the adipocyte . . . 12

3 Classical Models for cell populations and differentiation **13**
3.1 A mathematical model for cell differentiation - Pavel A. Prokharau . . . 13
3.2 An agent-based discrete model for cell populations . . . 14

4 A novel model approach for cell differentiation **17**
4.1 The cell . . . 18
4.2 The maturity . . . 20
4.2.1 Chemical signaling . . . 21
4.2.2 Mechanical signaling . . . 23
4.3 Cell movement . . . 27
4.3.1 Cell rotation . . . 28
4.4 Physiological change of the cell . . . 29
4.5 Parameter choice . . . 30
4.5.1 Model overview . . . 32

5 Results from the novel model approach in 2D **33**
5.1 Sensitivity analysis . . . 33
5.1.1 Secretion sensitivity analysis . . . 34
5.1.2 Force magnitude sensitivity analysis . . . 35
5.2 Position analysis . . . 41

6 Results from the novel model approach in 3D **43**
6.1 Sensitivity analysis . . . 43
6.1.1 Secretion sensitivity analysis . . . 45
6.1.2 Force magnitude sensitivity analysis . . . 45
6.2 Position analysis . . . 51

7 Discussion **53**

8 Future work **55**

A Appendix **57**
A.1 Derivation of the relation between stress and displacement . . . 57
A.2 The Finite Element Method . . . 59
A.3 Derivation of the the weak formulation of the mechanical model . . . 61
A.3.1 Elliptic problem . . . 64

A.4 Derivation of the (weak) formulation chemical model . . . 65
A.5 Fourier analysis on the mechanical signal . . . 68
A.6 The gradient recovery method . . . 69
A.7 Generalized novel model approach for arbitrary phenotypes . . . 72
A.8 Extension toward three dimensions . . . 73
A.8.1 Geometrical adaptations . . . 73
A.8.2 Cell force . . . 74
A.8.3 Cell movement . . . 74
A.8.4 Domain changes . . . 75
A.9 Validation of models . . . 76
A.9.1 Chemical model . . . 77
A.9.2 Mechanical model . . . 79
A.10 Comparing different source techniques . . . 81

Bibliography **85**

1

INTRODUCTION

In this thesis we propose a novel model approach to simulate the differentiation process of mesenchymal stem cells (MSC's). The reason to study the behavior of MSC's is because of their promising features in tissue engineering. With its mobility and differentiation properties, these cells are able to repair tissue in various parts of the body. Recent research has shown that stem cell injection in damaged cardiac tissue can improve damaged tissue [1][1].
With the abstraction ability of mathematics, a mathematical model could aid in stem cell research. By condensing the biological process in a mathematical model, the model could help in understanding the underlying mechanisms of (stem) cell differentiation, or could aid for educational purposes.
However, a mathematical model is as good as the knowledge about the subject which is being modeled. This is most definitely true in this case, since stem cell differentiation remains a complex process, which is not entirely understood yet [3]. Hence, it is a difficult task to present a model which simulates cell differentiation in a realistic manner, since among others, validation of the model by the use of biological experiments is challenging.
Then again, a reason to propose a mathematical model for cell differentiation is that they can reproduce an experiment very easily compared to biological experiments. Besides that, mathematical models are ethically neutral in contrast to biological experiments where one has to be concerned about these restrictions[2].

To model (stem) cell differentiation, we use an approach which is inspired by the paper of Prokharau [4], where (stem) cell differentiation is considered to be a gradual process whereby a cell obtains the characteristics of its phenotype gradually, and by the thesis of W.M. Boon [5]. As stated before, a bio-mathematical model is as good as the biological knowledge and choice of parameters. Hence, in order to produce a useful model we are compelled to expand our knowledge about cell biology, which will be presented in Chapter 2. After this introduction into cell biology, we will explore two models proposed by Prokharau and Macklin in Chapter 3.
The novel model approach will be presented in Chapter 4 which is *able* to simulate the differentiation towards p phenotypes. However, we will only simulate the differentiation towards two specific phenotypes, namely muscle and fat cells. Subsequently we give some preliminary results of the 2D version of the model in Chapter 5, and a preview of the results from the 3D version in Chapter 6. Hereafter we discuss the obtained results in more detail and point out parts of the model that can be improved in Chapter 7 and 8, respectively.

[1] However, another paper claims that this is not possible during *in vitro* studies at high frequencies [2]
[2] Take for example genetic modification, embryotic stem cell reasearch and cloning

2

BIOLOGY

In this chapter we will introduce the biological knowledge we have gained. We start by explaining the basics of a cell, which list properties like its composition, migration and proliferation.
From this introduction we will guide the reader through the stages of cell differentiation, where we will focus on the differentiation of mesenchymal stem cells towards fat and muscle cells since the differentiation process towards these two phenotypes is the main focus of this thesis.
In our novel model approach we attempt to simulate the differentiation of MSC towards adipocyte and myocyte, hence the gained biological knowledge is a key ingredient to form our model assumptions.

2.1. GENERAL CELL BIOLOGY

Cells are the building blocks of life, they are the smallest unit of life that can replicate independently. The whole population of cells can be divided into two classes, which are characterized by the presence or absence of a nucleus. The cells without a nucleus are called *prokaryotes* and cells with a nucleus are called *eukaryotes*. Prokaryotes are considered less complex than eukaryotes, mainly because it is assumed that eukaryotes are composed of evolved prokaryotes. Since stem-, fat-, and muscle cells are eukaryotes, we have no interest in the mechanisms behind prokaryotes in this thesis.

2.1.1. CELL COMPOSITION

Despite the small size of eukaryotic cells, ranging from a mere 10 - 100 μm, they are extremely complex. Looking from a molecular point of view, we can say that eukaryotes are composed of water, *inorganic* ions and *organic* molecules.
The total mass of a cell is for 70% made up of water. This is an important fact, because this helps with the formation of the cell membrane. The reason behind this, is that the water molecule is a polar molecule. The hydrogen atom of the water molecule has a small positive charge, whereas the oxygen atom is slightly negatively charged. This causes the water molecule to bind more easily to other polar molecules and ions and further it tends to minimize the contact with non-polar molecules. This interaction between molecules is an important factor in the formation of biological structures, such as cell membranes, since cell membranes are mainly composed of lipids that repel water.
About 1% of the mass in a eukaryote is caused by the *inorganic* ions, which include: Sodium, potassium, magnesium, calcium, phosphate, chloride and bicarbonate.
The *organic* molecules are the ingredients that make a cell unique. These molecules can be classified into four distinct classes

- Carbohydrates - provides the nutrients and energy storage in a cell.
- Nucleic acids - DNA and RNA, contain the blue print of the cell.
- Proteins - execute the 'blue print' of the nucleic acids.
- Lipids - provides energy storage, are a major component of cell membranes and used in cell signaling.

The carbohydrates, nucleic acids and proteins are considered macromolecules due to their size. These compounds are formed by joining (polymerization) of hundreds or thousands of low molecular-weight precursors: amino acids, nucleotides, and simple sugars. [6]

From a functional point of view, a cell is filled with cytoplasm that is bounded by a cell membrane, where the cytoplasm contains all the bound and unbound organelles, and the cytosol.
An important (unbound) organelle in the cytoplasm, is the cytoskeleton. This structure is, among others, responsible for the size and shape of the cell. We will see that the cytoskeleton is an elastic skeleton which deforms during cell movement and contraction.
One of the building blocks of the cytoskeleton is the protein actin, which is responsible for the formation of microfilaments inside a cell. Further, the protein actin can act as a track on which the protein myosin attaches to cause contraction in myocytes.
The cell membrane physically separates the intracellular components from the extracellular environment, hence the cell membrane is the connection between the (inner) cytoskeleton and the (outer) extracellular matrix (ECM).
This membrane is composed of lipids and proteins. The function of the lipids in the membrane, is to repel water-soluble molecules, while the proteins act as a mediator for ions and biological molecules. The weight distribution between the lipids and proteins is 50/50, since proteins are much larger than lipids, this ratio translates into one protein molecule per every 50-100 molecules of lipid.
The proteins that reside in the cell membrane can be divided in two classes - *peripheral* proteins and *integral membrane proteins*. Many integral proteins are also *trans-membrane proteins*, which span the lipid layer with portions exposed on both sides of the membrane. A special set of trans-membrane proteins are the integrins and the cadherins, which are considered *cell adhesion molecules*.

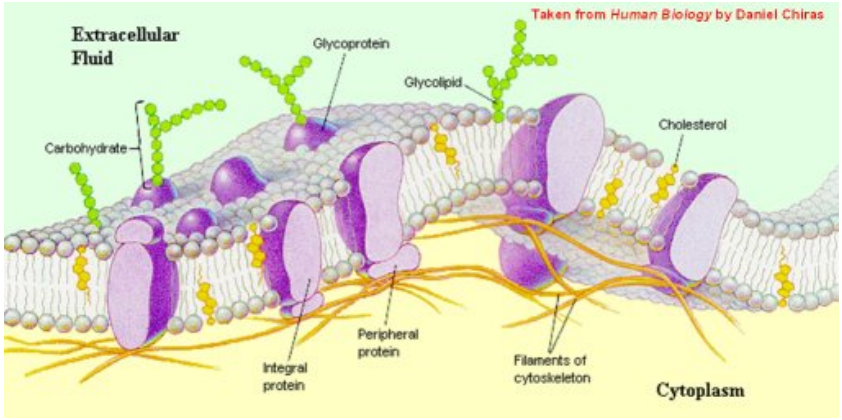

Figure 2.1: Abstract visualization of several membrane proteins

The integrins are responsible for the attachment of cells to the extracellular matrix and the cadherins are used in cell-cell adherence.
These proteins are used at focal adhesion points, which are large, dynamic protein complexes through which the cytoskeleton of a cell connects to the ECM. These integrins then bind to extra-cellular proteins via short amino acid sequences.
The formation behind focal adhesion is a complex process, where many different (trans-membrane) proteins are used. However, the core idea we can get from this, is that every cell has certain 'hooks' on which it grabs the ECM, or any other cell. Besides their mechanical functioning as 'hooks', the focal adhesions also serve as a chemical transmitter. However, note that these 'hooks' are far more complex than stated here.

2.1.2. CELL MOVEMENT

The mechanism behind cell-ECM adhesion is also used in the movement of a cell. It can be assumed that most animal cells use a crawl-like movement to migrate. This process of crawling can be summarized in four distinct steps, as shown in Figure 2.2

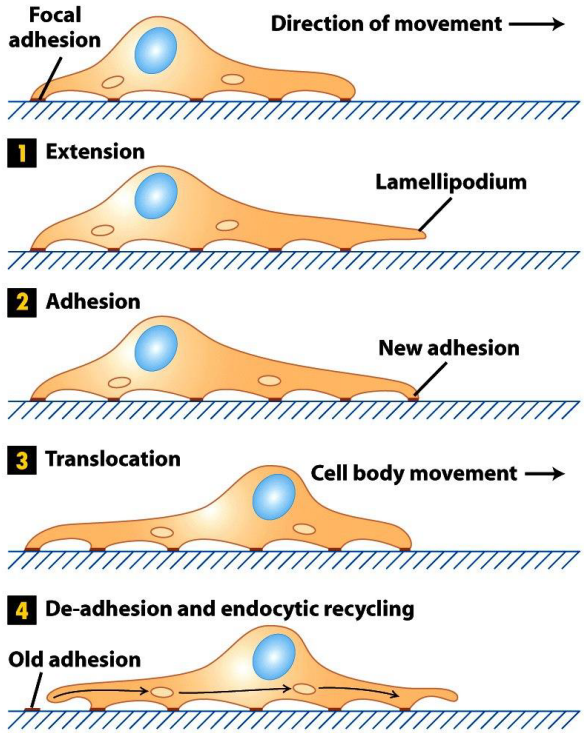

Figure 2.2: Abstract display of cell movement

A cell may undergo both random and directed active migration. The random migration of a cell is modeled by a Brownian motion, whereas the directed active migration is caused by a certain signal. These signals originate from the cell's environment and have a chemical nature, which causes chemotaxis, or a mechanical nature, which causes mechanotaxis. Among these migration signals, there are many different type of -taxis, like haptotaxis, phototaxis and thermotaxis.
Note that from Figure 2.2, it is clear that the cell must adapt its cytoskeleton to move. First it stretches itself in the direction of motion, after which it propels the nucleus in the same direction. Then the cell has to contract and reassemble its focal adhesions to make the next 'step'.
The range of speed in which eukaryotes can move is very broad. For example, there are fish keratocytes [1] which move at a speed of 10-45 μm per minute. While on the other hand, there are mouse fibroblastoid cells that have a speed of 29 μm per *hour* [2].

[1] wound healing fibroblast of the cornea
[2] Hyper link to web page which presents these results: webpage

2.1.3. CELL CYCLE

The molecular process for cell movement is also relevant during cell mitosis, which is the process where a cell divides. During this division, one cell has to create a boundary membrane for two cells and thus has to rearrange its cytoskeleton.
Cell division is part of the cell cycle, which regulates the whole process of cell division. In Figure 2.3 the different stages in the cell cycle are given in an abstract way, the protein classes *cyclin* and *cyclin-dependent* kinases (CDK)[7] regulate how long each cell stays in a phase.

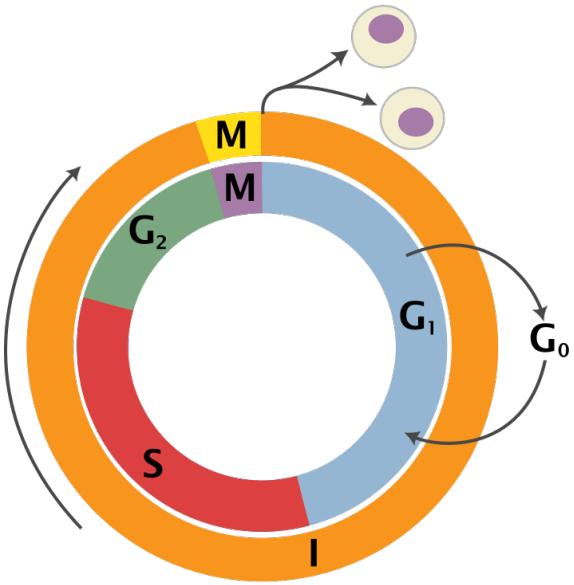

Figure 2.3: The cell cycle, copyright Richard Wheeler (Zephyris) 2006.

The cell cycle can be seen as having two consecutive phases - the **I**nterphase and **M**itosis. Where the interphase contains three sub phases - Gap 1 (G_1), **S**ynthesis and Gap 2 (G_2). During the interphase the cell grows, replicates its DNA and prepares the cell for the mitosis stage. As soon as a cell reaches this point, it enters the mitosis stage, stops growing and starts the division process.
Cell division is commonly referred to as cell proliferation. This proliferation process takes, for an average eukaryote, approximately 24 hours, where 11 hours are spent in the G_1 phase, 8 hours in the S phase, 4 hours in the G_2 phase and only one hours in the mitosis phase. Cell apoptosis, which is programmed cell death, takes roughly 24 hours [8].
The last phase, Gap 0 (G_0), also known as the resting phase, can be entered from Gap 1. When a cell enters the resting phase, it no longer proliferates. It is common for cells that are fully differentiated to enter this state. However, there is a possibility for some cells to re-enter the cell cycle despite not having differentiated entirely.
Stem cells have the ability of (life-long) self renewal and cell differentiation. This makes stem cells an ideal candidate to maintain the balance of different cells inside a cell population.
In their process of division, they can either divide in a symmetric or asymmetric way. In the first case, one stem cell yields two stem cells, whereas in the latter case we get one stem cell and one (slightly more differentiated) daughter cell.
The daughter cell is no longer considered a stem cell, since it is differentiated slightly towards a certain phenotype. However, the daughter cell can still be pluripotent [3]. As the daughter cell continues to proliferate, eventually a fully differentiated cell arises.

[3] Having the ability to differentiate towards multiple phenotypes

2.1.4. CELL DIFFERENTIATION

The process of cell differentiation is complicated, and the simulation of this process lies at the core of this thesis. A cell 'decides' when it should differentiate according to the signals it gets from the extra-cellular matrix which have a chemical, or mechanical nature.
Each cell secretes its share of proteins to the extra-cellular matrix, which in turn comes into contact with other cells. This interaction between cells gives a cell population the ability to communicate, and also for a stem cell to decide towards which phenotype it should differentiate. In a similar way, mechanical signals are conveyed through the ECM. Even though everything can be considered as a chemical at this level, we do make a distinction in the cause of a chemical signal.
Further, according to Even-Ram (2006) [9], (stem) cell differentiation is also influenced by the surface topology. In their article they state that under various elasticity conditions only certain phenotypes can arise. At soft tissue (1 kPa) we expect more growth of nerve cells, whereas at 10 kPa we see the formation of muscle tissue and at around 100 kPa the shaping of bone tissue.
Note however that it is possible for a stem cell that grows towards a certain phenotype, to change its destination and become a different phenotype. The process of change in phenotype is called metaplasia and dysplasia.

2.1.5. STEM CELLS

As mentioned earlier, stem cells have both the ability to renew themselves and eventually differentiate towards a certain target cell. During the development of a human (or animal), there exist several types of stem cells. For example, in the beginning of life there are fetal or embryonic stem cells, which are not limited to a fixed number of mitotic divisions, by definition [10].
Even in an adult human there still reside stem cells, to keep a fresh cell population, these cells are called 'adult stem cells'. In the next section we will discuss a special type of adult stem cell, called the mesenchymal stem cell.

MESENCHYMAL STEM CELLS

Mesenchymal stem cells[4] are considered to be the most promising for tissue engineering. The reason for this is their multi potency and their self renewal potential. A source of MSC can be found in bone marrow, trabecular bone, adipose tissue, skeleton muscle and others [3].
Their ability to differentiate towards several phenotypes is presented in Figure 2.4, where we also see the cytokines (or growth factors) that are involved in the differentiation process.

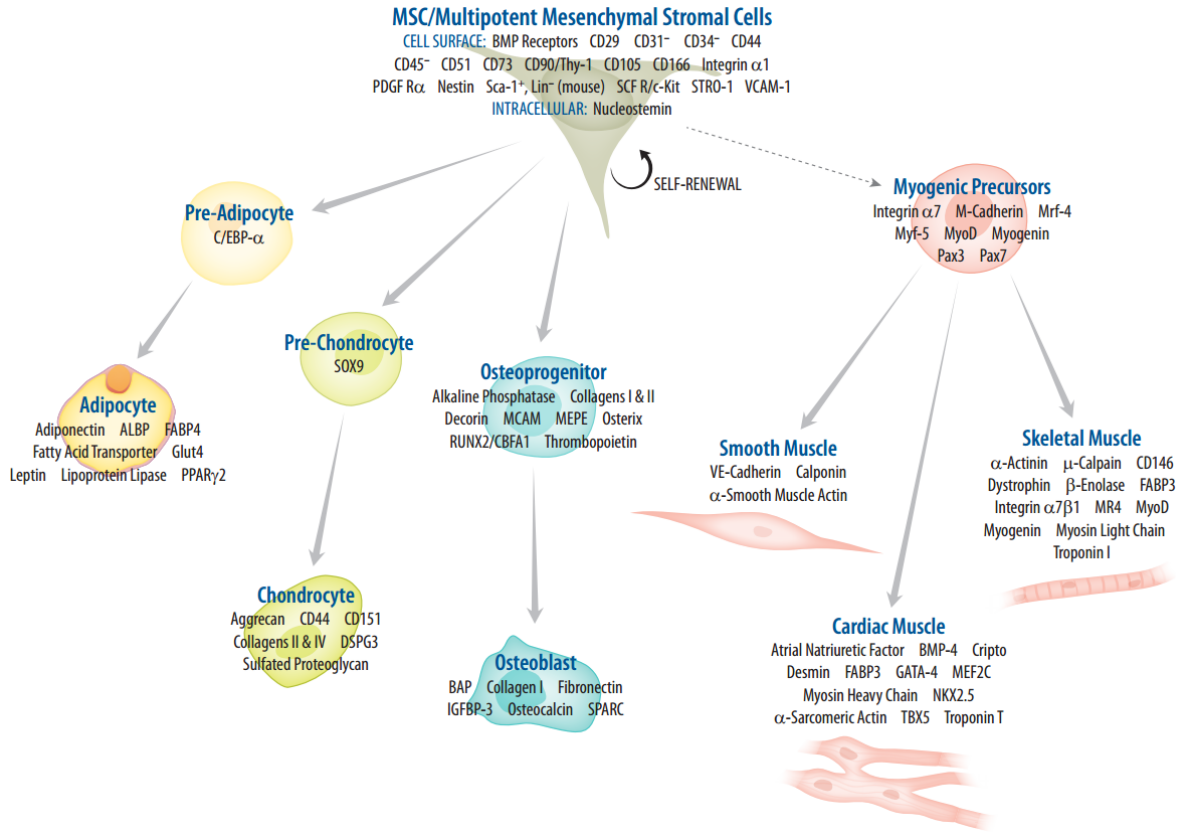

Figure 2.4: Differentiation path of mesenchymal stem cells, copyright R& D systems

The speed at which a MSC can move is roughly 30 $\mu m/h$ [11]. The study that revealed this result tried to determine the effect of electro-taxis on the motility of MSC, where they compared to movement speed of cells under influences of an electric field with that of a control group.
Another interesting result comes from a study by Bertolo [12], which links the motility of a MSC to the differentiation property. In his conclusion he states that the in-vitro cell motility might be a useful tool to characterize and distinguish the MSC population's differentiation potential. With this characterization, it then could be possible to assemble specific cell population compositions for tissue engineering.

[4] otherwise known as mesenchymal stromal cells

2.2. PHENOTYPES

2.2.1. MYOGENESIS - THE MYOCYTE

Myogenesis is the formation of muscle tissue and occurs during embryonic development and muscle recovery. We have listed the intermediate stages of embryo-tic myogenesis in Table 2.1. While we are not particularly interested in the muscle development of an embryo, it does give a framework to analyze myogenesis.

Table 2.1: The different stages in myogenesis [13]

Stage of myogenesisnesis	**Associated genetic factors**
De-lamination	PAX3, c-Met
Migration	c-Met/HGF, LBX1
Proliferation	PAX3, c-Met, Mox2, MSX1, Six, Myf5, MyoD
Determination	Myf5, MyoD
Differentiation	Myogenin, MCF2, Six, MyoD, Myf6
Specific Muscle Formation	Lbx1, Mox2
Satellite Cells	PAX7

The last stage in myogenesis is the satellite cell, according to Table 2.1. Satellite cells maintain the muscle tissue throughout adulthood and can be seen as quiescent myoblasts. Once they are activated, which can be caused by either injury or high mechanical loading, the satellite cells re-enter the cell cycle in order to proliferate and deliver differentiated cells via asymmetric division.
According to some studies, satellite cells are able to differentiate towards muscle, bone, and fat [14]. However, other studies show that this should not be possible for pure satellite cells [15].
Figure 2.5 shows an abstract representation of the differentiation path from a satellite cell to a muscle cell.

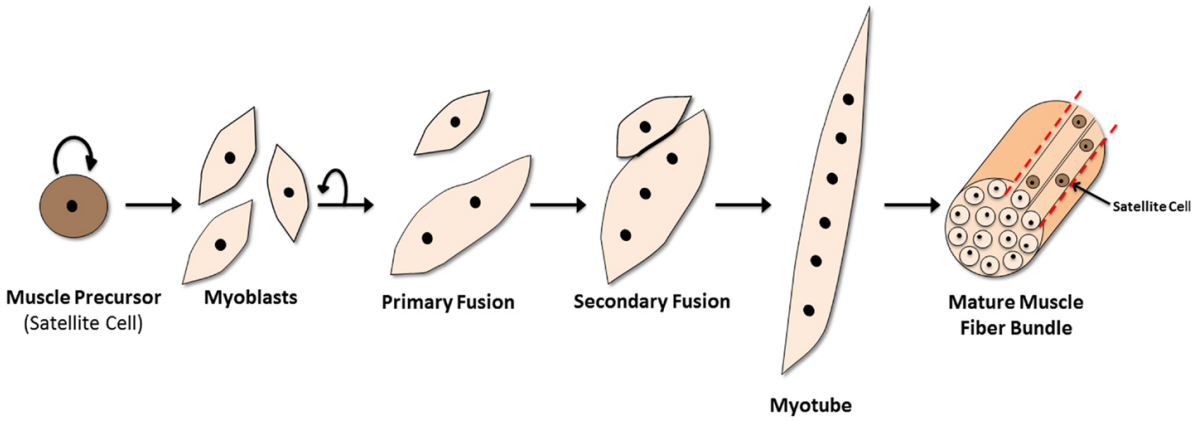

Figure 2.5: Graphically representation of myogenesis [16]

The differentiation process of a satellite cells resembles the stages shown in Table 2.1. Since, when a satellite cell is activated, it will first de-laminate itself and migrate to the site of injury where it will proliferate and differentiate.
In this differentiation process we can distinguish several physical stages that the satellite cell attains. The first stage is called the myoblast, which is a bi-polar spindle shaped cell that can fuse together with other myoblasts. Besides their fusion property, they are also able to proliferate and are determined to a myogenic phenotype.
The fusion process is totally controlled by several growth factors that are expressed either in the ECM or the cell itself. When enough myoblasts have fused together, we will call this quantity a myotube, which are multi-nucleated elongated cells. These myotubes are destined to become muscle fibers, but only after a period of maturation. During this maturation stage, the myotubes obtain their contractile behavior via the construction of myofibrils inside the cytoplasm. There the thick and thin filaments that make up the cytoskeleton align themselves to form the myofibrils. In Figure 2.6 you can see a graphical representation of the myofibers.

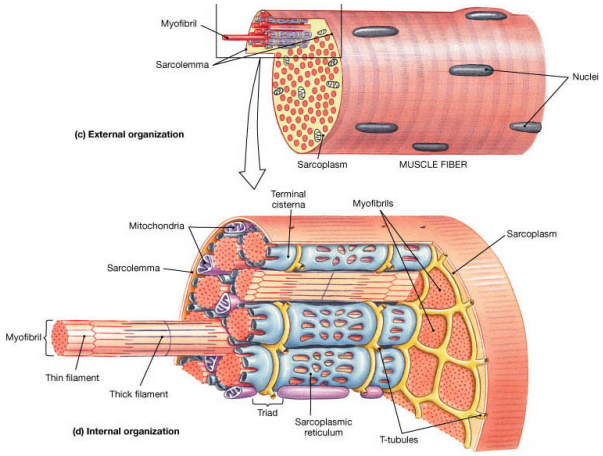

Figure 2.6: Build up of muscle cell source

These myofibers are also multi-nucleated cells, since they are formed by the fusion of many mono-nucleated myoblasts.
One important property of these myofibers is that they can contract in a very efficient way. When some myofibers are bundled together, we call them a muscle fascicle. These bundles are then bundled together to eventually obtain a full muscle, which can be activated voluntary in order to move a certain limb. In Figure 2.7 the reader can find a graphical representation on how this systems is build.

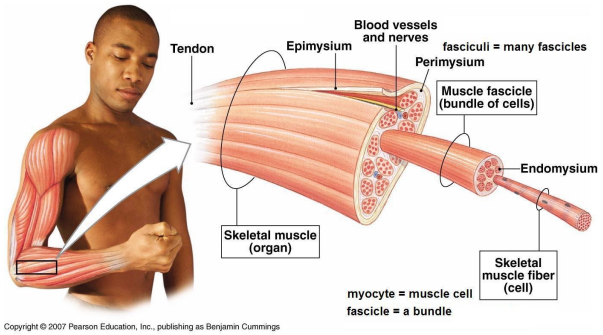

Figure 2.7: Build up of muscle cell

This process of contraction happens inside one muscle fiber, and because there are many myofibers bundled together, this can create a great amount of force. The mechanisms behind it come from the structure inside a myofiber, which is partitioned by several sarcomeres. These sarcomeres are the contractile compartments of a myofibers, inside these sarcomeres thin and thick filaments move to and away from each other to induce movement.

The movement of these thin and thick filaments are driven by the molecules ATP and Ca^{2+}, this behavior is called the cross-bridge theory and there are many animations available on the internet that show how this works.

Note that there are several types of muscles, which are distinguished by the speed at which they contract. For now, there has been made a distinction between three different types: slow twitch, fast twitch and the hybrid type. Where the slow twitch muscles are related to aerobic movement, the fast twitch to anaerobic movement, and where the hybrid type lays in between these two types.
Furthermore, besides the distinction in speed, all muscles have the ability to contract in different ways. The following list shows these three contraction types.

- Concentric contraction, muscle actively shortening:

  this happens when the load being lifted is less than the maximum tetanic tension it can generate.

- Eccentric contraction, muscle actively lengthening:

  when the load is larger than the muscle can handle, this occurs. It is an interesting phenomena since the cross-bridge theory is not as successful when describing eccentric loads.

- Isometric contraction, muscle actively held at a fixed Length:

  Think of this type when you lift an object. Your muscles contract and are actively held at a fixed length.

As mentioned in Section 2.1.5, cells communicate with each other via certain proteins, called cytokines or growth factors. When it comes to myocytes, we call the cytokines that are secreted by this cell group myokines. In this set of myokines there is a special subset that are only secreted during or after contraction, which exert either autocrine, paracrine or endocrine effects.
The secretion of these special myokines have a tremendous amount of influence on the cell population as a whole. Especially the adipose tissue that surrounds the muscle tissue will react to the secretion of these myokines by releasing their energy, and thus reducing the amount of fat tissue.

2.2.2. ADIPOGENESIS - THE ADIPOCYTE

Adipogenesis is the formation of fat cells from pre-adipocytes. Just like the process of myogenesis, a cell that undergoes adipogenesis moves through several distinct stages. These stages can be found in table 2.2.

Table 2.2: The different stages in adipogenesis [17]

Stage of adipogenesis	**Characteristics**
Mesenchymal precursor	Proliferation Ability to differentiate into multiple lineages
Committed preadipocyte	Proliferation Commitment to differentiation along adipocyte lineage Fibroblast-like morphology
Growth-arrested preadipocyte	Lack of proliferation due to contact inhibition
Mitotic clonal expansion	Re-entry into the cell cycle induced by hormonal stimulation Several rounds of cell divisions (i.e. mitotic clonal expansion) Induction of C/EBPb and C/EBPd expression and activity
Terminal differentiation	Cell-cycle arrest Induction of PPARg and C/EBPa expression Transcriptional activation of adipocyte genes (lipid and carbohydrate metabolism genes, adipokines)
Mature adipocyte	High expression of adipocyte genes Transcriptionally active PPARg, C/EBPa and C/EBPb Signet-ring morphology: large lipid droplet occupies majority of cell volume aThese distinctions are based primarily on in vitro studies.

The body can gain energy from three main macro-nutrients: fat, carbohydrate and protein. The adipose tissue inside a body is responsible for one of these macro-nutrients; fat.
The storage of fat can be done in two ways, either by the storage of white adipose tissue or brown adipose tissue. The white adipose cell contain large amount of triglycerides, which are esters made up of a glycerol and one or more fatty acids. In a white adipose cell the nucleus is not cell centered and very small, besides there is little to no cytoplasm since most of the cell's content is filled with triglycerides. The white adipose tissue secretes these fatty acids to act as energy for muscles or other tissue.
The brown adipose cell contains fat droplets of different size, a cell centered nuclei and a cytoplasm filled with numerous mitochondria. Unlike the white adipose cell, the brown adipose cell uses its own fatty acids to generate heat. However, most fat is stored as white adipose tissue.
Besides the storage of energy, fat also comforts, cushions the body and helps as a structural function as it attaches the skin to the underlying tissue [18]. An excess amount of fat inside an animal can cause negative effects, like obesity, cardiovascular disease or diabetes. This excess amount of fat is characterized by an increase in size (hypertrophy) and number (hyperplasia) of adipocytes.
Fat tissue, like muscle tissue, secretes adipokines which regulate physiological processes throughout the body like for example glucose metabolism, appetite and angiogenesis [17]. For a full list of all the known adipokines, we refer to the paper published by [19], where the reader can also find a short explanation to some interesting adipokines.

3

CLASSICAL MODELS FOR CELL POPULATIONS AND DIFFERENTIATION

In this chapter we will discuss two published models that are concerned with cell differentiation. We will try to find the essence of their models and the reason behind certain choices.

3.1. A MATHEMATICAL MODEL FOR CELL DIFFERENTIATION - PAVEL A. PROKHARAU

In this section we consider the model proposed by Prokharau in 2012, since our model is inspired by it.
What makes this model so unique, is the way it treats cell differentiation. Most models use a mass-balance-like system to simulate the differentiation to various phenotypes, by using a reaction-like term in the differential equation. In such models a cell type can directly 'jump' to another phenotype. However, in the model by Prokhaura, the differentiation is simulated as a gradual process.
This is done by a certain maturation state, which can change over time according to the different stimuli it senses. This differentiation process is reversible as long as the differentiation is not complete, that is when the cell is not matured yet.
The model by Prokharau et. al. [4], can be used to model any number of cell type differentiation and in their paper they also give an application of their model for the simulation of bone growth.

The simulation of this model gives the density of a certain cell type per unit of maturation and unit of volume over time and space. As stated before, the unique property of this model is the gradual change in cell differentiation.
By defining a set of complex boundary conditions, this model is able to change the composition of the cell population, and therefore able to simulate bone growth.
The governing equation used to simulate the differentiation behavior from MSCs towards bone or fibroblast tissue, is given by equation 3.1. Here we have an index $i \in \{b, f\}$ which denotes the bone phenotype or the fibroblast phenotype.

$$\frac{\partial c_i}{\partial t} = \nabla \cdot (D_c \nabla c_i) - \frac{\partial}{\partial a}(u_i c_i) + A_c(1 - c_{tot} - f - b)c_i, \; i = b, f. \tag{3.1}$$

Let $c_{tot}(\underline{x}, t)$ be the normalized total density of MSC's and the constant A_c the proliferation rate, then we see that the proliferation rate stagnates when the total density of MSC's reaches its limit, which is equal to one. Here we have that the normalized total density is given by

$$c_{tot}(\underline{x}, t) = \int_0^1 c_b + c_f \, da. \tag{3.2}$$

Further, the first term on the right-hand side of equation 3.1 represent a random walk of MSCs in the physical space. Here ∇ denotes the nabla operator in physical space and the constant D_c is the mobility coefficient. Further, the constant A_c is the rate of proliferation, which stops if the total density of MSC reaches its limit.

The differentiation process is modeled by the second term, $-\frac{\partial}{\partial a}(u_i c_i)$, where the flux $u_i c_i$ comes from the differentiation state domain.
This model is solved by using the finite volume method and the modified Euler method, for time integration. Using the finite volume method is a logical step, since they are dealing with conservation laws for the concentrations and cell densities.

3.2. AN AGENT-BASED DISCRETE MODEL FOR CELL POPULATIONS

In this section we give a short review of an agent-based, or discrete cell based model, proposed by P. Macklin and M.E. Edgerton [20]. An agent-based model allows a broad range of detail to be simulated where the cells are not bound to a certain lattice but are able to move through a continuous domain. A drawback of this approach depends on the amount of detail that is incorporated into the model, since this could drastically increase the computation time.
Even though this model does not model cell differentiation, it does give a modular approach to cell behavior. By using a relative simple approach, the model is able to simulate complex cell behavior, like tumor growth. The first characteristic of the model is the implementation of the cell states and cell cycle, an abstract representation of the connections between the cell states is given in Figure 3.1.

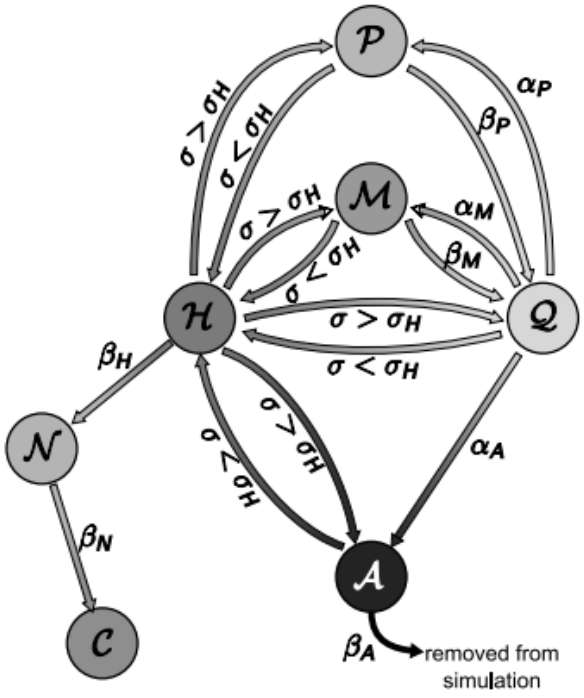

Figure 3.1: An abstract representation and connection of the cell states [20].

The symbols that are presented in the graph of Figure 3.1 denote probabilities of moving from one state to another.
The second characteristic of the model is that the cell agents are also under the influence of forces from other cells and their environment, which induce movement. This movement is captured by Newton's First law as shown in equation 3.3

$$m_i \dot{\mathbf{v}}_i = \sum_j \left(\mathbf{F}^{ij}_{cca} + \mathbf{F}^{ij}_{ccr} + \mathbf{F}^{ij}_{dda} \right) + \mathbf{F}^{i}_{cma} + \mathbf{F}^{i}_{cba} + \mathbf{F}^{i}_{cbr} + \mathbf{F}^{i}_{loc} + \mathbf{F}^{i}_{drag} \approx 0. \tag{3.3}$$

Here, the sum is over all cells j in the computational domain and i denotes a cell different from j. This model makes the assumption that the forces equilibrate quickly, so that $|m_i \dot{\mathbf{v}}_i| \approx 0$. To see how the forces from equation 3.3 apply to the cells, see Figure 3.2.
The cell force $\mathbf{F}_{cca}$ stands for the *cell-cell adhesion* force, which is driven by a complex equation accompanied with a potential function with a compact support to limit the reach of the cell-cell adhesion. The force $\mathbf{F}_{cma}$ stands for *cell-ECM adhesion*, $\mathbf{F}_{cba}$ represents the force that involves *cell-BM adhesion*, where BM stands for

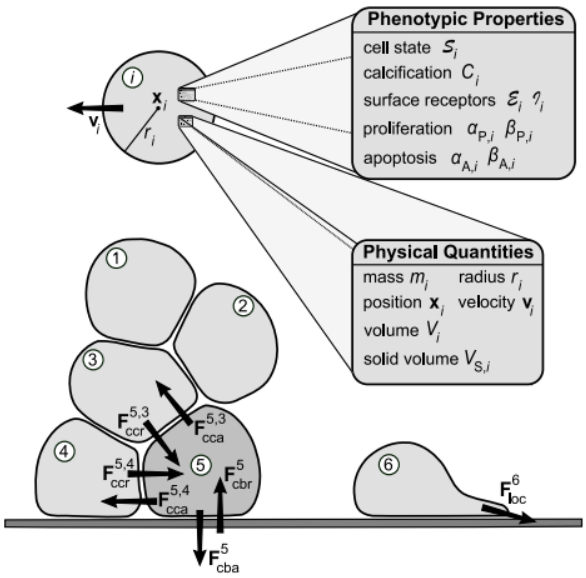

Figure 3.2: An abstract representation of the cell properties and inter-cellular forces.

Boundary Membrane. Then, $\mathbf{F}_{dda}$ gives the amount of force with *debris-debris adhesion*, where debris is a certain cell state that a cell can be in. The force $\mathbf{F}_{ccr}$ denotes the *cell-cell repulsion*, in order to prevent cell overlap during the simulation. There is also the $\mathbf{F}_{cbr}$ force for the *cell-BM repulsion* and $\mathbf{F}_{loc}$ stands for the locomotive force, which only applies to cells that are in the motile state.
Then, the third characteristic of the model is the ability to incorporate a molecular-scale signaling model to improve the cell agent's "decision process". Finally, the model also introduces a set of (continuous) equations that model the diffusion of oxygen among the cell population; the production of new ECM; and MMP (Matrix metalloproteinases). Subsequently, these concentrations then influence the behavior of the cells.
Due to the modular set up of the model, it is relatively easy to adjust certain parts of the model and replace it with an improved version where needed. This model is eventually used to simulate tumor growth in a two dimensional breast duct, which showed promising results. Although, for a more detailed explanation of the model we refer to the original paper [20].

4

A NOVEL MODEL APPROACH FOR CELL DIFFERENTIATION

In the previous chapter we have seen a short review of two modeling approaches for cell behavior. Together with the obtained biological knowledge, we are now ready to propose a novel model approach, which is inspired by the models Prokharau [4] and Vermolen [21].
The goal of this model is to give a mathematical framework for the differentiation behavior of mesenchymal stem cells towards several phenotypes. In this chapter we introduce the *two dimensional* version which simulates the differentiation towards *two* phenotypes, the fat and muscle cell. To introduce this model, we first explain how we simulate individual cells and state the general properties a cell has. Then we continue with the equation for the differentiation rate of a cell, and show which mechanisms are used to simulate this differentiation process. Subsequently, we present the equations of cell-motion, cell-rotation and cell growth. After that, we present results of this two dimensional modeling approach in Chapter 5 .
In Chapter 6, we present some preliminary results from the three dimensional version of the model. The mathematical details to define the three dimensional version are given in Appendix A.8. Furthermore, in Appendix A.7, one can find a short note on how to extend the model towards a variable amount of phenotypes.
The novel model approach simulates the differentiation behavior of an arbitrary number of discrete cells $C \in \mathbb{N}$ on a domain denoted by Ω, with boundary $\partial\Omega$. The mechanisms behind the model of the differentiation process are driven by a set of partial differential equations, which involve the diffusion of chemicals and the displacement of the domain Ω due to cellular interaction. These partial differential equations will be solved by using the Finite Element Method (FEM), see the Appendix A.2 for a brief explanation of the method.

4.1. THE CELL

The discrete cells are modeled as discrete ellipse-shaped entities. Their dimensions are defined by their length, width, center position and orientation. Furthermore, the boundary of a cell is approximated by a set of $L \in \mathbb{L}$ nodes from which cells will secrete their chemicals and mechanically interact with the ECM. These cells boundary nodes can be seen as the biological equivalent of focal adhesions.
In the coming sections, we will define various parameters and variables that can be cell or cell-boundary-node dependent. Variables that are only cell-dependent will have an index i as superscript, and variables that are cell-boundary-node dependent will have, in addition, an index j as subscript. Here the index i ranges from $1,\ldots,C$ and index j from $1,\ldots,L$.
Further, some variables are also phenotype dependent, for most of these variables we use the index k as subscript, where k attains the values 1 or 2. We use this subscript when we want to denote the phenotype dependency explicitly, since this could also be derived from the cell index itself.

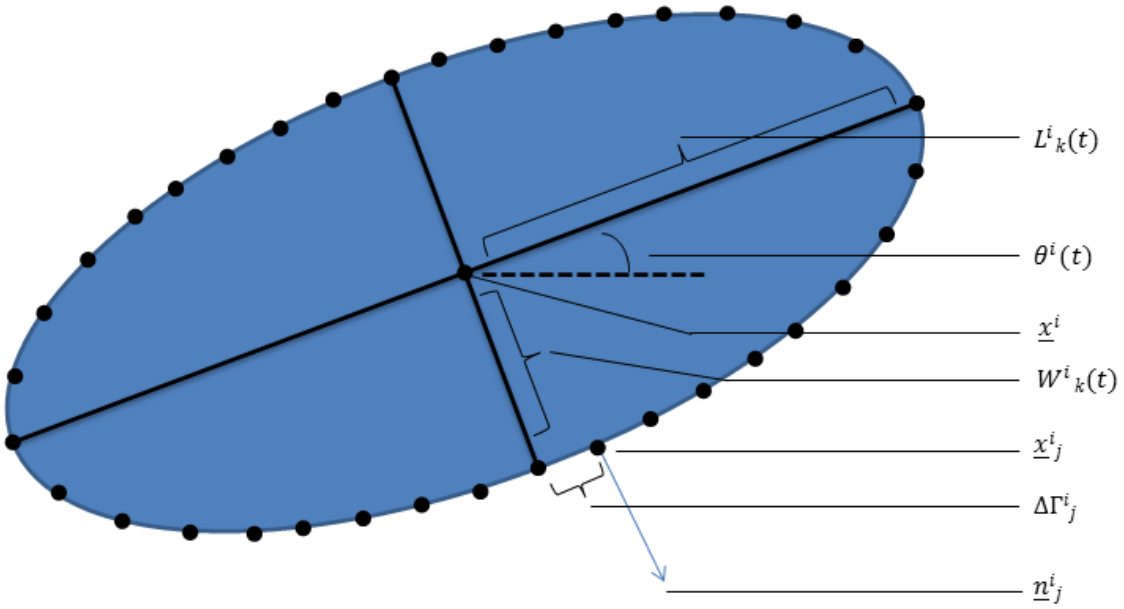

Figure 4.1: The geometrical entities associated with a cell

In Figure 4.1 we present a general simulation cell. Here $L^i_k(t)$ denotes the length, $W^i_k(t)$ is the width and $\theta^i(t)$ represents the angle between the orientation of the length $L^i_k(t)$ and the x-axis, of cell i. Further, the area of cell i is given by $A^i(t) = \pi L^i_k(t) W^i_k(t)$.
The vector $\underline{x}^i(t) = [x^i(t),\ y^i(t)]$ denotes the position of the cell center of cell i, the vector $\underline{x}^i_j(t) = [x^i_j(t),\ y^i_j(t)]$ denotes the position of the cell boundary node j of cell i, and $\underline{n}^i_j(t)$ is the outward normal vector at boundary node j of cell i.
When the orientation of the length of the cell is parallel to the x-axis, hence when $\theta^i(t) = 0$, the cell boundary are defined as

$$\begin{aligned} x^i_j(t) &= L^i_k(t)\cos(j\frac{2\pi}{L}), \\ y^i_j(t) &= W^i_k(t)\sin(j\frac{2\pi}{L}),\ j = 1,\ldots,L. \end{aligned} \tag{4.1}$$

By using this relation, we conclude that the outward normal vector $\underline{n}^i_j$ is given by

$$\underline{n}^i_j(t) = \left[\frac{x^i_j(t)}{(L^i_k(t))^2},\ \frac{y^i_j(t)}{(W^i_k(t))^2}\right]. \tag{4.2}$$

However, to include the orientation $\theta^i(t)$ of the cell, we use the anti-clockwise rotation matrix $R(\theta)$ to rotate the cell in the right direction. This rotation matrix is defined as

$$R(\theta) = \begin{bmatrix} \cos(\theta) & -\sin(\theta) \\ \sin(\theta) & \cos(\theta) \end{bmatrix}. \tag{4.3}$$

Hence, we apply this rotation to the vectors $\underline{x}^i_j(t)$ and $\underline{n}^i_j(t)$ to obtain the rotated version of the cell boundary nodes and normal vectors. Subsequently, we add the cell center $\underline{x}^i(t)$ to these rotated vectors to obtain the right position and normal vectors of the cells.
Furthermore, we assume that the cells can only interact with the domain Ω by their cell boundary nodes $\underline{x}^i_j(t)$. This means that a cell secretes its cytokine onto the domain, and applies its contractile forces on the domain via their cell boundary nodes. This results in a chemical concentration level on the domain and possibly a deformation of the domain as well. The cells then senses theses chemical concentrations and deformations via their cell boundary nodes.
The cell center node $\underline{x}^i(t)$ is needed to construct the cell boundary nodes and is used for the movement of the cells during the simulation, see Section 4.3. This node will not act as a sensing node like the cell boundary nodes. Further, note that in our simulations, the cells remain elliptic at all times. The issue of cell orientation will be dealt with in greater detail in Section 4.3.1.

4.2. THE MATURITY

To model the differentiation of the discrete cells, we propose the following model that is driven by a level of maturity $m^i(t)$ of cell i.

$$\begin{aligned} \frac{\mathrm{d}}{\mathrm{d}t} m^i(t) &= \frac{1}{2}\left(U_c^i(t) + U_M^i(t)\right), i = 1, \ldots, C, \\ \underline{m}(0) &\sim \mathrm{U}(0,1). \end{aligned} \tag{4.4}$$

Our assumption here is that the differentiation of cells depends solely on two terms, one that has a chemical nature and the other with a mechanical nature. Here $U_c^i(t)$ denotes the chemical part of the maturation rate of cell i, and $U_M^i(t)$ denotes the mechanical part for cell i. Both aging rates are determined by the amount of chemical and mechanical stimuli a cell i senses through its cell boundary nodes, these stimuli are denoted by $\psi_c^i(t)$ and $\psi_M^i(t)$, respectively. The values of these stimuli are obtained through a chemical model, which governs the reaction diffusion equation, and a mechanical model, which is driven by the Navier Cauchy momentum equation. We will elaborate on this in Section 4.2.1 and 4.2.2, respectively.
Further, the maturation of each cell is summarized in the $C \times 1$ vector $\underline{m}(t)$. In order to start the maturation process we set the initial value of the maturation vector $\underline{m}(0) = \mathrm{U}(0,1)$, hence each entry of the vector is set to a value from the uniform distribution over the open interval (0,1). This process, described by equation 4.4, stops for cell i when it reaches a maturity level of one. We then consider this cell to be mature and its phenotype will also be final.

To denote the phenotype corresponding to cell i, we use the variable $\iota^i(t)$, which represents the numerical version of the two phenotypes we are modeling. Hence, when $\iota^i(t) = 1$ we have that cell i is a myocyte, and when $\iota^i(t) = 2$ we have ourselves an adipocyte. Furthermore, let $\iota_M^i(t)$ denote the phenotype responsible for the mechanical stimulus $\psi_M^i(t)$ sensed by cell i. In a similar way, we also define $\iota_c^i(t)$ for the chemical stimulus.
The model for the change in phenotype is intertwined in the chemical and mechanical aging rate by the sign of these functions. For example, when a cell is a certain phenotype $\iota^i(t)$ and gains a chemical stimulus from a phenotype $\iota_c^i(t) \neq \iota^i(t)$, then the chemical aging rate $U_c^i(t)$ will have a negative sign, and thus reduces the maturity level of cell i. The same procedure applies to the mechanical aging rate. In order to obtain the correct sign, we use the following sign function

$$I^i(x,t) = \begin{cases} 1 & \text{if } x = \iota^i(t) \\ -1 & \text{if } x \neq \iota^i(t) \end{cases}. \tag{4.5}$$

When a cell eventually obtains a *negative* maturation due to this, it then changes its phenotype to the stimulus which is responsible for the largest rate of (negative) change. Subsequently, we take the absolute value of this (yet) negative maturation level before we continue with the calculations.

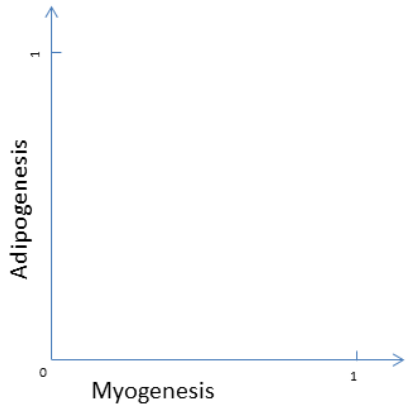

Figure 4.2: Differentiation paths of a cell

The maturation process, modeled by equation 4.4, and which genesis a cell will follow, is summarized in Figure 4.2. In this figure we can present the maturity level and phenotype of each cell in a single graph.

4.2.1. CHEMICAL SIGNALING

The explicit formulation of the chemical aging rate $U_c^i(t)$ is given in equation 4.6.

$$U_c^i(t) = U_{max} \tanh\left(2\frac{\psi_c^i(t)}{\xi(t)}\right) I^i(\iota_c^i, t), i = 1,\dots,C. \tag{4.6}$$

where we have used the hyperbolic tangent to easily limit the chemical aging rate by the constant U_{max}. The term inside the hyperbolic tangent is a scaled version of the chemical stimulus, where we use the function $\xi(t)$, which also depends on the chemical stimulus and is explained further in Section 4.5.
In turn, the chemical stimulus is dependent on the chemical concentrations sensed by cell i through its cell boundary nodes. These chemical concentrations are modeled by using the reaction diffusion equation. We will now introduce the way how we obtain the chemical stimulus per cell.

THE CHEMICAL MODEL

These chemical concentration represent a certain type of myokine or adipokine that are secreted by their corresponding cell type. The exact model that is used to calculate these concentrations is given by equation 4.7.

$$\begin{aligned} \frac{\partial c_k}{\partial t} + \nabla\cdot(\underline{v}_m c_k) - D_k\Delta c_k &= \sum_{i=1}^{C}\sum_{j=1}^{L}\gamma_k^i(t)\delta(\underline{x}-\underline{x}_j^i(t))\Delta\Gamma_j^i(t), \quad \underline{x}\in\Omega, \\ c_k(\underline{x},0) &= 0, \quad \underline{x}\in\Omega, \\ D_k\frac{\partial c_k}{\partial n} + \kappa c_k &= 0, \quad \underline{x}\in\partial\Omega. \end{aligned} \tag{4.7}$$

The chemical $c_k(\underline{x},t)$ is a density, the vector $\underline{v}_m$ is the mesh velocity due to the cellular forces that act on the domain and D_k is the diffusion coefficient.
Further, $k = 1,2$, denotes either the distribution of myokine or adipokine, respectively. Note that these processes are now independent, a possible extension is to have an interaction between the two chemical models. In the (Robin) boundary condition, the parameter κ gives the inflow (or outflow) of the chemical concentration. With this boundary condition we state that the flux on the boundary is proportional to the concentration at the boundary.
For this model, we have chosen a particular sourcing function to model the secretion of cytokine from the cell boundary nodes. The amount of cytokine that is secreted by the cells into the domain per unit of time is given by $\gamma_k^i(t)$, which depends on the maturity of the cell and the phenotype k as shown in equation 4.8.

$$\gamma_k^i(t) = \frac{\gamma_k^0 m^i(t)}{\sum_{j=1}^{L}\Delta\Gamma_j^i(t)}, \quad k = 1,2,\ i = 1,\dots,C, \tag{4.8}$$

where the variable γ_k^0 gives the amount of density that is secreted per time unit. We want to note here that the division by the summation over the intermediate length of a cell has not been implemented in the model. Until we were in a late stadium of this thesis project we noticed this error, unfortunately we could not resolve this in time.
The Dirac Delta function on the right hand-side of equation 4.2.1 is chosen such that the sourcing only occurs at the cell boundary nodes $\underline{x}_j^i$, $i = 1,\dots,C$, $j = 1,\dots,L$. Note that the sourcing term in equation 4.7 is summed over all the cells and their boundary nodes, which means that we get a sourcing term from each cell boundary node due to the Dirac Delta function.
As stated before, the chemical stimulus $\psi_c^i(t)$ depends on the chemical concentration a cell senses. This concentration is defined as the mean over all the concentration levels sensed by the cell boundary nodes, hence

$$\mathbf{c}_k^i(t) = \frac{1}{L}\sum_{j=1}^{L} c_k(\underline{x}_j^i, t), \quad k = 1,2,\ i = 1,\dots,C. \tag{4.9}$$

By using this definition, we define the chemical stimulus as the absolute difference of the chemical concentration of both phenotypes

$$\psi_c^i(t) = |\mathbf{c}_1^i(t) - \mathbf{c}_2^i(t)|, i = 1,\dots,C. \tag{4.10}$$

The chemical stimulus is then substituted in equation 4.6 to determine the aging rate caused by the chemical stimulus. The chemical stimulus direction $\iota_c^i(t)$ follows from the definition of the chemical stimulus, and is given by

$$\iota_c^i(t) = \arg\max_{k\in\{1,2\}} \mathbf{c}_k^i(t), i = 1,\ldots,C. \tag{4.11}$$

4.2.2. MECHANICAL SIGNALING

The explicit formulation of the mechanical aging rate $U_M^i(t)$ is given in equation 4.12.

$$U_M^i(t) = U_{max} \tanh\left(2\frac{\psi_M^i(t)}{\eta(t)}\right) I^i(\iota_c^i, t), i = 1,\dots,C. \tag{4.12}$$

Again, we have made use of the hyperbolic tangent to limit the mechanical aging rate. Further, the function $\eta(t)$ is used here to scale the mechanical stimulus $\psi_M^i(t)$ and is explained further in Section 4.5. The following section will show how we have obtained the mechanical stimulus.

THE MECHANICAL MODEL

The cells that live on the substrate Ω are able to apply force on it via their boundary nodes, as explained in section 4.1. These forces are summarized, per phenotype, into the vectors $\underline{F}_k, k = 1,2$ and are used in equation 4.13 to determine the displacement caused by these forces.

$$\begin{aligned} \nabla\cdot\underline{\underline{\sigma}} + \underline{F}_1 + \underline{F}_2 = 0, \quad \underline{x}\in\Omega, \\ \underline{\underline{\sigma}}\cdot\underline{n} + K\underline{u} = 0, \quad \underline{x}\in\partial\Omega. \end{aligned} \tag{4.13}$$

Here $\underline{\underline{\sigma}}(\underline{x},t)$ is the stress tensor, and $\underline{F}_k(\underline{x},t), k = 1,2$ are the forces the different phenotypes apply on the domain per unit area, their definition will be given in the next section.
The boundary condition used in 4.13, makes the boundary elastically connected to the tissue far away, where the parameter K represents the stiffness of the boundary.
Further, in order to calculate the displacement of the grid, we assume that equation 4.13 models small displacements. Hence, we will be working with the infinitesimal strain theory, which means that we assume

$$\|\underline{u}\| \ll 1, \text{ and }, \|\nabla\underline{u}\| \ll 1. \tag{4.14}$$

By these assumptions, we have the following relation between the strain tensor and the displacement gradient

$$\underline{\underline{\varepsilon}} = \frac{1}{2}(\nabla\underline{u} + (\nabla\underline{u})^T). \tag{4.15}$$

In addition, Hooke's law shows that the relation between the stress and the strain tensor is given by

$$E\begin{bmatrix}\varepsilon_{11}\\ \varepsilon_{22}\\ \varepsilon_{12}\end{bmatrix} = \begin{bmatrix}1 & -\nu & 0\\ -\nu & 1 & 0\\ 0 & 0 & 1+\nu\end{bmatrix}\begin{bmatrix}\sigma_{11}\\ \sigma_{22}\\ \sigma_{12}\end{bmatrix}. \tag{4.16}$$

Where E is Young's modulus of the extra cellular matrix and ν is the Poisson ratio. This relation can also be written as

$$\begin{bmatrix}\sigma_{11}\\ \sigma_{22}\\ \sigma_{12}\end{bmatrix} = \frac{E}{(1+\nu)(1-2\nu)}\begin{bmatrix}1-\nu & \nu & 0\\ \nu & 1-\nu & 0\\ 0 & 0 & 1-2\nu\end{bmatrix} E\begin{bmatrix}\varepsilon_{11}\\ \varepsilon_{22}\\ \varepsilon_{12}\end{bmatrix}. \tag{4.17}$$

From equation 4.17 and 4.15 we can see how the stress of the domain Ω is linked to the gradient of the displacement [1]. By substituting the equations 4.15 and 4.17 into equation 4.13, we can solve the problem for the displacement vector $\underline{u}(\underline{x},t)$.

[1] A full derivation, in 3D, of this relation is given in the appendix A.1

THE CELLULAR FORCES

The force vector $\underline{F}_k(\underline{x},t)$ that acts on the domain, is given by the sum of all the forces that every cell boundary node exerts on the domain. The force that a cell i applies on the domain via cell boundary node j, is directed in the (outward) normal direction $\underline{n}^i_j$ and has a magnitude of $F^i_{j,k}(t)$.
Since the dimension of the force vector $\underline{F}_k(\underline{x},t)$ must be force per surface area, we need to divide the magnitude $F^i_{j,k}(t)$ by the area of cell i in order to satisfy the dimensions of the Navier-Cauchy momentum equation. In mathematical terms we say that the force, produced by a phenotype k, applied on the domain Ω, is given by

$$\underline{F}_k(\underline{x},t) = \sum_{i=1}^{C} \frac{\sum_{j=1}^{L} F^i_{j,k}(t)\underline{n}^i_j}{A^i(t)}, k = 1,2. \tag{4.18}$$

Where the function $F^i_{j,k}(t)$ characterizes the force behavior of cell i with phenotype k on each cell boundary node j. For myocytes (i.e. $k=1$), we define the following characteristic force

$$F^i_{j,1}(t) = \begin{cases} k^i_j(t)\frac{\mathrm{d}}{\mathrm{d}t}L^i_1(t) & \text{if } m^i(t) < 0.8 \\ k^i_j(t)\frac{\mathrm{d}}{\mathrm{d}t}L^i_1(t) + \Delta\Gamma^i_j(t)F^0_1 m^i(t)\cos(\omega t) & \text{if } m^i(t) \geq 0.8 \end{cases} \tag{4.19}$$

For adipocytes ($k=2$), we define the following force function

$$F^i_{j,2}(t) = k^i_j(t)\frac{\mathrm{d}}{\mathrm{d}t}L^i_2(t). \tag{4.20}$$

where we have that the function $k^i_j(t)$ is given by

$$k^i_j(t) = \frac{E^i W^i(t)\Delta\Gamma^i_j(t)}{2L^i_k(t)}. \tag{4.21}$$

Here E^i is Young's modulus of cell i. The terms which contain the variable $k^i_j(t)$ are designed to mimic the force that cells exert on the domain while they grow. The idea originates from Hooke's law, which states that

$$F = k\Delta L, \tag{4.22}$$

with k the spring constant. Hence, this formula shows the amount of force needed to extend an object by a length ΔL with a resistance given by k. However, we would like to link the amount of resistance k to the Young's modulus of a cell, which can be done by looking at the unidirectional definition of the Young's modulus. This is given by

$$E = \frac{\sigma}{\varepsilon},\ \varepsilon = \frac{\Delta L}{L},\ \sigma = \frac{F}{A}. \tag{4.23}$$

where ΔL denotes the change in length, L is the original length and F is the force applied on an area A to obtain this change of length ΔL. We can rewrite this expression to the following format

$$E = \frac{F/A}{L/\Delta L} \Rightarrow \frac{F}{\Delta L} = \frac{EA}{L}. \tag{4.24}$$

By using equation 4.22, we can see that the following identity holds

$$k = \frac{EA}{L} \Rightarrow F = \frac{EA}{L}\Delta L. \tag{4.25}$$

To relate equation 4.25 to the force that belongs to the growth of a cell, we rewrite this equation to

$$F^i_{j,G}(t) = \frac{E^i W^i(t)\Delta\Gamma^i_j}{2L^i_k(t)}\frac{d}{dt}L^i_k(t). \tag{4.26}$$

where E^i is Young's modulus for cell i, $L^i_k(t)$ is the length of cell i and $F^i_{j,G}(t)$ is the growing force caused at cell boundary node j of cell i. Here we have introduced a virtual height, given by $\frac{1}{2}W^i(t)$, in order to approximate the area A of equation 4.25 together with $\Delta\Gamma^i_j(t)$. Further, the change in length $\frac{d}{dt}L^i_k(t)$ is approximated by

$$\frac{d}{dt}L^i_k(t) \approx \frac{L^i_k(t^{n+1}) - L^i_k(t^n)}{\Delta t}. \tag{4.27}$$

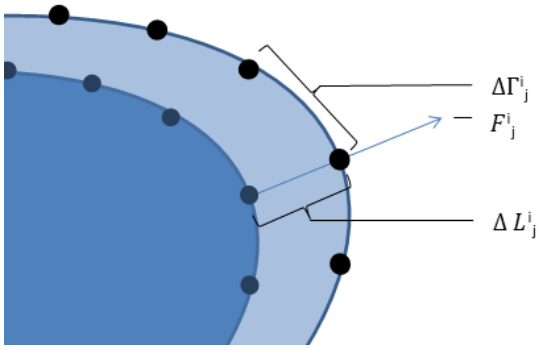

Figure 4.3: Pushing force of cells

Where Δt is the time step used in the numerical simulations. A graphical representation of the growing force that cells exert, is given in Figure 4.3.
Hence, we assume that both phenotypes produce a force due to their growth in size, and in addition, myocytes also have the ability to exert a pulsating force on the domain to simulate muscular behavior. This muscular behavior is characterized by two parameters F_1^0, the magnitude of the force a myocyte exerts, and by ω which is the angular frequency of the co-sinus. The angular frequency is related to the frequency f by $\omega = 2\pi f$, where the frequency is the reciprocal of the period T of the cosinus, hence $f = \frac{1}{T}$ period of the force.
Since we are solving our models in a discrete sense, we have a time step Δt which determines the accuracy of our solutions. However, this time step also determines the amount of detail that is modeled by the pulsating force. Due to the angular frequency ω, we need an upper bound for the time step in order to model periodic behavior. When we analyze the co-sinus, we have that

$$\cos(\omega t) = \cos(2\pi f t). \tag{4.28}$$

Due to the discrete time stepping, we state that $t = n\Delta t, n = 1, \ldots, T_{max}$. This simplifies equation 4.28 to

$$\cos(2\pi f t) = \cos(2\pi f n\Delta t) = \cos(n\pi(2f\Delta t)), n = 1, \ldots, T_{max}. \tag{4.29}$$

Knowing that taking the co-sinus of integer multiples of π results in a sequence of alternating -1 and 1, we see that we must have that

$$2f\Delta t \leq 1 \Rightarrow \Delta t \leq \frac{1}{2f}, \tag{4.30}$$

with f the frequency of the signal in order to simulate a predictable periodic function.
By using the force vectors that are produced by the cells, we obtain the displacement of the domain Ω by solving the system 4.13 with the FEM. We use this displacement field to determine the mechanical stimulus for each cell. For the definition of the mechanical stimulus, we use the octahedral shear strain to represent the activity on the domain. This quantity is defined by

$$\phi(\underline{x}) = \frac{2}{3}|\varepsilon_1(\underline{x}) - \varepsilon_2(\underline{x})|. \tag{4.31}$$

Note that $\phi(\underline{x})$ is a dimensionless scalar variable that is based on the principle strains, which are the eigenvalues of the strain tensor (see equation 4.15).
To obtain the octahedral shear strain for one cell, we take the average of the octahedral shear strain of all the cell boundary nodes.

$$\boldsymbol{\phi}^i(t) = \frac{1}{L}\sum_{j=1}^{L}\frac{2}{3}|\varepsilon_1(\underline{x}_j^i) - \varepsilon_2(\underline{x}_j^i)|. \tag{4.32}$$

The mechanical stimulus sensed by cell i is then given by the integral of a weighted version of the rate of change of the octahedral shear strain over a time interval $((t-\tau)+, t)$, where τ denotes the length of the time interval.

By this we wish to simulate muscular memory of the muscle tissue, where we assume that recent muscular activity will cause the most mechanical stimulus in the cell population. In mathematical terms, we write the mechanical stimulus as

$$\psi_M^i(t) = \psi_M(\boldsymbol{\phi}^i) = \int_{(t-\tau)+}^{t} w(s) \left(\frac{d\boldsymbol{\phi}^i}{ds} \right)^2 ds, \quad i = 1, \dots, C. \tag{4.33}$$

Where the weight function $w(s)$ is given by

$$w(s) = \begin{cases} e^{(s-t)}, & s \in (t-\tau, t) \\ 0 & \text{else} \end{cases} \tag{4.34}$$

The direction of the mechanical stimulus $\iota_M^i(t)$ is determined by the behavior of the octahedral shear strain $\boldsymbol{\phi}^i(t)$. Since the octahedral shear strain reflects the behavior that the cells have on the domain, and because myocytes can contract in a periodic fashion, we know that we can distinguish the different phenotypes via the characteristics of the octahedral shear strain.
Therefore, we expect that when muscle-tissue is dominating in the cell population, the octahedral shear strain will act in a periodic fashion similar to the muscle contraction. Thus, in order to distinguish muscular behavior from non-muscular behavior, we apply the Fourier Transform to the octahedral shear strain $\boldsymbol{\phi}^i(t)$ to determine the frequency of this signal.
The Fourier Transform is useful in the sense that it translates a signal over a time domain to a signal over the frequency domain. With this transformed function, in the frequency domain, we can then determine which frequency possesses the highest amplitude which then tells us what the frequency of the original signal is most likely to be.
Hence, for this approach we apply the Discrete Fourier Transform on the octahedral shear strain to decipher the numerical frequency, which we denote by $\hat{f}$. Then we compare this frequency with the frequency of the myocyte force function given by f. However, we expect that the numerical frequency of the octahedral shear strain $\hat{f}$ will be twice time the original frequency f since we took the absolute value of the principle strains in equation 4.31. Therefore we define the direction of the mechanical stimulus as

$$\iota_M^i(t) = \begin{cases} 1 & \frac{1}{2}\hat{f} \in [\frac{9}{10}f, \frac{11}{10}f] \\ 0 & \frac{1}{2}\hat{f} \notin [\frac{9}{10}f, \frac{11}{10}f] \end{cases}. \tag{4.35}$$

For an explanation on the DFT, see Appendix A.5.

4.3. CELL MOVEMENT

During the simulation, the cells in the domain have to ability to move, which is based upon various types of stimuli. In this model we take into account mechanotaxis, chemotaxis and the Brownian motion. The resulting stochastic differential equation (SDE) is given by

$$\underline{v}_k^i(t) = d\underline{x}_k^i(t) = \sigma_k^i(t)d\underline{W}(t) + 4\mu_k m^i(t)(1-m^i(t))\nabla \mathbf{c}_k^i(t)dt + \mu_{M,k}\nabla \mathbf{M}^i(t)dt, i = 1,\dots,C,\ k = 1,2, \tag{4.36}$$

This equation is solved by the Euler-Maruyama method, which results in the following formula

$$\underline{x}_k^i(t^{n+1}) = \underline{x}_k^i(t^n) + \sigma_k^i(t)\Delta\underline{W}(t) + 4\mu_k m^i(t^n)(1-m^i(t^n))\nabla \mathbf{c}_k^i(t)\Delta t + \mu_{M,k}\nabla \mathbf{M}^i(t)\Delta t. \tag{4.37}$$

Where $i = 1,\dots,C,\ k = 1,2, n = 1,\dots,T_{max}$. Here n stands for the nth time step and Δt is the time step.

BROWNIAN MOTION

We assume that cells are subject to random walk, the first term in equation 4.36, 4.37 is responsible for this. Here the standard deviation σ_k is given by $\sigma_k^i(t) = \sigma_k^0(1-m^i(t)),\ \sigma_k^0 = \sqrt{2D_k}, k = 1,2$. Thus, as a cell matures it becomes less subject to the random walk.
The vector $d\underline{W}(t)$ and $\Delta\underline{W}(t)$ represent the Wiener processes that model the random walk, which is characterized by three properties

- $\underline{W}(0) = 0$;
- The function $t \to W(t)$ is almost surely continuous everywhere;
- $W(t)$ has independent increments with $W(t) - W(s) \sim N(0, t-s)$, for $0 \le s < t$ where $N(\mu,\sigma^2)$ denotes the normal distribution with expected value μ and variance σ^2.

Instead of assuming $W(t) \sim N(0,t)$, which cannot support algebraic calculations, the Wiener process dW is introduced. Further, we have that $\Delta W \equiv \alpha\sqrt{\Delta t}$, where $\alpha \sim N(0,1)$ and Δt is the time step.

CHEMOTAXIS

The second term in equation 4.36, 4.37 mimics the behavior of chemotaxis. The term presented here is equal to the maximum gradient sensed on the cell boundary nodes, which is measured in the L^2-norm. For this reason, we have executed the following computations. First we calculate which node senses the largest chemical gradient.

$$p^i = \arg\max_{j\in\{1,\dots,L\}} \|\nabla c_k(\underline{x}_j^i, t)\|, i = 1,\dots,C. \tag{4.38}$$

The index p^i is then substituted in the actual gradient to obtain the following

$$\nabla \mathbf{c}_k^i(t) = \nabla c_k(\underline{x}_{p^i}^i), i = 1,\dots,C. \tag{4.39}$$

We assume that this variables mimics the behavior of chemotaxis in a cell population. However, we would like to see the modeling over several chemical substances and different reactions towards these chemical concentrations in terms of movement and behavior. For example, some chemicals repel a certain cell type, while other chemicals attract this phenotype.
In a complex setting we would like to see attraction towards more specific chemicals and possibly different attraction rates over time.

MECHANOTAXIS

The third term $\nabla \mathbf{M}^i(t)$ denotes the movement caused by mechanotaxis, which is driven by the gradient of the mechanical strain energy (MSE).
From [22] we see that the mechanical strain energy in two dimensions is defined as

$$M(\underline{x}, t) = \frac{1}{2}\left(\sigma_{11}\varepsilon_{11} + \sigma_{12}\varepsilon_{12} + \sigma_{22}\varepsilon_{22}\right). \tag{4.40}$$

We apply a similar approach for the calculation of the mechanical strain energy per cell, as with the chemical gradient. Hence, we calculate the gradient of the MSE on each cell boundary node per cell and then determine

the maximum gradient which will give the direction and magnitude of movement. In summary we calculate the index which holds the maximum gradient in magnitude by

$$p^i = \arg\max_{j\in\{1,\dots,L\}} \|\nabla M(\underline{x}^i_j, t)\|, i = 1,\dots,C. \tag{4.41}$$

Using this index, we define the following direction of movement

$$\nabla \mathbf{M}^i(t) = \nabla M(\underline{x}^i_{p^i}), i = 1,\dots,C. \tag{4.42}$$

The details behind the calculation of this gradient, using gradient recovery techniques, are found in Appendix A.6.

Further more, the mechanical sensitivity parameter $\mu_{M,k}$ has a different sign based on the phenotype k. Here we have chosen that when $k = 1$ the sign of this parameter is negative and when $k = 2$, we have a positive sign. By this choice, we try to simulate the clustering of fat tissue around muscle tissue, since there will be the most mechanical strain energy, and the spread of muscle tissue over the domain to avoid clustering of myocytes. However, we have not found a paper which presents a value for this parameter, thus the value we will use is chosen such that we obtain the behavior we desire.

4.3.1. CELL ROTATION

As stated in Section 4.1, the cells are assumed to have the ability to rotate. This rotation is based on the current orientation $\theta^i(t)$ and on the direction in which the cell will move $\underline{v}^i_k(t)$. We assume that the orientation of the cell will change towards the direction of movement. Therefore we have used the following equation to model this behavior.

$$\begin{aligned} \frac{d}{dt}\theta^i(t) &= \theta^{i,0}(t)\cos^{-1}\left(\frac{\underline{v}^i_k(t)\cdot\underline{\theta}^i(t)}{\|\underline{v}^i_k\|\|\underline{\theta}^i\|}\right), \quad i = 1,\dots,C, k = 1,2, \\ \theta^i(0) &= 2\pi U(0,1), \qquad\qquad i = 1,\dots,C. \end{aligned} \tag{4.43}$$

Here $\theta^{i,0}(t)$ is used to scale, and provide the correct sign to the rate of change. The vector $\underline{v}^i_k(t)$ is the velocity at which cell i moves, and $\underline{\theta}^i(t)$ is the angle $\theta^i(t)$ of cell i written in vector format. This situation is sketched in Figure 4.4.

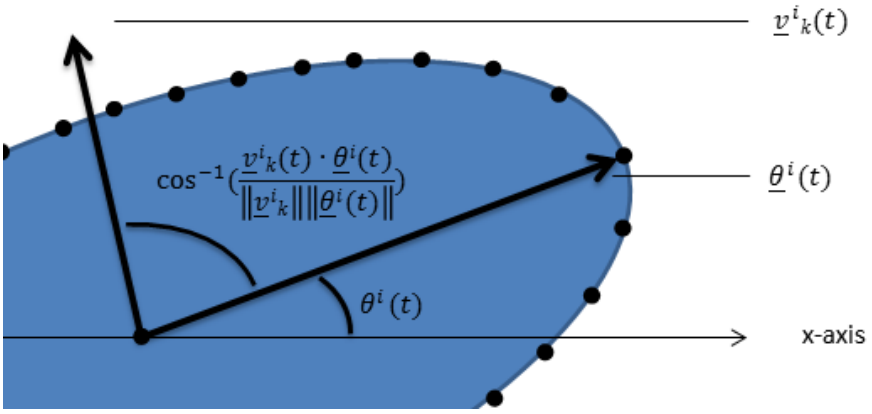

Figure 4.4: Graphical representation of the (anti-clockwise) angle

In the second term of equation 4.43, we determine the angle between the vectors $\underline{v}^i_k(t)$ and $\underline{\theta}^i(t)$, which will produce a non-negative angle. However, since we want to change the angle of cell i *towards* the direction of movement, we need to determine if the right hand side of equation 4.43 is positive or negative.

For the situation shown in Figure 4.4, we want a positive rate of change, since the angle $\theta^i(t)$ is taken with respect to the x-axis. Hence, in order to determine the sign of the rate of change, we need to determine in which quadrant $\underline{v}^i_k(t)$ lies with respect to $\underline{\theta}^i(t)$.

To do this, we first define the clock-wise rotation matrix $R_{cw}(\theta)$

$$R_{cw}(\theta) = \begin{bmatrix} \cos\theta & \sin\theta \\ -\sin\theta & \cos\theta \end{bmatrix}. \tag{4.44}$$

Then, to determine in which quadrant $\underline{v}_k^i(t)$ lies, we rotate this vector with an angle $\theta^i(t)$ in a clock-wise direction,

$$\underline{\hat{v}}_k^i(t) = R_{cw}(\theta^i(t))\underline{v}_k^i(t). \tag{4.45}$$

Now the problem is reduced to looking in which quadrant the rotated vector $\underline{\hat{v}}_k^i$ lies with respect to the x-axis. This problem is solved by looking at the sign of the dot product between the rotated vector $\underline{\hat{v}}_k^i$ and the unit vector $\underline{e}_y$ of the y-axis. Therefore we define the scaling factor as

$$\theta^{i,0}(t) = \text{sgn}\left(\underline{\hat{v}}_k^i(t) \cdot \underline{e}_y\right). \tag{4.46}$$

This result is then used for equation 4.43. To solve this equation, we use the Euler-backward method to discretize this equation in time and obtain the following updating formula

$$\begin{aligned} \theta^i(t^{n+1}) &= \theta^i(t^n) + \Delta t \theta^{i,0}(t^n) \cos^{-1}\left(\frac{\underline{v}_k^i(t^n) \cdot \underline{\theta}^i(t^n)}{\|\underline{v}_k^i(t^n)\| \|\underline{\theta}^i(t^n)\|}\right), \\ \underline{v}_k^i(t^n) &= \frac{\underline{x}_k^i(t^{n+1}) - \underline{x}_k^i(t^n)}{\Delta t} \end{aligned} \tag{4.47}$$

This rotation $\theta^i(t^{n+1})$ is then used in the rotation matrix given in equation 4.3 to rotate the cell boundary nodes in the correct direction.

4.4. PHYSIOLOGICAL CHANGE OF THE CELL

As the cells mature through time, they will gradually obtain the characteristics of a phenotype. This is noticeable in their force behavior as well as their movement.
In this model we also adapt the shape of the different phenotypes as they are maturing. We assume that muscle cells will have an elliptical shape and fat cell a circular shape, this behavior is summarized in the following equations

$$L_k^i(t) = L_k^0 + (L_{\infty,k} - L_k^{i,0}) m^i(t) \tag{4.48}$$

$$W_k^i(t) = W_k^0 + (W_{\infty,k} - W_k^{i,0}) m^i(t) \tag{4.49}$$

Where L_k^0, W_k^0 are the initial length and width of phenotype k and $L_{\infty,k}, W_{\infty,k}$ are the maximum length and width obtained by phenotype k. Here the maturity $m^i(t)$ scales the length of each phenotype in a linear way from the initial length towards the maximum length. The exact definition of the initial and maximum length and width are given in Table 4.1

4.5. PARAMETER CHOICE

In this section we give an elaborate explanation on how we choose the parameters, since this is a crucial part for the simulation results. The parameters are split up into four distinct groups, Table 4.1 shows the physiological parameters of the cells, Table 4.2 gives the parameters belonging to the simulation of the mechanical model, Table 4.3 presents the parameters that are needed for the chemical model and Table 4.4 gives the parameters belonging to the maturation process.
Most parameter values are found through research in cell biology papers, however, some values are self created and therefore an NA (Not Applicable) is added instead of a link to the source.
The dimension of all the parameters are expressed by using $[L], [T], [\rho]$, which expresses the length, time and density of a parameter, respectively. In this thesis our reference length is in micrometers, the time dimension represents minutes and rho is $\mu g/\mu m^2$. To shorten notation, we also use $[N] = \frac{[L]}{[T]^2}[\rho][L]^2$ to denote the force, note here the $[L]^2$ after the density, this is because we are using a two dimensional domain. Furthermore, during this dimension analysis we use the standard metric prefixes.

Table 4.1: Table containing physiological parameters of the two phenotypes

Variable name	Variable symbol	Dimension	Value	Reference
Initial width of a myocyte	W_1^0	$[L]$	25	source
Initial length of a myocyte	L_1^0	$[L]$	35	NA
Max. width of a myocyte	$W_{\infty,1}$	$[L]$	25	source
Max. length of a myocyte	$L_{\infty,1}$	$[L]$	150	NA
E-modulus of a myocyte	$E_{c,1}$	$[\mu N][L]^{-2}$	$10 \cdot 10^{-3}$	[23]
Initial width of an adipocyte	W_2^0	$[L]$	25	NA
Initial length of an adipocyte	L_2^0	$[L]$	25	NA
Max. width of an adipocyte	$W_{\infty,2}$	$[L]$	75	[24]
Max. length of an adipocyte	$L_{\infty,2}$	$[L]$	75	[24]
E-modulus of an adipocyte	$E_{c,2}$	$[\mu N][L]^{-2}$	$0.42 \cdot 10^{-3}$	[25]

In Table 4.1 we see the values that correspond to the geometric parameters of a cell, which are visualized in Figure 4.1. Note here the $[L]^{-2}$ for the elastic moduli of the cells, this should imply that we are using three dimensional cells when one recalls that the dimension of the elastic modulus is force per unit area. However, from section 4.1 we showed that we modeled cells as two dimensional entities, which is thus in contrast with the chosen dimension of the elastic modulus of a cell.
To justify this conflict, we assume that both cell types are virtually cylindrical shaped with a height equal to $\frac{1}{2}W^i(t)$, which can be seen in equation 4.26. By virtually we mean that it has no further implication in the model whatsoever, the sole reason is to justify the dimensions of the equations.

Table 4.2: Table containing mechanical related parameters for the model

Variable name	Variable symbol	Dimension	Value	Reference
E-modulus of the substrate	E	$[\mu N][L]^{-1}$	$25 \cdot 10^{-3}$	[26]
Poisson rate	ν	$[-]$	0.3	[27]
Force of myocyte	F_1^0	$[\mu N][L]^{-1}$	15	[28]
Period of contraction	ω	$[-]$	$\frac{2}{10}\pi$	NA
Muscle memory	τ	$[T]$	30	NA
B.C. mechanical model	K	$[\mu N][L]^{-2}$	$20 \cdot 10^{-3}$	NA
Mechanical sensitivity for myocyte	$\mu_{M,1}$	$[L]^3[\mu N]^{-1}[T]^{-1}$	$3 \cdot 10^4$	NA
Mechanical sensitivity for adipocyte	$\mu_{M,2}$	$[L]^3[\mu N]^{-1}[T]^{-1}$	$0.5 \cdot 10^3$	NA

The value for the period of contraction and the muscle memory here chosen in Table 4.2, are quite arbitrary, since any number would suffice. This is because we can not model actual muscle behavior with this model, since this is far too complex compared to this model, we can only make sure that we are able to identify the muscular behavior.
Further, the value for the mechanical sensitivity is obtain after a process of trial and error such that it simulates the behavior we desire.

Table 4.3: Table containing chemical and kinetic related parameters for the model

Variable name	Variable symbol	Dimension	Value	Reference
Diffusion coef. myokine	D_1	$[L]^2[T]^{-1}$	810	source
Secretion rate myocyte	γ_1	$[\rho][T]^{-1}$	0.5	[29]
Sensitivity towards myocyte gradient	μ_1	$[L]^2[T]^{-1}[\rho]^{-1}$	$6.6 \cdot 10^3$	NA
Diffusion coef. adipokine	D_2	$[L]^2[T]^{-1}$	810	source
Secretion rate adipocyte	γ_2	$[\rho][T]^{-1}$	0.5	[29]
Sensitivity towards adipocyte gradient	μ_2	$[L]^2[T]^{-1}[\rho]^{-1}$	$6.6 \cdot 10^3$	[30]
B.C. chemical model	κ	$[L][T]^{-1}$	1	NA

The value for the sensitivity towards the chemical gradient, shown in Table 4.3, is also chosen to satisfy the simulation results we desire. At first we tried values taken from the paper by Ford [30], which reflected the chemical sensitivity of the E.coli bacteria, but these values gave strange simulation results. Hence, after some trial and error we have found these values which result in a decent balance between the three factors of movement.
Note that the coefficients for both phenotypes shown in Table 4.3 are taken equal. The reason for this is mostly due to lack of information of the biological parameters, therefore we conduct a sensitivity analysis in Chapter 5 in order to see the effect in small changes of these parameters.

Table 4.4: Table containing chemical related parameters for the model

Variable name	Variable symbol	Dimension	Value	Reference
maximum aging rate	U_{max}	$[T]^{-1}$	1/120	NA
scaling MAR	$\eta(t)$	$[-]$	$\max_{i\in[1,C]} \|\psi_M^i(t)\|$	NA
scaling CAR	$\xi(t)$	$[-]$	$\max_{i\in[1,C]} \|\psi_c^i(t)\|$	NA

In Table 4.4 we see the parameters associated with the aging rate equations, see equation 4.6 and 4.12. These parameters are hard to choose since they have no biological relevance, they are mere mathematical artifacts used to model the behavior we think that is appropriate. For the moment we have chosen the following formulation for the scaling parameters

$$\begin{aligned} \eta(t) &= \max_{i\in[1,C]} \|\psi_M^i(t)\| \\ \xi(t) &= \max_{i\in[1,C]} \|\psi_c^i(t)\| \end{aligned} \tag{4.50}$$

The advantage of choosing these scaling parameters as such, is due to its simplicity in implementation and scalability with the cell population size. In the case of $\xi(t)$, we are aware of the fact that by this choice we let the maturity depend on a relative chemical concentration sensed by the cell population at a certain time t, which seems to be in contrast with the natural process of cell differentiation. Since from a biological point of view, all processes are controlled by an absolute *amount* of biomolecules which can be part of a chemical reaction. These chemical reactions obey the conservation of mass and energy, hence this kind of relativity may be wrong here.
Further, the maximum aging rate has been set to $\frac{1}{120}$ for the moment, as can be seen in Table 4.4. Which means that the minimum transition time from maturity level zero to one, is equal to 120 time units, which are in this case minutes. This setting can easily be adapted if we gather more information on the time it takes for a cell to undergo myo- or adipogenesis.

4.5.1. MODEL OVERVIEW

This section will give an overview on how we have implemented the model in Matlab, since the model and all its components can seen quite complex.

Algorithm 1 Algorithm for the novel model approach

Load Parameter.m ▷ *The first step is to load all the parameters and predefined matrices*
Execute Assembly process ▷ *Here we assemble the mass matrices of the mechanical and chemical model*
Execute Element-Cell process ▷ *Here we find which cell nodes lie in which triangle, this relation is crucial to construct the force and source vectors*
Execute External Vector process ▷ *Here we assemble the cell-force vector and cell-source vector*
for $n = 2$ to T_{max} **do**
    Solve mechanical model
    Update mesh
    Execute Aging rate process ▷ *Here we calculate all the chemical gradients and mechanical octahedral shear strain needed to determine the chemical and mechanical aging rate*
    Execute Gradient Recovery process ▷ *The gradient of the mechanical strain energy is now calculated by using the ZZ-patch gradient recovery method*
    Execute Update process ▷ *By using the obtained aging rates and chemical/mechanical gradient, we can update the maturity, position and all the other cell variables that are linked to this*
    Execute Assembly process
    Execute Element-Cell process
    Execute External Vector process
    Solve chemical model ▷ *Since we solve the chemical model implicitly, we need the mass matrices and source functions on the next time step. Therefore, we can only calculate the chemical concentration after the grid displacement and cell movement*
    Execute Plot process
end for

5

RESULTS FROM THE NOVEL MODEL APPROACH IN 2D

Having defined and motivated the novel model approach, together with a clear set of parameters, we are ready to present results obtained from the two dimensional version of the novel model approach. In this chapter we will present two type of results, one in the form of a sensitivity analysis where we present the model results from the variation of a set of parameters, the other is a position analysis based on the movement of the cells. The goal of these results is to test our hypotheses about the behavior of the model, since validating our model approach with actual biological data is not possible for now.

5.1. SENSITIVITY ANALYSIS

The sensitivity analysis will be used on the force magnitude of the myocytes, as well as on the secretion rate parameters of both phenotypes. The reason to analyze these parameters is because they define the source and force vectors of the chemical and mechanical model. Hence, these parameters lie at the core of the model and are the most important driving factors for the differentiation behavior of the cells. The set of parameters we use to produce the model results are summarized in Table 5.1.

Table 5.1: Default parameters for sensitivity analysis

Name	Symbol	Value
Number of cells	C	300
Number of cell boundary nodes	L	23
Number of grid nodes	M	31
Domain length	l_0	3000
Simulation time	T_{max}	1000
Time step	Δt	0.5
Myocyte sourcing rate	γ_1^0	0.5
Adipocyte sourcing rate	γ_1^0	0.5
Myocyte chemical sensitivity	μ_1	$6.6 \cdot 10^3$
Adipocyte chemical sensitivity	μ_2	$6.6 \cdot 10^3$
Myocyte mechanical sensitivity	$\mu_{M,1}$	$3 \cdot 10^4$
Adipocyte mechanical sensitivity	$\mu_{M,2}$	$0.5 \cdot 10^3$
Muscle memory	τ	60
Muscle frequency	f	0.01
Myocyte force magnitude	F_1^0	15

Note that the simulation time, T_{max}, is expressed in minutes which implies that we are modeling $16\frac{2}{3}$ hours. In the coming sensitivity simulations we will look at six variations of a particular parameter, where with each variation we simulate the differentiation process of 300 cells over a time of 1000 minutes. To compare these parameter variations, we show the mean behavior of the cells over time per variation. Hence, in the graphs to come, there will be six lines each plotted with a different color that each represent the mean behavior of

300 cells. Also, to distinguish the different phenotypes in the simulation results, we use dotted lines to denote myocytes and solid lines for adipocyte in line graphs. Further, in the position analysis section, we use the color red to denote myocytes and blue for adipocytes.

5.1.1. SECRETION SENSITIVITY ANALYSIS

In the following section we present the results from the sensitivity analysis on the mentioned parameters. The main idea behind this analysis is to understand the influence that small changes in the force and source function have on the differential behavior of the cell population. Furthermore, this is an excellent method to identify possible strange behaviors in the model, due to implementation errors.

MYOCYTE SECRETION RATE VARIATION

We start by variating the myocyte secretion rate, as stated in Table 5.2. Note that the secretion of adipokines is fixed to 0.5, as stated in the default parameter table 5.1.

Our hypothesis is that as when $\gamma^0_{1,b} \leq \gamma^0_2, b = 1,\dots,6$, we will obtain a cell culture that is dominated by adipocyte tissue. However, we do realize that there are two terms that influence a cell to become a myocyte, while there is only one term that stimulates adipose tissue creation. Hence it is plausible that while the secretion rate of the adipose tissue is dominating we still obtain a majority of myocyte tissue.

The results of this variation in parameters can be found in Figure 5.1 and 5.2.

Table 5.2: Variation of parameters for sensitivity analysis

Symbol name	Value
$\gamma^0_{1,1}$	0.1
$\gamma^0_{1,2}$	0.2
$\gamma^0_{1,3}$	0.3
$\gamma^0_{1,4}$	0.4
$\gamma^0_{1,5}$	0.5
$\gamma^0_{1,6}$	0.6

ADIPOCYTE PHENOTYPE

The variation of the adipocyte secretion rate is given in Table 5.3. Note that the secretion of myokines is fixed to 0.5, as stated in the default parameter table 5.1.

The variation in the secretion rate of the adipose culture is done over a different interval than that of the myocyte culture. This is because myocytes have a benefit from both the chemical and mechanical stimuli, while adipocytes can only benefit from their chemical signaling. Therefore we increase the secreation of adipocytes and try to determine a critical adipokine secretion rate, where lower secretion rates will result in myocyte dominating cell populations and higher secretion rates will have more adipose tissue.

The results of this variation in parameters can be found in Figure 5.3 and 5.4.

Table 5.3: Variation of parameters for sensitivity analysis

Symbol name	Value
$\gamma^0_{2,1}$	0.4
$\gamma^0_{2,2}$	0.6
$\gamma^0_{2,3}$	0.8
$\gamma^0_{2,4}$	1.0
$\gamma^0_{2,5}$	1.2
$\gamma^0_{2,6}$	1.4

5.1.2. FORCE MAGNITUDE SENSITIVITY ANALYSIS

In this section we vary the magnitude of the myocyte force vector with values shown in Table 5.4.

Table 5.4: Variation of parameters for sensitivity analysis

Symbol name	Value
$F^0_{1,1}$	2
$F^0_{1,2}$	4
$F^0_{1,3}$	6
$F^0_{1,4}$	10
$F^0_{1,5}$	20
$F^0_{1,6}$	30

We assume that the effect of this increase in force magnitude is of minor significance, since the effect of the force on the differentiate rate seems to be quite low. This is because there is a long chain of calculations before the actual force 'reaches' the differentiation rate, and even then, by the choice of the scaling function, this effect of the force magnitude could be null.

To recap, in the following chain of calculations, we see how the magnitude of the force is related to the mechanical aging rate.

$$F_1^0 \Rightarrow \underline{F}_1 \Rightarrow \underline{u} \Rightarrow \underline{\underline{\varepsilon}} \Rightarrow \varepsilon_1, \varepsilon_2 \Rightarrow \phi \Rightarrow \psi_M, \max \psi_M \Rightarrow U_M. \tag{5.1}$$

Especially the last step seems to diminish the effect of an increase in myocyte behavior, since we normalize with respect to the maximum sensed stimulus.

The results of this variation in parameters can be found in Figure 5.5.

MYOCYTE SECRETION RATE VARIATION RESULTS

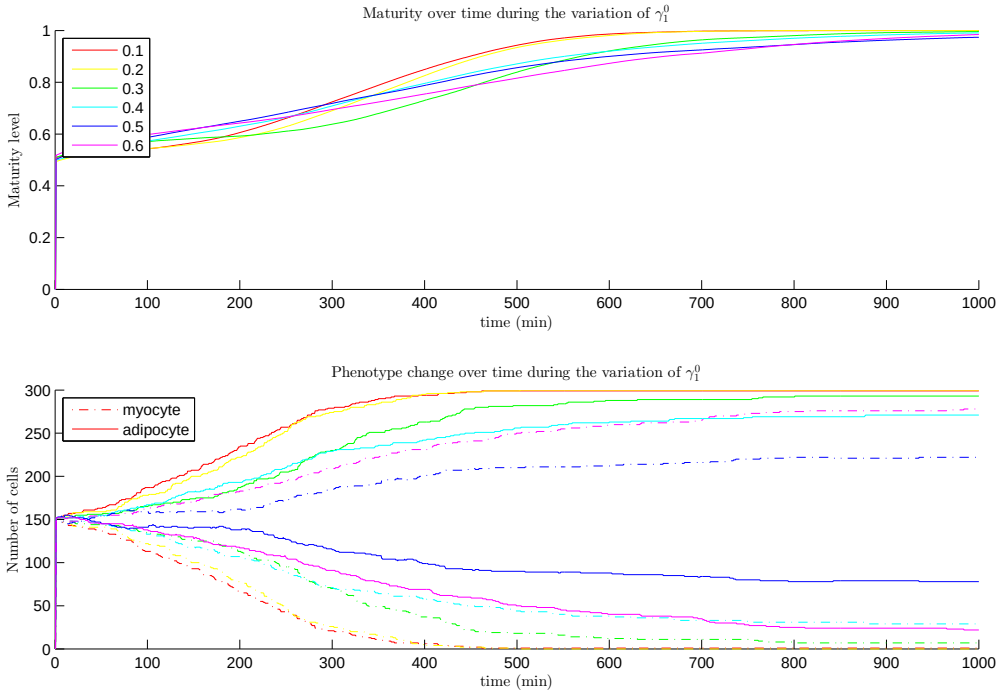

Figure 5.1: Variation of myocyte secretion rate according to legend in top graph. (top) Graph showing the mean behavior of the maturity level of 300 cells over time; (bottom): Graph displaying the distribution of the phenotypes over time.

In the top graph we see that over the course of time the cell population reaches maturity, where for some populations this mean behavior is faster than others. The bottom graph shows the distribution of the cell population per variation of the secretion rate of the myocytes. We see from Figure 5.1 that for myocye secretion rates below 0.5, we obtain an adipocyte dominant cell population. Since the amount of myocytes produces at a secretion rate of 0.5 and 0.4 differs a lot, more research would be needed to determine the exact tipping point of this secretion rate. However, we can expect that this will range between 0.4 and 0.5.

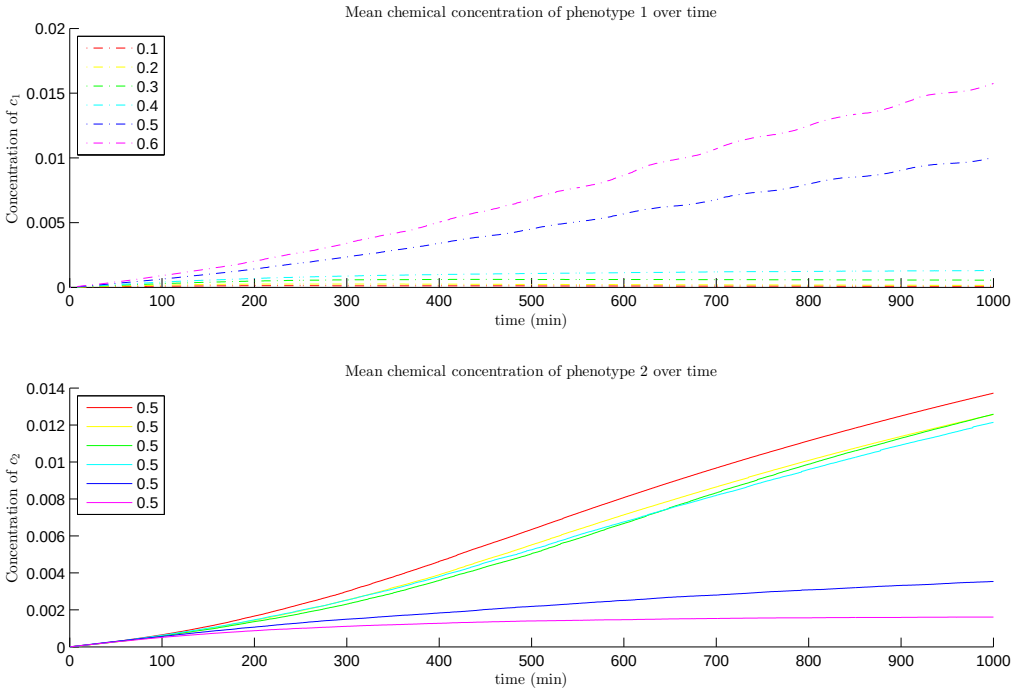

Figure 5.2: Variation of the myocyte secretion rate according to Table 5.2. (top) Graph showing the mean myokine concentration over time, (bottom) Graph showing the mean adipokine concentration over time while keeping the adipocyte secretion rate constant.

In Figure 5.2 we see the mean value of adipokines and myokines sensed by the cells over time. These values represent the expected chemical concentrations when one takes the results from Figure 5.1 into account. Note that in the top graph the order of the plotted concentrations respects the order of the secretion rates given in the legend of that figure. In the bottom graph we see a reverse relation, this is to be expected since when the myocyte population produces little myokines (for example the red line) we also have less myocytes and hence more adipocytes, which results in a larger adipokine concentration. Thus, when the secretion of myokines increases, we see a decrease in adipokine concentration.

ADIPOCYTE SECRETION RATE VARIATION RESULTS

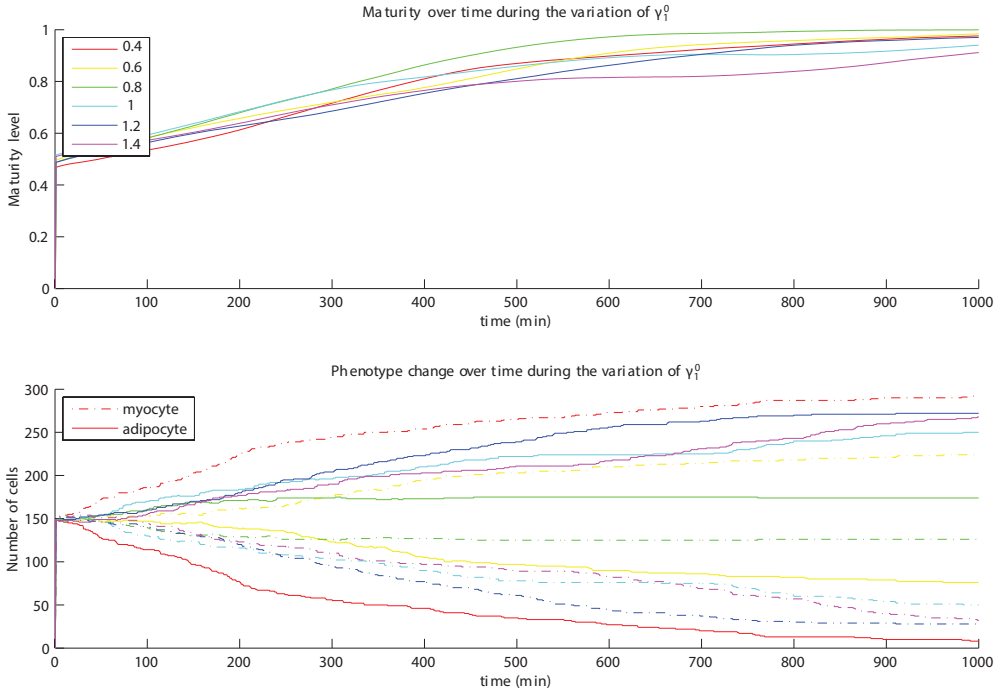

Figure 5.3: Variation of adipocyte secretion rate according to legend in top graph. (top) Graph showing the mean behavior of the maturity level of 300 cells over time; (bottom): Graph displaying the distribution of the phenotypes over time.

In Figure 5.3 we see the mean behavior of the aging rate of 300 cells over time. Compared to the course of change given in Figure 5.1, we see that this situation is less convergent, since after 1000 minutes there are still cell populations which have not fully matured.
However, given the fact that we wanted to find a tipping point, these results give us sufficient information. By inspection, one can see in the bottom graph that for the green line, i.e. an adipocyte secretion rate of 0.8, we obtain a well balanced cell population. For adipocyte secretion rates higher than this value, we see that the adipocytes are more dominant in the cell population. For rates lower than this 0.8, the muscle tissue is dominant.

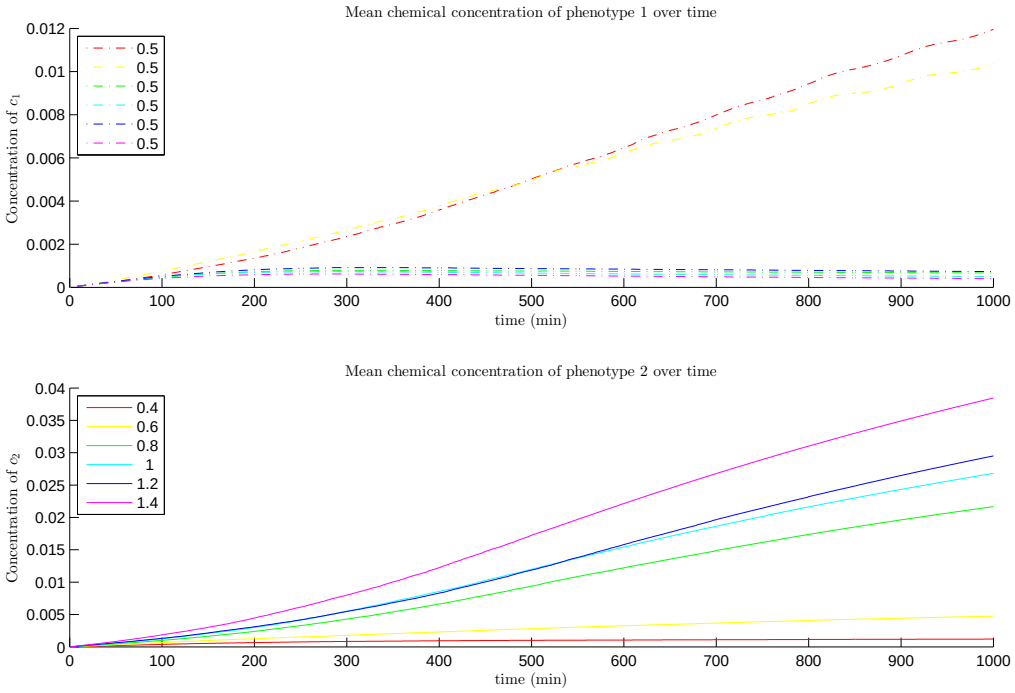

Figure 5.4: Variation of the adipocyte secretion rate according to Table 5.3. (top) Graph showing the mean myokine concentration over time, (bottom) Graph showing the mean adipokine concentration over time while keeping the adipocyte secretion rate constant.

In Figure 5.4 we see in the bottom graph that an increase in the adipocyte secretion rate will result in an overall greater adipokine concentration, in the top figure we see an inverse effect for the myokine concentration sensed by the cells.

From the results given in Figure 5.1 and 5.3, we would like to deduce a relation between the secretion rates of the two phenotypes which will results in a balanced population. From the sensitivity analysis of the myocyte secretion rate, we concluded that when $\gamma_1^0 = 0.45$ and $\gamma_2^0 = 0.5$ we will obtain a balanced cell population. And from the current sensitivity analysis of the adipocyte secretion rate we found that $\gamma_1^0 = 0.5$ and $\gamma_2^0 = 0.8$ will result in a balanced cell population. By taking the fraction between the two secretion rates,

$$b^0 = \frac{\gamma_2^0}{\gamma_1^0} \Rightarrow \frac{0.8}{0.5} = \frac{8}{5} = 1.6, \ \frac{0.5}{0.45} = \frac{10}{9} \approx 1.11, \tag{5.2}$$

hence, from these calculations it seems that it is not possible to set of a relation between the two secretion rates that will result in a balanced cell population.

FORCE MAGNITUDE SENSITIVITY ANALYSIS RESULTS

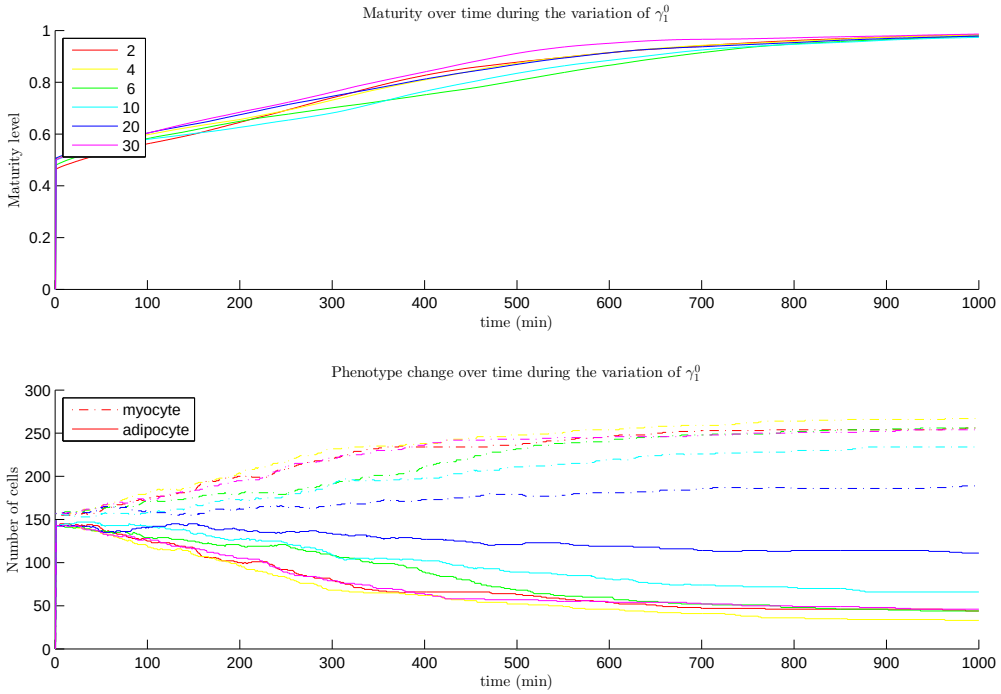

Figure 5.5: Varying the myocyte force magnitude according to Table 5.4. (top) Graph showing the mean behavior of the maturity level of 300 cells over time; (bottom): Here we see the distribution of the phenotypes over time, where the y-axis denotes the number of cells that a certain phenotype is.

We continue the sensitivity analysis by varying the myocyte force function. Here we set the cytokine secretion rates for both phenotypes to 0.5. We should keep in mind that from the previous sensitivity analysis when both secretion rates are set to 0.5, the myocyte population will eventually dominate the cell population. Therefore we will look what lower values of the force magnitude F_1^0 will do to the creation of muscle tissue.

From Figure 5.5 we see that this has little effect on the composition of the cell population, since in all variations the myocytes still dominates the cell population. However, there are some small variations in the amount of myocyte that are eventually produced. For example, when $F_1^0 = 4$, we obtained the most myocytes, when $F_1^0 = 20$ we got the least and with $F_1^0 = 30$ we had something in between. This could mean that there are sub-optimal choices for the force magnitude F_1^0, however, more research is needed in order to verify this behavior of the model.

5.2. POSITION ANALYSIS

Besides the differentiation behavior, we are also interested in the positioning of the cells at the end of the simulation. In this section we will show the positions of the cells after a simulation of 1000 minutes, where the same parameters are used as proposed in Table 5.1.

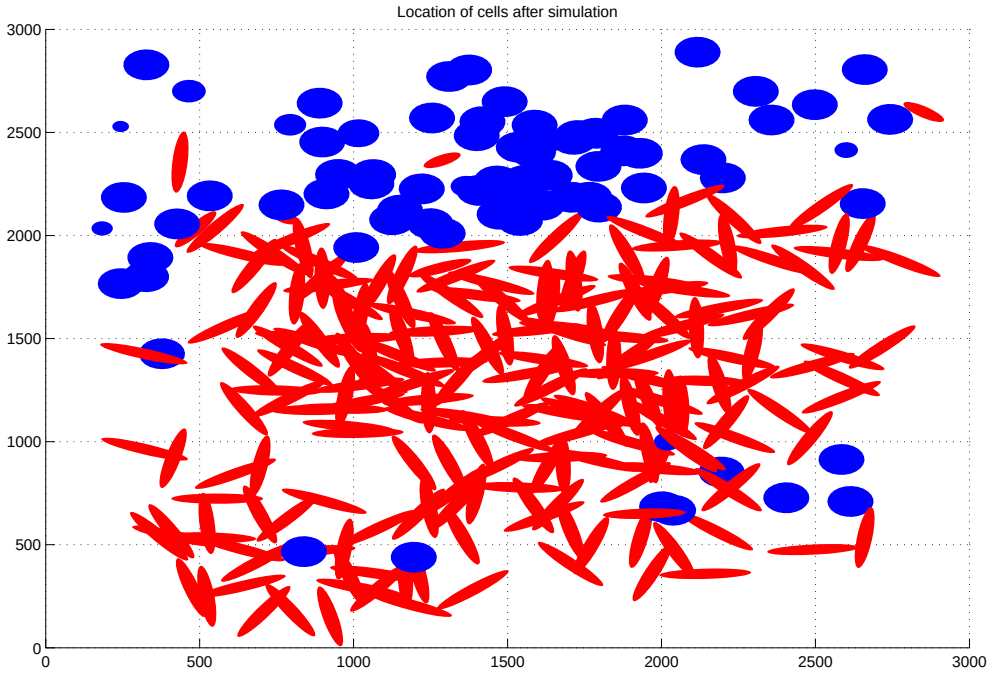

Figure 5.6: Cell position when $\gamma_1^0 = 0.4$ and $\gamma_2^0 = 0.5$

Figure 5.6 shows the position of cells when the simulation has ended, hence after 1000 simulation minutes. Notice the clear myocyte cluster which is surrounded by some scattered adipocytes, where some adipocytes are intertwined in the myocyte cluster. We would like to note how this formation has come to being, since the process prior to this composition also contains valuable information.

During the simulation, the movement of most cells is being dominated by the random walk and the chemical gradient. This chemical gradient causes cells to form dense clusters, which are self-sustaining since more cells gather around these clusters and keep secreting their cytokine. The movement due to haptotaxis is of minor significance in the early parts of the simulation, but becomes more important when the cells have matured.

This is because the movement due to chemotaxis and randomness is dependent on the maturity level, once a cell has matured it is no longer subject to these influences. Hence, then the movement of cells is dominated by haptotaxis, which causes the cells to spread out and reduce the amount of dense clusters.

6

RESULTS FROM THE NOVEL MODEL APPROACH IN 3D

Extending the model towards three dimensions was, from a theoretical point of view, a doable task. The implementation of this three dimensional version required some more attention than expected. However, since we were able to extend most parts of the 2D model towards 3D, we would like to present some preliminary results of the 3D version of the model.
However we cannot justify the correctness of the results presented here, since this code is more susceptible to implementation errors than the 2D version, which is mainly due to inexperience with the 3D model. In the near future, we would first like to attempt validation techniques on the methods used in the 3D model before appropriate model results can be produced. For example, we have not validated the 3D version of the chemical and mechanical model, and we were unable to implement the equation for rotation of the cells.
Under these circumstance we will continue with the sensitivity analysis on the same set of parameters as with the 2D model. Thereafter, we also discuss the positioning of the cells after a simulation.

6.1. SENSITIVITY ANALYSIS

The sensitivity analysis will again be concerned with the secretion rates of both phenotypes and the force magnitude of the myocytes. For the coming simulations we will use the set of parameters, given in Table 6.1, to start the simulations.

Table 6.1: Default parameters for sensitivity analysis

Name	Symbol	Value
Number of cells	C	300
Number of cell boundary nodes	L	6
Number of grid nodes	M	6
Domain length	l_0	3000
Simulation time	T_{sim}	1000
Time step	Δt	0.5
Myocyte sourcing rate	γ_1^0	0.5
Adipocyte sourcing rate	γ_1^0	0.5
Myocyte chemical sensitivity	μ_1	$6.6 \cdot 10^3$
Adipocyte chemical sensitivity	μ_2	$6.6 \cdot 10^3$
Myocyte mechanical sensitivity	$\mu_{M,1}$	$1 \cdot 10^4$
Adipocyte mechanical sensitivity	$\mu_{M,2}$	$0.5 \cdot 10^3$
Muscle memory	τ	60
Muscle frequency	f	0.01
Myocyte force magnitude	F_1^0	15

The range of variations that we view per parameter might be different from the 2D case, which is not intentional. Because the 2D model is faster than the 3D version, since less computations are needed, and because

we have worked with the 2D model slightly longer, we were able to analyze more variations and see which range showed the best results. We were unable to do the same for the 3D model, partly because of its incompleteness, its long computational time and due to the fact that we have implemented this model in a late stage of this thesis project.

6.1.1. SECRETION SENSITIVITY ANALYSIS

This section introduces the variations of the secretion rate parameters in a similar manner as the 2D case.

MYOCYTE SECRETION RATE VARIATION

Table 6.2: Variation of parameters for sensitivity analysis

Symbol name	Value
$\gamma^0_{1,1}$	0.2
$\gamma^0_{1,2}$	0.3
$\gamma^0_{1,3}$	0.4
$\gamma^0_{1,4}$	0.5
$\gamma^0_{1,5}$	0.6
$\gamma^0_{1,6}$	0.7

We vary the myocyte secretion rate according to Table 6.2, the results of this variation can be found in Figure 6.1 and 6.2.

ADIPOCYTE PHENOTYPE

Table 6.3: Variation of parameters for sensitivity analysis

Symbol name	Value
$\gamma^0_{2,1}$	0.5
$\gamma^0_{2,2}$	0.6
$\gamma^0_{2,3}$	0.7
$\gamma^0_{2,4}$	0.8
$\gamma^0_{2,5}$	0.9
$\gamma^0_{2,6}$	1.0

We vary the adipocyte secretion rate according to Table 6.3, the results of this variation can be found in Figure 6.3 and 6.4.

6.1.2. FORCE MAGNITUDE SENSITIVITY ANALYSIS

Table 6.4: Variation of' parameters for sensitivity analysis

Symbol name	Value
$F^0_{1,1}$	5
$F^0_{1,2}$	10
$F^0_{1,3}$	15
$F^0_{1,4}$	20
$F^0_{1,5}$	25
$F^0_{1,6}$	30

We vary the adipocyte secretion rate according to Table 6.4, the results of this variation can be found in Figure 6.5.

MYOCYTE SECRETION RATE VARIATION RESULTS

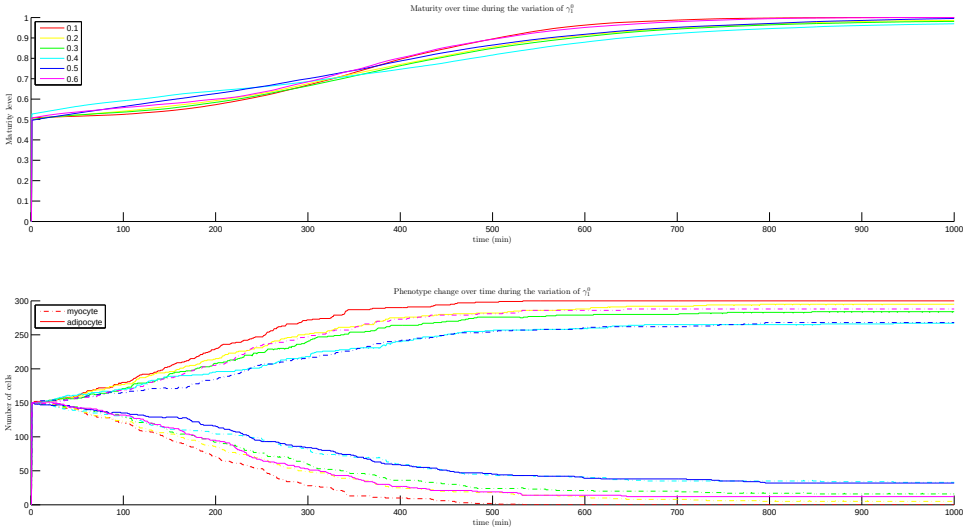

Figure 6.1: Variation of myocyte secretion rate according to legend in top graph. (top) Graph showing the mean behavior of the maturity level of 300 cells over time; (bottom): Graph displaying the distribution of the phenotypes over time.

In Figure 6.1 we see the mean age behavior of the simulated cells in the top graph, the bottom graph shows the distribution of both phenotypes over time. From this bottom graph we see a clear distinction between the chosen variations, since when $\gamma_1^0 \geq 0.5$ the cell population will be dominated by myocytes. Secretion rates below this value show an adipose dominant cell population. This is in close relation with the two dimensional version of the model, which verifies in some sense the correctness of the extension towards three dimensions.

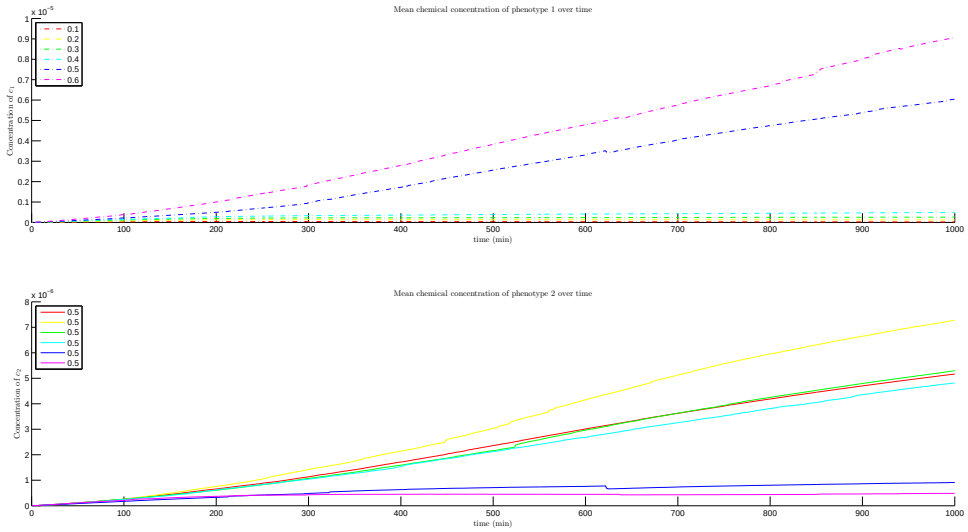

Figure 6.2: Variation of the myocyte secretion rate according to Table 6.2. (top) Graph showing the mean myokine concentration over time, (bottom) Graph showing the mean adipokine concentration over time while keeping the adipocyte secretion rate constant.

In Figure 6.2 we see the mean chemical concentrations sensed by the cells over time. These result here reflect the behavior we expect, for example, the magenta line should represent the highest concentration when we look at the myokine concentration since in that case we had the most myocytes. Therefore we have in that case that the chemical concentration of the adipokine should be the lowest.
However, there is some remarkable behavior, and that is the 'jumps' in the chemical concentrations in some cases. We would expect that this is accompanied by a sudden phenotype change, but this is not apparent from the bottom graph of Figure 6.1. Another reason could lie in the way we correct cells that move outside the domain. The method we have used looks each time step, after the update of the variables, if any cell boundary node would lies outside the domain. If so, it then identifies which cell is responsible for this and then resets the location of its cell center, and hence all its cell boundary nodes. It is possible that this process caused a cell to be spawned in a cluster of myocytes, which then explains the sudden increase in sensed myokine concentration and the drop of sensed adipokine concentration.
But if that is the case, we would expect the same behavior in the 2D model, but we know that we have not observed this behavior in that case. So it might be because this change is more apparent in the 3D version, or there is another unkown reason which causes these jumps.

ADIPOCYTE SECRETION RATE VARIATION RESULTS

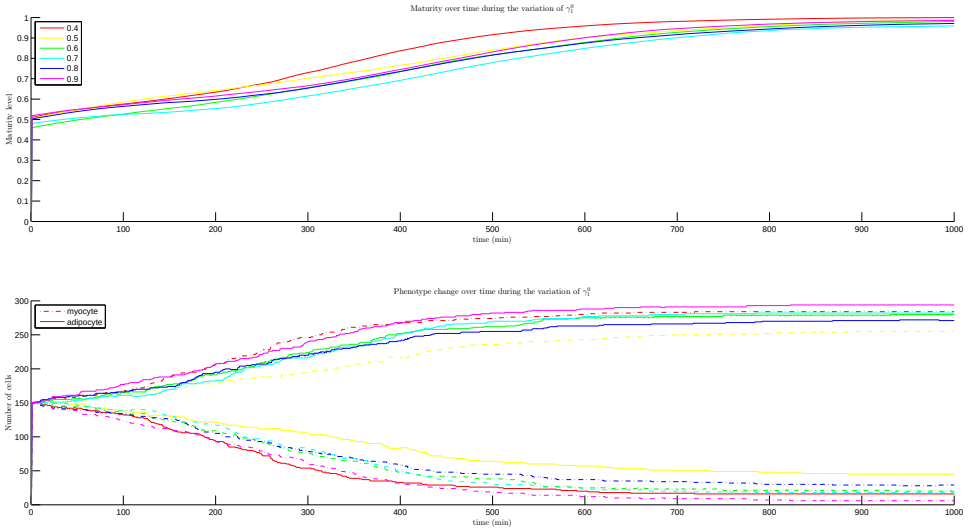

Figure 6.3: Variation of adipocyte secretion rate according to legend in top graph. (top) Graph showing the mean behavior of the maturity level of 300 cells over time; (bottom): Graph displaying the distribution of the phenotypes over time.

In Figure 6.3 we see the change of the population's mean age in the top graph and the composition of the cell population in the bottom graph. Again we have some interesting model results, since the red and yellow line (i.e. $\gamma_2^0 = 0.4, 0.5$) still show an myocyte dominant cell composition. However, when we increase the adipocyte secretion rate beyond this point, thus $\gamma_2^0 > 0.5$, we obtain an adipocyte dominant cell population. Compared to the two dimension version, we see that we obtain a similar results but not identical. What is also noteworthy is the behavior of these extreme cell population compositions, compared to the two dimensional case. By this we mean that in the 3D version we hardly obtain a 50-50 cell population composition, whereas in the 2D case this was more the norm than the exception.

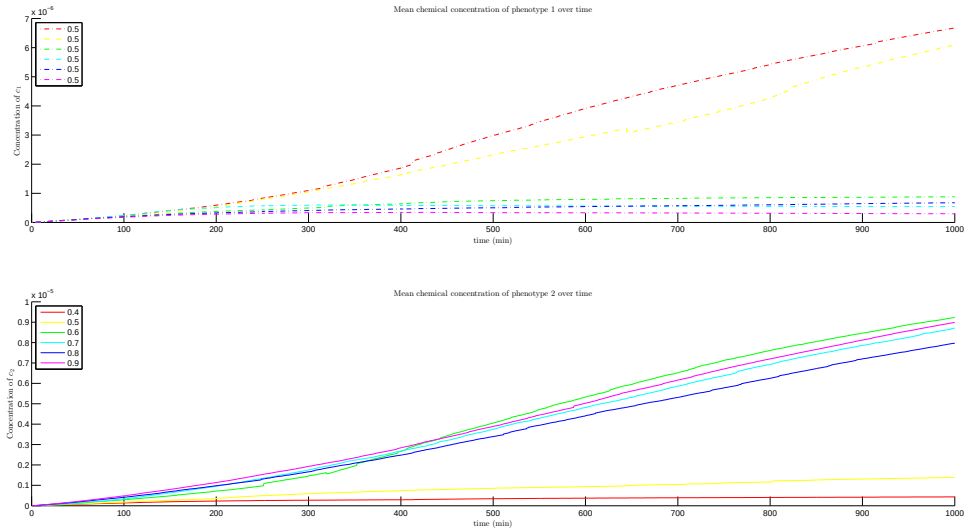

Figure 6.4: Variation of the adipocyte secretion rate according to Table 5.3. (top) Graph showing the mean myokine concentration over time, (bottom) Graph showing the mean adipokine concentration over time while keeping the adipocyte secretion rate constant.

The chemical concentrations show again results which we expect if we look at the graphs in Figure 6.3. From the results given in Figure 6.1 and 6.3, we would like to deduce a relation between the secretion rates of the two phenotypes which will results in a balanced population. From the sensitivity analysis of the myocyte secretion rate, we concluded that when $\gamma_1^0 = 0.4$ and $\gamma_2^0 = 0.5$ we will obtain a balanced cell population. And from the current sensitivity analysis of the adipocyte secretion rate we found that $\gamma_1^0 = 0.5$ and $\gamma_2^0 = 0.6$ will result in a balanced cell population. By taking the fraction between the two secretion rates,

$$b^0 = \frac{\gamma_2^0}{\gamma_1^0} \Rightarrow \frac{0.6}{0.5} = \frac{6}{5} = 1.2, \ \frac{0.5}{0.4} = \frac{5}{4} \approx 1.25, \tag{6.1}$$

hence, from these calculations it seems that we can state a relation between the two secretion rates that can result in a semi-balanced cell population. We state semi-balanced here because of the extreme composition results. However, this ratio should be used as a guideline, or rule of thumb, than as some result of a proof.

FORCE MAGNITUDE SENSITIVITY ANALYSIS RESULTS

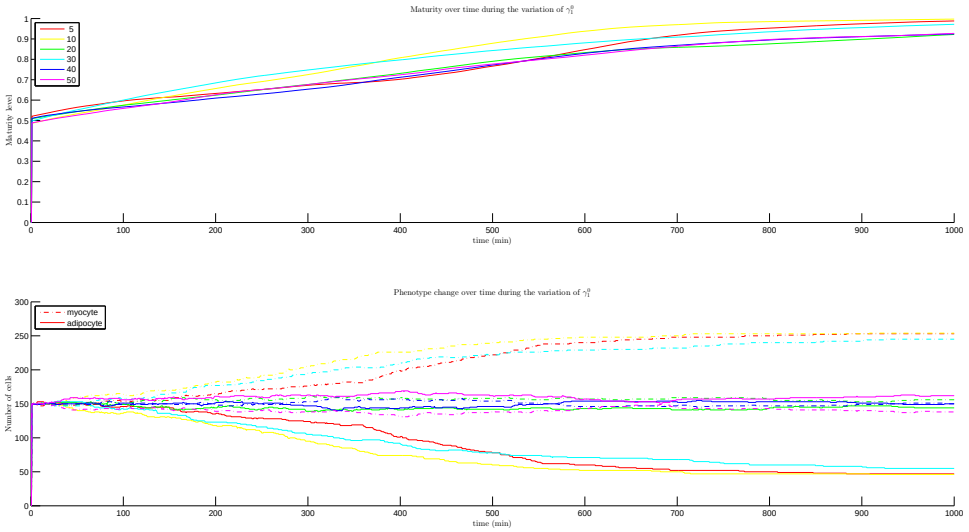

Figure 6.5: Varying the myocyte force magnitude according to Table 6.4. (top) Graph showing the mean behavior of the maturity level of 300 cells over time; (bottom): Here we see the distribution of the phenotypes over time, where the y-axis denotes the number of cells that a certain phenotype is.

In the bottom graph of Figure 6.5, we see the composition of the cell population over time. Compared to Figure 5.5, we have obtained a very unusual result here, since there is a strange mixture between which variations of the parameter F_1^0 resulted in a myocyte dominant population and which did not. To recap, the values $F_1^0 = 5, 10, 30$ gave a myocyte dominant population, while all the other values gave an almost exact 50-50 cell population composition as a result.
Since these result seem so irregular, we are unable to give a solid conclusion. Hence, more research is needed on this variation.

6.2. POSITION ANALYSIS

In Figure 6.6 we see the graphical representation of the cells' position after the simulation which corresponds with the purple line in Figure 6.1. By inspection, one sees immediately that the fat cell population is dominating the cell population. In between the fat cells, one can find some muscle cells.

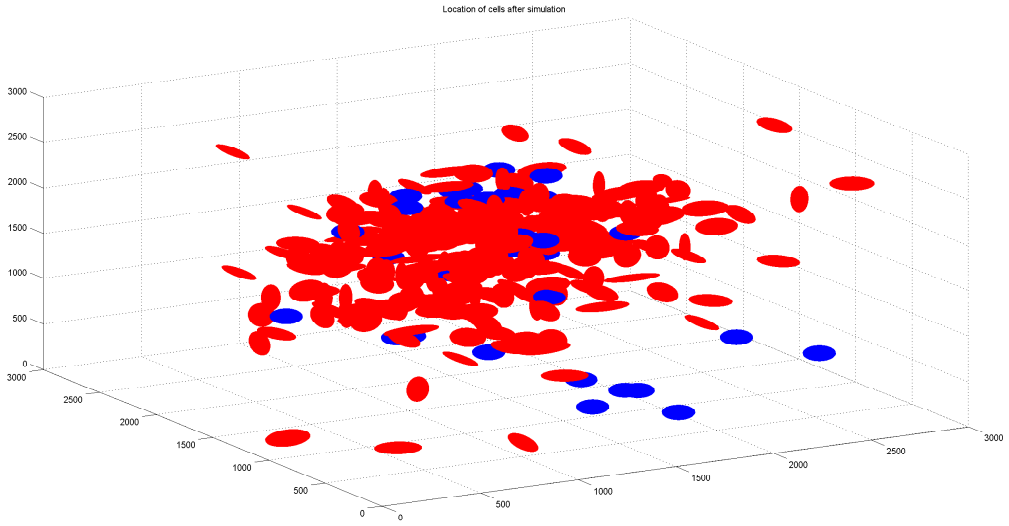

Figure 6.6: Cell position which corresponds with the purple line (i.e. $\gamma_1^0 = 0.6$) of Figure 6.1.

Note however that there has been no change of orientation of any cell during the simulation, since there was no more time left to implement this into the 3D model. Compared to the 2D case, there is less clustering of fat cells, however the distribution of the cells also seems more random. We would need more time to investigate how the movement parameters affect the cell movement in 3D, since it is apparent that they have a different influence because of the large difference in cell position compared to the 2D case of Figure 5.6.

7

Discussion

Chapter 5 presented some results from the 2D version of the model, and Chapter 6 did the same but for the 3D version of the model. In this section we will discuss these results and make small notes on how to improve the model for future reference. A more detailed list of the action can be found in Chapter 8.
We will start this discussion by evaluating the goal of this thesis. We started this project to think of a novel model approach for (stem) cell differentiation, where we eventually used an innovative way of modeling differentiation and cell movement. Since here we see cell differentiation as a gradual process, instead of a discrete one which is commonly used in other models, and the cell movement is based on discrete cell entities that can move around during the simulation, instead of cell densities that flow through the domain.
These model choices were made to allow us to simulate a certain amount of detail during the process of cell differentiation. We assume that this detail is needed to eventually be able to model more complex cell phenomena, like the fusion of myoblasts or cell division.
The results obtain from the 2D and 3D model are not sufficient enough to aid true cell biologist, yet. However, the results are useful for a mathematician that wants to validate its model based on the behavior it expects.
Further, we are obliged to note some flaws or strange mathematical quirks that reside in the model. We start by discussing the movement of the cells. As stated in Section 4.3, a cell moves under the influence of randomness, chemotaxis and haptotaxis, which we see as realistic influences of cell movement. However, the choice of parameters that determine the sensitivity towards these type of movement is crucial for the simulation results. From our experience, it was difficult to find parameter values that were obtained from cell biology papers, hence we were forced to attempt a trial and error method to find reasonable simulation results. This is of course not an ideal approach. Further, we have also experienced that the same motility parameters used in the 2D case, do not result in a similar behavior of movement for the 3D case.
Also, as already discussed in the parameter section 4.5, the choice for the scaling function (see equation 4.50) is also doubtful. Note that the scaling functions were used to limit the rate of differentiation of the cells, however finding an alternative scaling function was a difficult task when taking into account the way a cell can act and sense its environment. A possible adaption that can be made to simulate the differentiation rate in a different way, is by allowing cells to (re)enter the cell cycle which then causes cells to differentiate after the mitotic phase. In that case, the maturity of a cell does not change each time step, but each time a cell exits the cell cycle. Now the rate of differentiation will no longer be determined by functions $U_c^i(t)$ or $U_M^i(t)$, but by a stochastic (differential) equation which incorporates the mechanical and chemical stimuli, for example. However, this is just a speculation on how cell differentiation could also be simulated.
In conclusion we can say that from a biological point of view, we have not yet obtained a useful model that could aid cellular biologists. However, from a mathematical point of view, we have obtained the basis of a model that is able to be extended to an even more complex system. For the improved version of the current model, we believe that it will be possible to simulate the formation and change of tissue for bone, fat and muscle cells.

8

FUTURE WORK

In the previous chapter we have concluded our work with some remarks on how to improve the model. In this chapter we will elaborate on these remarks and also note more possible extensions as well as future plans of the model. This chapter is mostly designed for the successor that will continue with this proposed model. The possible extension we would like to see in the near future are given below.

- Introduce a new phenotype, the bone cell. Pay attention to the definition of the mechanical stimuli and the way to identify this cell's behavior with the Fourier Transform;
- Simulate a more detailed version of myogenesis. In this thesis there has been no distinction between myoblasts, myotubes and myocytes, these are all considered to be one entity which grows stronger over time. We would like to improve the model to be able to fuse cells together. However, obtaining this fusing model is no straightforward task, since for example one has to be concerned with the position of fusion and the equation of movement after two (or more) cells have fused. Moreover, this fusion model can also be used to fuse muscle tissue to bone tissue.;
- Introduce the cell cycle, see [31] or [20] for inspiration. We see this addition as a key factor in being able to simulate the change of existing tissue over time.;
- Introduce interaction between fat cells and muscle cells, i.e. burning and formation of fat due to muscular (in)activity.

Especially for the successor that continues with this model, we would like to point out the following errors and improvements one can make to the model.

- Find an appropriate way to deal with cells that move out the domain of computation;
- Validation of 3D models and functions used;
- Rotation and movement limitation. In the current thesis we did not limit the actual movement speed of the cells, likewise, a cell also should have a limit in its rotation speed.

We expect that this model approach is able to eventually simulate the development of bone, fat and muscle formation, but also to simulate the change of certain tissue over time. We believe that there is a possibility that this model can aid in the understanding of cell differentiation, but also that it can be helpful for educational purposes.
Further, we would like to see the continuation in the development of the 2D and the 3D model, since both have their advantages and disadvantages. The 2D model preserves a certain simplicity and low computational cost, while the 3D model is by definition more realistic but can be harder to handle due to the high computational cost.

A

APPENDIX

A.1. DERIVATION OF THE RELATION BETWEEN STRESS AND DISPLACEMENT

This section explains the relation between the displacement and the stress tensor in three dimensions. First we define the relation between the strain tensor and the displacement vector in the infinitesimal strain theory

$$\underline{\underline{\varepsilon}} = \frac{1}{2}(\nabla \underline{u} + (\nabla \underline{u})^T), \tag{A.1}$$

where

$$\nabla \underline{u} = \begin{bmatrix} \frac{\partial}{\partial x} \\ \frac{\partial}{\partial y} \\ \frac{\partial}{\partial z} \end{bmatrix} \begin{bmatrix} u(\underline{x}) & v(\underline{x}) & w(\underline{x}) \end{bmatrix} = \begin{bmatrix} u_x & v_x & w_x \\ u_y & v_y & w_y \\ u_z & v_z & w_z \end{bmatrix}. \tag{A.2}$$

Here $u(\underline{x})$, $v(\underline{x})$ and $w(\underline{x})$ denote the displacement in the $x-$, $y-$ and $z-$direction.
From this we gain an explicit view on the strain-displacement relation

$$\underline{\underline{\varepsilon}} = \begin{bmatrix} u_x & \frac{1}{2}(u_y + v_x) & \frac{1}{2}(w_x + u_z) \\ \frac{1}{2}(u_y + v_x) & v_y & \frac{1}{2}(w_y + v_z) \\ \frac{1}{2}(w_x + u_z) & \frac{1}{2}(w_y + v_z) & w_z \end{bmatrix}. \tag{A.3}$$

By Hooke's law there is also a stress-strain relation

$$E \begin{bmatrix} \varepsilon_{11} \\ \varepsilon_{22} \\ \varepsilon_{33} \\ \varepsilon_{12} \\ \varepsilon_{23} \\ \varepsilon_{13} \end{bmatrix} = \begin{bmatrix} 1 & -\nu & -\nu & 0 & 0 & 0 \\ -\nu & 1 & -\nu & 0 & 0 & 0 \\ -\nu & -\nu & 1 & 0 & 0 & 0 \\ 0 & 0 & 0 & 1+\nu & 0 & 0 \\ 0 & 0 & 0 & 0 & 1+\nu & 0 \\ 0 & 0 & 0 & 0 & 0 & 1+\nu \end{bmatrix} \begin{bmatrix} \sigma_{11} \\ \sigma_{22} \\ \sigma_{33} \\ \sigma_{12} \\ \sigma_{23} \\ \sigma_{13} \end{bmatrix}. \tag{A.4}$$

Taking the inverse leads to

$$\begin{bmatrix} \sigma_{11} \\ \sigma_{22} \\ \sigma_{33} \\ \sigma_{12} \\ \sigma_{23} \\ \sigma_{13} \end{bmatrix} = \frac{E}{(1+\nu)(1-2\nu)} \begin{bmatrix} 1-\nu & \nu & \nu & 0 & 0 & 0 \\ \nu & 1-\nu & \nu & 0 & 0 & 0 \\ \nu & \nu & 1-\nu & 0 & 0 & 0 \\ 0 & 0 & 0 & 1-2\nu & 0 & 0 \\ 0 & 0 & 0 & 0 & 1-2\nu & 0 \\ 0 & 0 & 0 & 0 & 0 & 1-2\nu \end{bmatrix} \begin{bmatrix} \varepsilon_{11} \\ \varepsilon_{22} \\ \varepsilon_{33} \\ \varepsilon_{12} \\ \varepsilon_{23} \\ \varepsilon_{13} \end{bmatrix}. \tag{A.5}$$

Rewriting this into matrix format, we obtain

$$\underline{\underline{\sigma}} = \frac{E}{(1+\nu)(1-2\nu)} \begin{bmatrix} \varepsilon_{11}(1-\nu) + \varepsilon_{22}\nu + \varepsilon_{33}\nu & \varepsilon_{12}(1-2\nu) & \varepsilon_{13}(1-2\nu) \\ \varepsilon_{12}(1-2\nu) & \varepsilon_{11}\nu + \varepsilon_{22}(1-\nu) + \varepsilon_{33}\nu & \varepsilon_{23}(1-2\nu) \\ \varepsilon_{13}(1-2\nu) & \varepsilon_{23}(1-2\nu) & \varepsilon_{11}\nu + \varepsilon_{22}\nu + \varepsilon_{33}(1-\nu) \end{bmatrix}. \tag{A.6}$$

And using the strain-displacement relation from equation A.1, we get

$$\underline{\underline{\sigma}} = \frac{E}{(1+\nu)(1-2\nu)} \begin{bmatrix} u_x(1-\nu)+v_y\nu+w_z\nu & \frac{1}{2}(1-2\nu)(u_y+v_x) & \frac{1}{2}(1-2\nu)(w_x+u_z) \\ \frac{1}{2}(1-2\nu)(u_y+v_x) & u_x\nu+v_y(1-\nu)+w_z\nu & \frac{1}{2}(1-2\nu)(w_y+v_z) \\ \frac{1}{2}(1-2\nu)(w_x+u_z) & \frac{1}{2}(1-2\nu)(w_y+v_z) & u_x\nu+v_y\nu+w_z(1-\nu) \end{bmatrix}. \tag{A.7}$$

A.2. THE FINITE ELEMENT METHOD

This section is meant to give a short introduction to the method we use to solve our mathematical models. We will leave out most mathematical details that are concerned with this method and try to transmit the idea of this method.

With a boundary value problem (BVP), one also has the (partial) differential equations that give the solution in an abstract sense.
In this thesis we used the Finite Element Method (FEM) to approximate the solution of the (partial) differential equations. There are two ways to apply the finite element method to a problem. The first one is by finding the corresponding minimization problem to the PDE's, and then apply Ritz' method. The other one is by calculating the weak form of the PDE, and the apply Galerkin's method.
Both ways give a similar result when it is possible to find a corresponding minimization problem, since this is not always the case. The conditions under which we can say that a boundary value problem has an equivalent minimization problem are given below, where L represents the operator of the boundary value problem.

- symmetry (self ad-jointness) of the operator L of the BVP:

$$\int_\Omega uLvd\Omega = \int_\Omega vLud\Omega, \forall u, v \in \Sigma. \tag{A.8}$$

- positiveness of the operator L:

$$\int_\Omega uLvd\Omega \geq 0, \forall u \in \Sigma. \tag{A.9}$$

With Σ the solution space. If these conditions are met, then we say that the operator L is strongly elliptic. In section A.3.1 we show that the problem given by equation 4.13 is strong elliptic and thus there will be no difference in applying Galerkin's or Ritz' method to solve the model given by equation 4.13.

We continue with a brief explanation on how we use the FEM with Galerkin's method for a general problem. In sections A.3 and A.4, we show how the FEM applies to our models.
The first step in the FEM when we are going to use Galerkin's method, is to derive the weak form of the PDE. This is done by multiplying the partial differential equation by a test function $\phi \in \mathscr{H}^1$, which comes from a Hilbert space, and then integrate this product over the domain of computation Ω. By using integration by parts, we are able lower the order of the partial differential equation.
The next step is to approximate the solution by an unknown linear combination of N basis functions and also discretize the domain Ω by these N points. The basis functions have a compact support around its specific node in the mesh. Eventually we want to obtain this yet unknown linear combination, because once this is known we have our solution.
The set of basis functions comes from the Hilbert space and must be linearly independent and complete, so that this set forms a basis for the Hilbert space in the limit. The test function $\phi(x)$ is also expanded in a series of basis functions, but because our test function is arbitrary, we use $\phi(x) = \phi_i(x), i = 1, \ldots, N$ [32, p.123-124].
The definition of these basis functions is a crucial step in the FEM. In this thesis we used piecewise linear basis functions for the FEM, which are defined as

- $\phi_i(\underline{x})$ is linear per element, $i = 1, \ldots, N$
- $\phi_i(\underline{x}_j) = \delta_{ij}$, $i, j = 1, \ldots, N$

where $\underline{x}_j$ is the coordinate of the j^{th} node and where the element comes from the discretization of the domain with N points, from this discretization we can construct M elements, which are finite.
Despite the other ways that are available to define the basis functions, we restrict ourselves to piecewise linear basis functions. This means that when we work on a two dimensional domain, we will use the following formulation

$$\phi_i(\underline{x}) = a_0^i + a_1^i x + a_2^i y. \tag{A.10}$$

While on a three dimensional domain our basis functions are given by

$$\phi_i(\underline{x}) = a_0^i + a_1^i x + a_2^i y + a_3^i z \tag{A.11}$$

Note that by using these piecewise linear functions as basis functions, we will obtain an accuracy of order $\mathcal{O}(h^2)$, where h is the uniform grid size. The coefficients a_k^i are determined by the dimensions of the element in which node i lies.
Since we have obtained the weak form of the BVP, and approximated the solution and the test functions by a set of basis functions, we are now able to solve the problem for these N unknowns. However, the integrals obtained from the weak form are taken over the whole domain Ω, which are difficult to calculate. A much easier approach is to integrate over each element Ω_e, considering the nifty definition of the basis functions. By this approach, we can treat every element independently which results in a so called *element matrix* and *element vector* per element.
After the calculation of all the element matrices and vectors for each element, we can assembly a large matrix which contains all the information of these element matrices and vectors, and thus summarized our PDE into one large system. We can then solve this system for the unknown coefficients which we used to approximate the solution in its basis functions.

A.3. DERIVATION OF THE THE WEAK FORMULATION OF THE MECHANICAL MODEL

The three dimensional mechanical model is defined as

$$\nabla \underline{\underline{\sigma}} + \underline{F} = 0, \quad \underline{x} \in \Omega, \tag{A.12}$$

$$\underline{\underline{\sigma}} \cdot \underline{n} + K\underline{u} = 0, \quad \underline{x} \in \partial\Omega. \tag{A.13}$$

To obtain the weak form of equation A.12, we use an element-wise approach. Hence, we continue by deriving the weak form of the x, y and z components of equation A.12. However, since these derivations use a similar approach, we will only show the calculations for the weak form of the x-component, followed by the result of the weak form for the y and z components for completeness.
The x component version of equation A.12 is given by

$$\nabla \cdot \underline{\sigma}_x + F_x = 0, \quad \underline{x} \in \Omega, \tag{A.14}$$

$$\underline{\sigma}_x \cdot \underline{n} + Ku = 0, \quad \underline{x} \in \partial\Omega. \tag{A.15}$$

where $\underline{\sigma}_x$ is the first row (or column) of equation A.7.
In order to deduce the weak form of equation A.14 we multiply the equation by a test function $\phi(\underline{x})$ and then integrate over the domain Ω.

$$\int_\Omega (\nabla \cdot \underline{\sigma}_x)\phi \, d\Omega + \int_\Omega F_x \phi \, d\Omega = 0, \quad \underline{x} \in \Omega. \tag{A.16}$$

Applying Green's theorem on the first integral, gives

$$-\int_\Omega \nabla\phi \cdot \underline{\sigma}_x \, d\Omega + \int_{\partial\Omega} \phi(\underline{\sigma}_x \cdot \underline{n}) \, d\Gamma + \int_\Omega F_x \phi \, d\Omega = 0, \quad \underline{x} \in \Omega. \tag{A.17}$$

This can be simplified by using the boundary condition A.13. We then get:

$$-\int_\Omega \nabla\phi \cdot \underline{\sigma}_x \, d\Omega - K\int_{\partial\Omega} \phi u \, d\Gamma + \int_\Omega F_x \phi \, d\Omega = 0, \quad \underline{x} \in \Omega, \tag{A.18}$$

$$\int_\Omega \nabla\phi \cdot \underline{\sigma}_x \, d\Omega + K\int_{\partial\Omega} \phi u \, d\Gamma = \int_\Omega F_x \phi \, d\Omega, \quad \underline{x} \in \Omega. \tag{A.19}$$

The next step in the FEM process is to approximate the domain integral by discrete elements $\Omega_e, e = 1, \ldots, M$ and the boundary integral by discrete boundary elements $\Omega_{be}, be = 1, \ldots, M_{be}$.

$$\sum_{e=1}^{M} \int_{\Omega_e} \nabla\phi \cdot \underline{\sigma}_x \, d\Omega + K \sum_{be=1}^{M_{be}} \int_{\partial\Omega_{be}} \phi u \, d\Gamma = \sum_{e=1}^{M} \int_{\Omega_e} F_x \phi \, d\Omega, \quad \underline{x} \in \Omega. \tag{A.20}$$

Now we will approximate the solution and the test function, by a series of basis functions

$$u(\underline{x}) = \sum_{j=1}^{N} u_j \phi_j(\underline{x}), \quad v(\underline{x}) = \sum_{j=1}^{N} v_j \phi_j(\underline{x}), \tag{A.21}$$

$$w(\underline{x}) = \sum_{j=1}^{N} w_j \phi_j(\underline{x}), \quad \phi(\underline{x}) = \phi_i(\underline{x}), i = 1, \ldots, N, \tag{A.22}$$

and substitute this back into equation A.20.

$$\sum_{e=1}^{M} \int_{\Omega_e} \nabla\phi_i \cdot \underline{\sigma}_x \, d\Omega + K \sum_{be=1}^{M_{be}} \sum_{j=1}^{N} u_j \int_{\partial\Omega_{be}} \phi_i \phi_j \, d\Gamma = \sum_{e=1}^{M} \int_{\Omega_e} F_x \phi_i \, d\Omega, \quad \underline{x} \in \Omega, i = 1, \ldots, N. \tag{A.23}$$

These integrals in equation A.23 can be greatly reduced in complexity if we focus on one element e, or boundary element be. This is because of the nifty definition of the basis functions $\phi(\underline{x})_i$. However, in this process we need to be careful with the notation of the grid node we are on, since every basis function is defined on each element differently. Therefore, we denote the nodes of an element e by the bold-face index $\mathbf{i} = 1, 2, 3, 4$.

The first integral from equation A.23 is given by

$$\int_{\Omega_e} (\nabla \phi_{\mathbf{i}}) \cdot \underline{\sigma}_x \, d\Omega, \mathbf{i} = 1, \ldots, 4 \tag{A.24}$$

Which is equal to

$$E_v \int_{\Omega_e} \begin{bmatrix} \partial_x \phi_{\mathbf{i}} \\ \partial_y \phi_{\mathbf{i}} \\ \partial_z \phi_{\mathbf{i}} \end{bmatrix} \cdot \begin{bmatrix} u_x(1-\nu) + v_y \nu + w_z \nu \\ \frac{1}{2}(1-2\nu)(u_y + v_x) \\ \frac{1}{2}(1-2\nu)(w_x + u_z) \end{bmatrix} d\Omega, \mathbf{i} = 1, \ldots, 4. \tag{A.25}$$

Where ∂_x denotes the partial differentiation with respect to x, the symbols ∂_y and ∂_z are defined in a similar way. Note that the integral in equation A.25 equals the volume of the tetrahedron, because the vector-matrix product results in a constant value. By using the theorem of Holand-Bell, we see that $\int_{\Omega_e} d\Omega = \frac{|\Delta_e|}{n!}$, where n is the dimension of the problem, and thus we obtain the following formula.

$$E_v \frac{|\Delta_e|}{n!} \sum_{\mathbf{j}=1}^{4} \begin{bmatrix} a_{\mathbf{i}}^1 \\ a_{\mathbf{i}}^2 \\ a_{\mathbf{i}}^3 \end{bmatrix} \cdot \begin{bmatrix} u_{\mathbf{j}} a_{\mathbf{j}}^1 (1-\nu) + v_{\mathbf{j}} a_{\mathbf{j}}^2 \nu + w_{\mathbf{j}} a_{\mathbf{j}}^3 \nu \\ \frac{1}{2}(1-2\nu)(u_{\mathbf{j}} a_{\mathbf{j}}^2 + v_{\mathbf{j}} a_{\mathbf{j}}^1) \\ \frac{1}{2}(1-2\nu)(w_{\mathbf{j}} a_{\mathbf{j}}^1 + u_{\mathbf{j}} a_{\mathbf{j}}^3) \end{bmatrix} d\Omega, \mathbf{i} = 1, \ldots, 4. \tag{A.26}$$

After multiplication, we obtain

$$\begin{aligned} E_v \frac{|\Delta_e|}{n!} \sum_{\mathbf{j}=1}^{4} \Big(a_{\mathbf{i}}^1 a_{\mathbf{j}}^1 (1-\nu) + \frac{1}{2}(1-2\nu)(a_{\mathbf{i}}^2 a_{\mathbf{j}}^2 + a_{\mathbf{i}}^3 a_{\mathbf{j}}^3) \Big) u_{\mathbf{j}} + \ldots \\ \Big(a_{\mathbf{i}}^1 a_{\mathbf{j}}^2 \nu + \frac{1}{2}(1-2\nu) a_{\mathbf{i}}^2 a_{\mathbf{j}}^1 \Big) v_{\mathbf{j}} + \ldots \\ \Big(a_{\mathbf{i}}^1 a_{\mathbf{j}}^3 \nu + \frac{1}{2}(1-2\nu) a_{\mathbf{i}}^3 a_{\mathbf{j}}^1 \Big) w_{\mathbf{j}} \, d\Omega, \mathbf{i} = 1, \ldots, 4. \end{aligned} \tag{A.27}$$

The second integral is the boundary integral

$$B_{\mathbf{ij}}^{be} = K \int_{\partial\Omega_{be}} \phi_{\mathbf{i}} \phi_{\mathbf{j}} \, d\Gamma, \mathbf{i}, \mathbf{j} = 1, \ldots, 3. \tag{A.28}$$

Note that this integral only passes three nodes, since we are on a boundary surface. Or in other words, we are on a plane of a tetrahedron. By using the Holand-Bell theorem, we get the following element matrix

$$B^{be} = K \frac{|\Delta_{be}|}{(n+1)!} \begin{bmatrix} 2 & 1 & 1 \\ 1 & 2 & 1 \\ 1 & 1 & 2 \end{bmatrix} \tag{A.29}$$

The third and last integral is given by

$$F_{x,\mathbf{p}}^e = \int_{\Omega_e} F_x \phi_{\mathbf{p}} \, d\Omega, \mathbf{p} = 1, \ldots, 4 \tag{A.30}$$

Where we have that the force F_x inside the integral equals

$$F_x(\underline{x}, t) = \sum_{k=1}^{2} \sum_{i=1}^{C} \sum_{j=1}^{L} F_k(t) n_x(\underline{x}_j^i) \delta(\underline{x} - \underline{x}_j^i) \Delta\Gamma(\underline{x}_j^i). \tag{A.31}$$

Where $n_x(\underline{x})$ is the x component of the (outward) normal vector at point $\underline{x}$. Further, we have that the Dirac Delta function is defined as

$$\delta(x) = \begin{cases} +\infty, & x = 0 \\ 0, & x \neq 0 \end{cases}, \quad \int_{-\infty}^{\infty} \delta(x) dx = 1. \tag{A.32}$$

Where it has the following property

$$\int_{-\infty}^{\infty} f(t) \delta(t - T) dt = f(T). \tag{A.33}$$

Which is called the sifting property[1]. Due to this, we see that our integral is simplified to

$$F_{x,\mathbf{p}}^e = \int_{\Omega_e} F_x \phi_{\mathbf{p}} \, d\Omega = \sum_{k=1}^{2} F_k(t) \sum_{i=1}^{C} \sum_{j=1}^{L} n_x(\underline{x}_j^i) \Delta\Gamma(\underline{x}_j^i) \phi_{\mathbf{p}}(\underline{x}_j^i), \mathbf{p} = 1, \ldots, 4. \tag{A.34}$$

[1] For more information see WikiDiracDelta

Which gives an element vector of the form

$$\underline{F}_x^e = \sum_{k=1}^{2} F_k(t) \sum_{i=1}^{C} \sum_{j=1}^{L} n_x(\underline{x}_j^i) \Delta\Gamma(\underline{x}_j^i) \begin{bmatrix} \phi_1(\underline{x}_j^i) \\ \phi_2(\underline{x}_j^i) \\ \phi_3(\underline{x}_j^i) \\ \phi_4(\underline{x}_j^i) \end{bmatrix}. \tag{A.35}$$

This element vector will only be non-zero when we can apply the sifting property.
From equation A.27, A.29 and A.35, we then assemble these element matrices and vector into one large system.
In equation A.27 we define the mass matrices U^1, V^1 and W^1 by using the corresponding coefficients that are multiplied by the coefficients used in equation A.21 and A.22. In a similar way we define U^2, V^2, W^2 and U^3, V^3, W^3 for the y and z component version of equation A.12.
Let B denote the assembled mass matrix corresponding to equation A.29, we can then write the weak form of equation A.12 as the following system

$$\begin{bmatrix} U^1 + B & V^1 & W^1 \\ U^2 & V^2 + B & W^2 \\ U^3 & V^3 & W^3 + B \end{bmatrix} \begin{bmatrix} \underline{u} \\ \underline{v} \\ \underline{w} \end{bmatrix} = \begin{bmatrix} \underline{F}_x \\ \underline{F}_y \\ \underline{F}_z \end{bmatrix}. \tag{A.36}$$

Here the vectors $\underline{u}, \underline{v}$ and $\underline{w}$ correspond to the coefficients used in equation A.21 and A.22.

A.3.1. ELLIPTIC PROBLEM

In this section we will show that the mechanical model, given by 4.13 is a strong elliptic system. To see this, we first need to give the definition of a strong elliptic system. For a system given by

$$\frac{\partial}{\partial x^\alpha}(a_{ij}^{\alpha\beta}u_{x^\beta}^j + b_{ij}^\alpha u^j + e_i^\alpha) \tag{A.37}$$

where we make use of the Einstein summation convention and we have that $\alpha,\beta = 1,\dots,\nu$ $i,j = 1,\dots,N$. This system will be *strongly elliptic* if the coefficients satisfy the following constraint

$$|a_{ij}^{\alpha\beta}\lambda_\alpha\lambda_\beta| \neq 0, \forall\lambda_\alpha,\lambda_\beta \neq 0. \tag{A.38}$$

This determinant then contains all the coefficients of the derivatives, on element i,j we have the summation of all the possible second order derivatives of the ith equation and the jth variable.

$$D = \begin{vmatrix} \frac{{\lambda_1}^2(\nu-1)}{\nu-1+2\nu^2} + \frac{1}{2}\frac{{\lambda_2}^2}{1+\nu} + \frac{1}{2}\frac{{\lambda_3}^2}{1+\nu} & \frac{1}{2}\frac{\lambda_2\lambda_1}{1+\nu} - \frac{\lambda_2\nu\lambda_1}{(1+\nu)(2\nu-1)} & -\frac{\lambda_1\nu\lambda_3}{\nu-1+2\nu^2} + \frac{1}{2}\frac{\lambda_3\lambda_1}{1+\nu} \\ -\frac{\lambda_2\nu\lambda_1}{\nu-1+2\nu^2} + \frac{1}{2}\frac{\lambda_2\lambda_1}{1+\nu} & \frac{1}{2}\frac{{\lambda_1}^2}{1+\nu} + \frac{{\lambda_2}^2(\nu-1)}{(1+\nu)(2\nu-1)} + \frac{1}{2}\frac{{\lambda_3}^2}{1+\nu} & \frac{1}{2}\frac{\lambda_3\lambda_2}{1+\nu} - \frac{\lambda_3\nu\lambda_2}{\nu-1+2\nu^2} \\ -\frac{\lambda_1\nu\lambda_3}{\nu-1+2\nu^2} + \frac{1}{2}\frac{\lambda_3\lambda_1}{1+\nu} & -\frac{\lambda_3\nu\lambda_2}{(1+\nu)(2\nu-1)} + \frac{1}{2}\frac{\lambda_3\lambda_2}{1+\nu} & \frac{1}{2}\frac{{\lambda_1}^2}{1+\nu} + \frac{1}{2}\frac{{\lambda_2}^2}{1+\nu} + \frac{{\lambda_3}^2(\nu-1)}{\nu-1+2\nu^2} \end{vmatrix} \tag{A.39}$$

Calculating this determinant gives us

$$D = \frac{1}{4}(\lambda_1^2+\lambda_2^2+\lambda_3^2)^3\frac{\nu-1}{(2\nu-1)(1+\nu)^3}. \tag{A.40}$$

Which is a very elegant formula, considering the matrix where we started with. The first term, containing the squares of the lambda's, can be ignored since we know that this will always be positive. For the second term, there is some freedom considering different values of ν. To see which values are appropriate, we have plotted this function in Figure A.1.

We immediately see that the proper values for ν lie in the interval $(-1,\frac{1}{2})$, which is what we expect considering the denominator of the second term.

Further, since the Poisson ratio is the negative ratio of transverse to axial strain, we also have a physical interpretation of this value. We know that the Poisson ratio of a stable, isotropic, linear elastic material cannot be less than minus one nor greater than a half. Since we assume that the extra cellular matrix will behave in a linear, isotropic manner, we will also have a Poisson ratio that lies in the interval $(-1,\frac{1}{2})$. Hence, from this we can conclude that the determinant given in equation A.40 will be positive, and thus the mechanical model given by 4.13, is a strongly elliptic system.

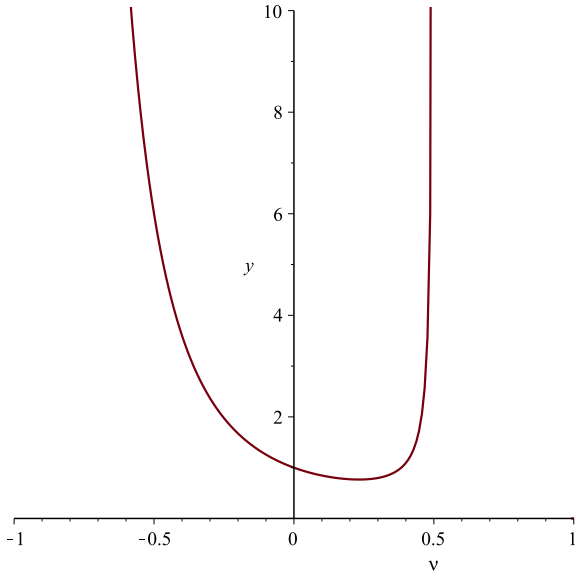

Figure A.1: The determinant in A.40 versus the Poisson ratio.

A.4. DERIVATION OF THE (WEAK) FORMULATION CHEMICAL MODEL

The chemical model is given by the following initial boundary problem

$$\frac{\partial c_k}{\partial t} + \nabla \cdot (\underline{v} c_k) - D_k \Delta c_k = \sum_{i=1}^{C} \sum_{j=1}^{L} \gamma_k(m^i) \delta(\underline{x} - \underline{x}_j^i(t)) = S_k(\underline{x}), \tag{A.41}$$

$$\begin{aligned} c_k(0, \underline{x}) &= 0, \underline{x} \in \Omega, \\ D_k \frac{\partial c_k}{\partial n} + \kappa c_k &= 0, \underline{x} \in \partial\Omega. \end{aligned} \tag{A.42}$$

where $k = 1, \ldots, p$, representing the phenotypes and the summation is done over the cells and their boundary nodes. Further, we have that the advection velocity is given by $\underline{v} = \frac{d\underline{u}}{dt}$, here $\underline{u}$ is the displacement vector obtained from the mechanical problem.

In order to derive the weak form of equation A.41, we multiply by a test function $\phi \in \mathscr{H}^1$ and then integrate over the (time dependent) domain $\Omega(t)$,

$$\int_{\Omega(t)} \frac{\partial c_k}{\partial t} \phi + \nabla \cdot (\underline{v} c_k) \phi - D_k \Delta c_k \phi \, d\Omega = \int_{\Omega(t)} S_k(\underline{x}) \phi \, d\Omega. \tag{A.43}$$

Using Green's Theorem and the boundary condition to reduce the second order derivative to,

$$\int_{\Omega(t)} \frac{\partial c_k}{\partial t} \phi + \nabla \cdot (\underline{v} c_k) \phi + D_k \nabla c_k \cdot \nabla \phi \, d\Omega + \kappa \int_{\partial\Omega(t)} c_k \phi \, d\Gamma = \int_{\Omega(t)} S(\underline{x}) \phi \, d\Omega. \tag{A.44}$$

Expanding the gradient term in front of the velocity field, gives

$$\int_{\Omega(t)} \frac{\partial c_k}{\partial t} \phi + \underline{v} \cdot \nabla c_k \phi + c_k \nabla \cdot \underline{v} \phi + D_k \nabla c_k \cdot \nabla \phi d\Omega + \kappa \int_{\partial\Omega(t)} c_k \phi d\Gamma = \int_{\Omega(t)} S(\underline{x}) \phi \, d\Omega. \tag{A.45}$$

Notice that the first two terms of the integral form a material derivative,

$$\int_{\Omega(t)} \left(\frac{\partial c_k}{\partial t} + \underline{v} \nabla c_k \right) \phi d\Omega = \int_{\Omega(t)} \left(\frac{\partial c_k}{\partial t} + \frac{\partial c_k}{\partial x} \frac{dx}{dt} + \frac{\partial c_k}{\partial y} \frac{dy}{dt} + \frac{\partial c_k}{\partial z} \frac{dz}{dt} \right) \phi d\Omega = \int_{\Omega(t)} \frac{Dc_k}{Dt} \phi d\Omega. \tag{A.46}$$

However, we would like to have the test function also inside the material derivative operator. Hence, by some algebraic operators, we get

$$\frac{Dc_k}{Dt} \phi = \frac{D(c_k \phi)}{Dt} - c_k \frac{D\phi}{Dt} = \frac{D(c_k \phi)}{Dt}. \tag{A.47}$$

The last equality holds by Dziuk and Elliott (2007), which means that the material derivative of the test function equals zero. From the proof of the Reynolds Transport Theorem[2], we have the following property

$$\frac{d}{dt} \left(\int_{\Omega(t)} f(x,t) d\Omega \right) = \int_{\Omega(t)} \left(\frac{Df(x,t)}{Dt} + f(x,t) \nabla \cdot \underline{v}(x,t) \right) d\Omega. \tag{A.48}$$

where $\underline{v}(x,t)$ is the velocity of the domain.
We are going to use this identity to simplify our weak form, which can be done because we have a time dependent domain. Using this identity, we see that

$$\int_{\Omega(t)} \left(\frac{\partial c_k}{\partial t} + \underline{v} \cdot \nabla c_k + c_k \nabla \cdot \underline{v} \right) \phi d\Omega = \int_{\Omega(t)} \frac{D(c_k \phi)}{Dt} + c_k \phi \nabla \cdot \underline{v} d\Omega = \frac{d}{dt} \int_{\Omega(t)} c_k \phi d\Omega. \tag{A.49}$$

If we substitute this result into A.45, we obtain the following formula

$$\frac{d}{dt} \int_{\Omega(t)} c_k \phi d\Omega + D_k \int_{\Omega(t)} \nabla c_k \cdot \nabla \phi d\Omega + \kappa \oint_{\Gamma(t)} c_k \phi d\Gamma = \int_{\Omega(t)} S_k(\underline{x}) \phi \, d\Omega. \tag{A.50}$$

The next step is to approximate the domain integral by the elements $e, e = 1, \ldots, M$, and the boundary integrals by the boundary elements $be, be = 1, \ldots, M_{be}$.

$$\sum_{e=1}^{M} \frac{d}{dt} \int_{\Omega_e(t)} c_k \phi d\Omega + D_k \int_{\Omega_e(t)} \nabla c_k \cdot \nabla \phi d\Omega + \kappa \sum_{be=1}^{M_{be}} \int_{\partial\Omega_{be}(t)} c_k \phi d\Gamma = \sum_{e=1}^{M} \int_{\Omega_e(t)} S_k(\underline{x}) \phi \, d\Omega. \tag{A.51}$$

[2] See wikipedia page ReynoldsTT

We approximate the solution $c_k(\underline{x},t)$ by a linear combination of basis functions

$$c_k(\underline{x},t)=\sum_{j=1}^{N} c_{k,j}(t)\phi_j(\underline{x}),\quad \phi(\underline{x})=\phi_i(\underline{x}), i=1,\dots,N. \tag{A.52}$$

where N is the number of nodes on the grid. By substituting these approximations into equation A.51, we obtain

$$\begin{aligned}\sum_{e=1}^{M}\sum_{j=1}^{N}\frac{d}{dt}\int_{\Omega_e(t)} c_{k,j}(t)\phi_j\phi_i d\Omega + D_k\int_{\Omega_e(t)} c_{k,j}(t)\nabla\phi_j\cdot\nabla\phi_i d\Omega+\dots\\ \sum_{be=1}^{M_{be}}\kappa\int_{\partial\Omega_{be}(t)} c_{k,j}(t)\phi_j\phi_i d\Gamma=\sum_{e=1}^{M}\int_{\Omega_e(t)} S_k(\underline{x})\phi_i\, d\Omega, i=1,\dots,N.\end{aligned} \tag{A.53}$$

Since the basis functions are constructed in a nifty way, we will look at an arbitrary element e and investigate each integral separately. However, in this process we need to be careful with the notation of the grid node we are on, since every basis function is defined on each element differently. Therefore, we denote the nodes of an element e by the bold-face index $\mathbf{i}=1,2,3,4$.
The first integral from equation A.53 is given by

$$A^e_{\mathbf{ij}}=\int_{\Omega_e(t)}\phi_{\mathbf{j}}\phi_{\mathbf{i}}d\Omega,\mathbf{i},\mathbf{j}=1,\dots,4. \tag{A.54}$$

Using Holand-Bell, we obtain the following element matrix

$$A^e(t)=\frac{|\Delta_e|}{(n+2)!}\begin{bmatrix}2&1&1&1\\1&2&1&1\\1&1&2&1\\1&1&1&2\end{bmatrix}, \tag{A.55}$$

where n is the dimension of our problem. We deal with the time derivative of the concentration c_k after the assembly process. From the second integral we can define the following element matrix which represents the discretization of the diffusive part

$$\begin{aligned}D^e_{\mathbf{ij}}(t)=D_k\int_{\Omega_e(t)}\nabla\phi_{\mathbf{j}}\cdot\nabla\phi_{\mathbf{i}}d\Omega=\\ D_k\int_{\Omega_e(t)} a^1_{\mathbf{j}}a^1_{\mathbf{i}}+a^2_{\mathbf{j}}\,a^2_{\mathbf{i}}+a^3_{\mathbf{j}}a^3_{\mathbf{i}}d\Omega=\\ D_k\frac{|\Delta_e|}{n!}a^1_{\mathbf{j}}a^1_{\mathbf{i}}+a^2_{\mathbf{j}}\,a^2_{\mathbf{i}}+a^3_{\mathbf{j}}a^3_{\mathbf{i}},\mathbf{i},\mathbf{j}=1,\dots,4.\end{aligned} \tag{A.56}$$

The third integral of equation A.53 is the boundary integral. Hence, the boundary element matrix is given by

$$B^{be}_{\mathbf{ij}}(t)=\kappa\int_{\partial\Omega_{be}(t)}\phi_{\mathbf{j}}\phi_{\mathbf{i}}d\Gamma,\mathbf{i},\mathbf{j}=1,\dots,3, \tag{A.57}$$

Using Holand-Bell, we obtain the following element matrix

$$B^{be}(t)=\kappa\frac{|\Delta_{be}|}{(n+1)!}\begin{bmatrix}2&1&1\\1&2&1\\1&1&2\end{bmatrix}. \tag{A.58}$$

In the last integral we have to deal with the source function. Since we have the Dirac Delta function inside the source function, we get a similar result as with the mechanical model by using the sifting property of the Dirac Delta function.

$$S^e_{\mathbf{p}}(t)=\int_{\Omega_e(t)} S_k(\underline{x})\phi_{\mathbf{p}}(\underline{x})\, d\Omega,\mathbf{p}=1,\dots,4, \tag{A.59}$$

$$S^e_{\mathbf{p}}(t)=\sum_{i=1}^{C}\sum_{j=1}^{L}\gamma_k(m^i)\phi_{\mathbf{p}}(\underline{x}^i_j),\mathbf{p}=1,\dots,4. \tag{A.60}$$

Which gives the following element vector.

$$\underline{S}^e(t) = \sum_{i=1}^{C}\sum_{j=1}^{L}\gamma_k(m^i)\begin{bmatrix}\phi_1(\underline{x}_j^i)\\ \phi_2(\underline{x}_j^i)\\ \phi_3(\underline{x}_j^i)\\ \phi_4(\underline{x}_j^i)\end{bmatrix}. \tag{A.61}$$

With the gathered information we are able to assemble all the element matrices and vectors into a large matrix and vector. Schematically, the system we obtain is given by

$$A\frac{d}{dt}\underline{c}(t) + D\underline{c}(t) + B\underline{c}(t) = \underline{S}(t). \tag{A.62}$$

Where A is the matrix corresponding to the first integral, D is the matrix from the diffusive part, B is the boundary matrix and $\underline{S}(t)$ is the source vector. To explain how we deal with the time derivative, we rewrite the equation to

$$A\frac{d}{dt}\underline{c}(t) = \underline{S}(t) - (D+B)\underline{c}(t). \tag{A.63}$$

A straightforward way to discretize the time derivative is by using the Euler Forward method. However, in doing so, we limit ourselves in the size of the time step. A more favorable option would be to use the Euler Backward method, which gives us super stability in time.

$$A^{n+1}\underline{c}^{n+1}(t) = A^{n+1}\underline{c}^{n}(t) + \mathrm{d}t\left(\underline{S}^{n+1}(t) - (D^{n+1}+B^{n+1})\underline{c}^{n+1}(t)\right), \tag{A.64}$$

$$\left(A^{n+1} + \Delta t(D^{n+1}+B^{n+1})\right)\underline{c}^{n+1}(t) = A^{n+1}\underline{c}^{n}(t) + \Delta t\underline{S}^{n+1}(t), n = 1,\ldots,T_{max} \tag{A.65}$$

Here n denotes the time step. In the context of the discretization of partial differential equations, we need the mass matrix $\left(A^{n+1} + \Delta t(D^{n+1}+B^{n+1})\right)$ on the left hand side to be an M-matrix. An $n\times n$ matrix A is an M-matrix, if it satisfies the following properties

1. $A_{ii} > 0$ for $i = 1,\ldots,n$;
2. $A_{ij} \leq 0$ for $i \neq j, i, j = 1,\ldots,n$;
3. A is irreducibly diagonally dominant.

This property guarantees the absence of wiggles in convection dominated flows and the positivity of concentrations in chemical engineering applications [33].
However, since we are using the theorem by Holand-Bell to obtain a value for the integral, we are lacking this property in matrix A^{n+1} and B^{n+1}. An easy way to see this is by looking at the element matrices of equation A.55 and A.58. It is clear that these element matrices do not satisfy the criteria of an M-matrix, hence it is unlikely that the assembled matrix will have these properties. The matrix D^{n+1} is already an M-matrix since this matrix represents the discretization of the diffusion.
In order for matrix A^{n+1} and B^{n+1} to be an M-matrix, we need a different approach than Holand-Bell to evaluate the integral. An option to do so is by using Newton-Cotes integration, this result in an element matrix of the form

$$\alpha I_{n\times n} \tag{A.66}$$

where α is some constant depending on the area of the triangle Δ and $I_{n\times n}$ is the identity matrix with dimension n. Then both the matrices A^{n+1} and B^{n+1} will have the shape of an identity matrix, hence they will have the M-property. The result of using Newton-Cotes integration, instead of Holand-Bell, becomes apparent in the precision of our solution, since this approximation introduces an error of order $\mathcal{O}(h^2)$. However, since we use linear basis functions to solve the partial differential equations with the FEM, we already have an error of order $\mathcal{O}(h^2)$, hence using Newton-Cotes will not influences the precision of our solution.

A.5. FOURIER ANALYSIS ON THE MECHANICAL SIGNAL

In this section we explain how we conduct the Fourier Analysis on the mechanical signal to obtain the direction of the mechanical stimulus.
In this setting we choose the time interval to be given by $[(t-\tau)+,t]$, which is equal to the domain of integration in equation 4.33. However, since we do not have an analytical representation of the signal $\boldsymbol{\phi}^i(t)$, we must use the numerical approximation of $\boldsymbol{\phi}^i(t)$ and therefore also use the Discrete Fourier Transform (DFT). When we apply this transformation to the signal $\boldsymbol{\phi}^i(t)$, we get

$$\boldsymbol{\Phi}^i(s) = \mathscr{F}_D[\boldsymbol{\phi}^i(t)]. \tag{A.67}$$

Where we define the DFT, as

$$\boldsymbol{\Phi}^i(s) = \sum_{n=0}^{N-1} \boldsymbol{\phi}^i(t_n) e^{-2\pi i s n/N}, s \in \mathbb{Z}. \tag{A.68}$$

Here $t_n, n = 0,\dots,N-1$ denotes the discretization of the time interval $[(t-\tau)+,t]$, which is discretized by N nodes that depend on the time step size Δt by the following relation $N = \frac{\tau}{\Delta t}$. However, we do realize that the time step is restricted by the period (or frequency) that we impose on the contraction rate of the myocytes, since the DFT produces accurate results when the time interval is an integer multiple of the period.
Keeping this in mind, we obtain the frequency of the signal $\boldsymbol{\phi}^i(t)$ by

$$\hat{s} = \underset{s}{\operatorname{argmax}} \|\boldsymbol{\phi}^i(s)\| \tag{A.69}$$

However, this value $\hat{s}$ will only tell us at which position we will find the frequency in the *frequency domain*. To obtain the frequency we will use the sampling frequency $F_s = \frac{1}{\Delta t}$ and the fact that the frequency in the center of the frequency domain is equal to $\frac{F_s}{2}$, hence

$$\hat{f} = \frac{F_s}{2}\hat{s}\frac{2}{N}, \tag{A.70}$$

which we can simplify to

$$\begin{aligned} \hat{f} &= \frac{F_s \hat{s}}{N}, \\ \hat{\omega} &= 2\pi \hat{f}. \end{aligned} \tag{A.71}$$

A.6. THE GRADIENT RECOVERY METHOD

In this section we explain how we have obtained the gradient of the mechanical strain energy while using first order basis functions. We will first show the essence of the problem, which is that we need to calculate a second derivative, while our basis functions are a first order polynomial. Recall that the mechanical strain energy is defined by

$$M(\underline{x},t) = \frac{1}{2}(\sigma_{11}\varepsilon_{11} + \sigma_{12}\varepsilon_{12} + \sigma_{22}\varepsilon_{22}). \tag{A.72}$$

Substituting the definition for the stress and strain into this equation, we see that we have

$$\begin{aligned} M(\underline{x},t) &= \frac{E_v}{2}\left((u_x(1-\nu)+v_y\nu)u_x + \frac{1}{2}(1-2\nu)(u_y+v_x)\frac{1}{2}(u_y+v_x) + (u_x\nu + v_y(1-\nu))v_y\right) = \\ &\frac{E_v}{2}\left(u_x^2(1-\nu) + u_x v_y \nu + \frac{1}{4}(1-2\nu)(u_y^2+v_x^2+2u_y v_x) + v_y u_x \nu + v_y^2(1-\nu)\right) = \\ &\frac{E_v}{8}\left(4u_x^2(1-\nu) + 8u_x v_y \nu + 4v_y^2(1-\nu) + u_y^2 + v_x^2 + 2u_y v_x - 2\nu u_y^2 - 2\nu v_x^2 - 4\nu u_y v_x\right). \end{aligned} \tag{A.73}$$

If we want to calculate the gradient of equation A.73, we obtain a complex formula where we need to be able to calculate the second order derivative of the displacement $\underline{u}(\underline{x},t)$. However, note that the displacement $\underline{u}(\underline{x},t)$ is approximated by N basis functions.

$$u(\underline{x},t) = \sum_{j=1}^{N} u_j\phi_j(\underline{x}),\ v(\underline{x},t) = \sum_{j=1}^{N} v_j\phi_j(\underline{x}). \tag{A.74}$$

Where the basis functions were explicitly defined on an element as

$$\phi_{\mathbf{j}}(\underline{x}) = a_0^{\mathbf{j}} + a_1^{\mathbf{j}}x + a_2^{\mathbf{j}}y, \mathbf{j} = 1,\ldots,3. \tag{A.75}$$

Hence, per element we are able to calculate the first derivative of the displacement $\underline{u}(\underline{x},t)$. However, calculating the second order derivative is possible, but results in a rather trivial answer which is unsuitable for further calculations.

In order to be able to calculate the gradient of the mechanical strain energy, we calculate the piecewise constant stress and strain field, and then approximate a piecewise linear function to these fields. This method is also known as the ZZ-patch recovery method [34].

To obtain this piecewise linear function we will make use of the already defined (first order) basis functions and try to find a suitable linear combination such that the error between this piecewise linear function and the stress and strain fields is minimal. We denote this approximation of the stress and strain field by

$$\sigma^*(\underline{x}) = \sum_{j=1}^{N} \sigma_j^*\phi_j(\underline{x}), \tag{A.76}$$

$$\varepsilon^*(\underline{x}) = \sum_{j=1}^{N} \varepsilon_j^*\phi_j(\underline{x}). \tag{A.77}$$

The idea here is to apply a least square estimation with these approximations to the existing values of the stress and strain on a patch, such a patch is given in Figure A.2 and constitutes of the union of the adjacent elements to a node.

By using this approximation on a patch, we can then determine (approximated) nodal values for the stress and strain fields, which are denoted by $\sigma_j^*, \varepsilon_j^*$ as seen in equation A.4, A.77. In turn, this enables us to calculate the derivative of the stress and strain fields that are needed to calculate the gradient of the mechanical strain energy. To demonstrate this technique, we will now show an example to calculate one component of the stress field.

To calculate the least square estimation on a patch we will first define a polynomial, in vector format, that is of the same order as our basis functions

$$\underline{P}(\underline{x}) = [1\ x\ y], \tag{A.78}$$

Further, we define the following patch coefficients, in vector format, that will enable us to eventually calculate the nodal coefficients σ_j^*

$$\underline{\boldsymbol{\sigma}}_j^* = [\boldsymbol{\sigma}_1^*\ \boldsymbol{\sigma}_2^*\ \boldsymbol{\sigma}_3^*]^T. \tag{A.79}$$

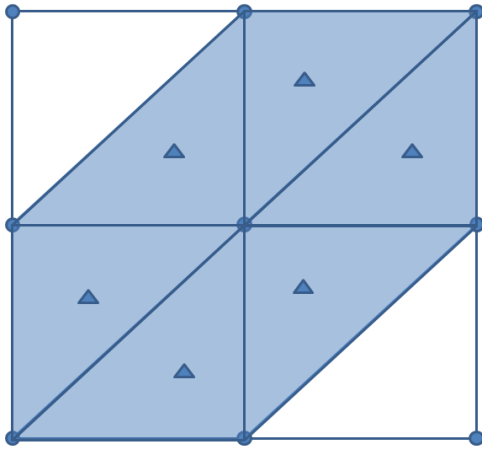

Figure A.2: The geometrical entities associated with a cell, where the sampling nodes are denoted by the small solid triangles

Then we take the values of the strain field σ^h, that we have obtained from the FEM, in the N_P sampling nodes given in Figure A.2, and use these values for the least square estimation. This results in minimizing the following function

$$F(\underline{\boldsymbol{\sigma}}_j^*) = \sum_{p=1}^{N_P} (\sigma^h(x_p, y_p) - \underline{P}(x_p, y_p) \cdot \underline{\boldsymbol{\sigma}}_j^*)^2 \tag{A.80}$$

If we want to minimize $F(\underline{\boldsymbol{\sigma}}_j^*)$, we need to calculate $F'(\underline{\boldsymbol{\sigma}}_j^*) = 0$, hence

$$\begin{aligned} F'(\underline{\boldsymbol{\sigma}}_j^*) &= 0 \\ -2 \sum_{p=1}^{N_P} \underline{P}(x_p, y_p)^T (\sigma^h(x_p, y_p) - \underline{P}(x_p, y_p) \underline{\boldsymbol{\sigma}}_j^*) &= 0 \\ \sum_{p=1}^{N_P} \underline{P}(x_p, y_p)^T (\sigma^h(x_p, y_p) - \underline{P}(x_p, y_p) \underline{\boldsymbol{\sigma}}_j^*) &= 0 \\ \sum_{p=1}^{N_P} \underline{P}(x_p, y_p)^T \underline{P}(x_p, y_p) \underline{\boldsymbol{\sigma}}_j^* &= \sum_{p=1}^{N_P} \underline{P}(x_p, y_p)^T \sigma^h(x_p, y_p) \end{aligned} \tag{A.81}$$

Hence, if we want to solve this equation, we first define

$$\begin{aligned} A_p &= \sum_{p=1}^{N_P} \underline{P}(x_p, y_p)^T \underline{P}(x_p, y_p) \\ b_p &= \sum_{p=1}^{N_P} \underline{P}(x_p, y_p)^T \underline{\boldsymbol{\sigma}}_j^* \end{aligned} \tag{A.82}$$

and then state

$$\underline{\boldsymbol{\sigma}}_j^* = A_p^{-1} b_p \tag{A.83}$$

By using these coefficients, we then define the nodal value of the stress field as

$$\sigma_j^* = \underline{P}(\underline{x}_j) \underline{\boldsymbol{\sigma}}_j^*, j = 1, \ldots, N \tag{A.84}$$

To see the effect of this method on the first component of the stress field, we present the following two figures.

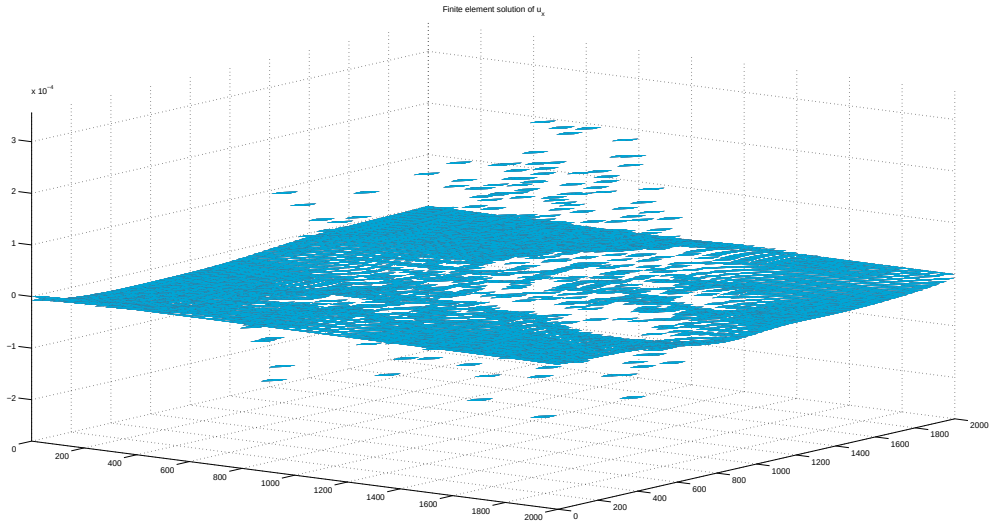

Figure A.3: Derivative of the displacement with respect to the x direction by using the FEM solution

Figure A.3 shows the piecewise constant derivative of the displacement in the x direction. By applying the ZZ-patch gradient recovery method on this result, we obtain the graph seen in Figure A.4.

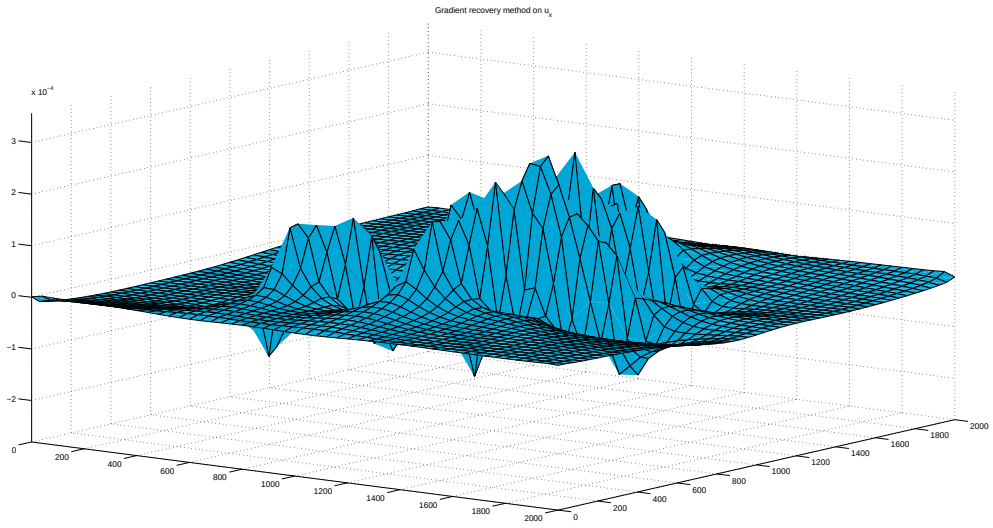

Figure A.4: ZZ-patch gradient recovery solution of the derivative of the displacement with respect to the x direction

Note however that this is just an approximation. By closer inspection, one can see that the method has difficulty in mimicking the extreme values of the derivative from Figure A.3. Though, the reconstruction of the gradient has improved compared to cases where this gradient recovery method has not been applied.

A.7. GENERALIZED NOVEL MODEL APPROACH FOR ARBITRARY PHENOTYPES

In this section we explain how to expand the current model to simulate the differentiation behavior towards p phenotypes, instead of two.

First of all, the model for two phenotypes has been constructed such that extending it an arbitrary number of phenotypes is a straightforward task. The main problem lies in defining new variables for the other phenotypes.

For example, to add one phenotype we need to determine what its shape will be, the secretion rate of its cytokine and the way it applies force on the domain and how it reacts to forces and to its chemical environment. Having defined these quantities, we are left with one challenge, and that is the definition of the mechanical stimuli $\psi^i_M(t)$ and the direction of the mechanical stimuli $\iota^i_M(t)$. Since at this moment, the definition of the mechanical stimuli is specifically designed for myocyte behavior. The same holds for the definition of the direction of the mechanical stimuli. When we introduce a new phenotype, for example bone cells, we need to reconsider these definitions and adapt them where necessary.

However, to make an appropriate adaptation, we first need to obtain more knowledge about the phenotype we want to add. Like its behavior during differentiation, interaction with other cells and change in size during its genesis. Hence, little can be said about how to add another phenotype, however we have constructed the model cleverly such that this addition takes little effort.

A.8. EXTENSION TOWARD THREE DIMENSIONS

In this section we will explain how the 2D model can be extended towards three dimensions. Since the reader should be quite familiar with the 2D model by now, we will mostly state the new equations which will be accompanied with some small notes.
We start by explaining how a 3D cell is defined, and all its geometrical aspects. Then we will make a small note about the force function of the cells, followed by the changes in the equation for cell movement. At last we make a short comment on the change of the domain Ω.

A.8.1. GEOMETRICAL ADAPTATIONS

In 2D we already defined the length and width of a cell, for the 3D model we also need a definition for the height, which is given by

$$H_k^i(t) = H_k^0 + (H_{\infty,k} - H_k^{i,0})m^i(t). \tag{A.85}$$

By using the length, width and height, we define the cell boundary nodes by the following parametric formula

$$\begin{aligned} x_{j,J}^i(t) &= L_k^i(t)\cos(J\frac{2\pi}{L} - \pi)\cos(j\frac{2\pi}{L}), \\ y_{j,J}^i(t) &= W_k^i(t)\cos(J\frac{2\pi}{L} - \pi)\sin(j\frac{2\pi}{L}), \\ z_{j,J}^i(t) &= H_k^i(t)\sin(J\frac{2\pi}{L} - \pi),\ j,J = 1,\dots,L. \end{aligned} \tag{A.86}$$

From this parametric formulation, we can easily determine the outward normal vector on the surface of an ellipsoid.

$$\underline{n}_{j,J}^i(t) = \left[\frac{x_{j,J}^i}{(L_k^i(t))^2},\ \frac{y_{j,J}^i}{(W_k^i(t))^2},\ \frac{z_{j,J}^i}{(H_k^i(t))^2}\right]^T \quad j,J = 1,\dots,L. \tag{A.87}$$

In order to perform the rotation to the cells, we need to define three rotation matrices. One rotation matrix for each axis, where each rotation matrix rotates a vector around its axis in an anti-clockwise manner. The definition of these rotation matrices are given by equation A.88.

$$\begin{aligned} R_x(\theta) &= \begin{bmatrix} 1 & 0 & 0 \\ 0 & \cos\theta & -\sin\theta \\ 0 & \sin\theta & \cos\theta \end{bmatrix}, \\ R_y(\theta) &= \begin{bmatrix} \cos\theta & 0 & \sin\theta \\ 0 & 1 & 0 \\ -\sin\theta & 0 & \cos\theta \end{bmatrix}, \\ R_z(\theta) &= \begin{bmatrix} \cos\theta & -\sin\theta & 0 \\ \sin\theta & \cos\theta & 0 \\ 0 & 0 & 1 \end{bmatrix}. \end{aligned} \tag{A.88}$$

The rotation for a certain cell boundary point $\underline{x}_{j,J}^i(t) = [x_{j,J}^i(t),\ y_{j,J}^i(t),\ z_{j,J}^i(t)]^T$, is then determined by three angles, θ_x, θ_y and θ_z. The details on how these angle change over time will be explained later on.
In the 2D model we used the variable $\Delta\Gamma_j^i$ to define the source and force function. This variable denoted the intermediate length between adjacent cell boundary nodes, the 3D version of this is denoted by $\Delta S_{j,J}^i$. However, in the 3D simulation results that are present in this thesis, we have approximated this quantity by dividing the surface area of the cells by the L^2 boundary points. This creates an uniform distribution for the cell surface elements $\Delta S_{j,J}^i(t)$. This is not an ideal method to achieve this quantity, hence for future references we would like to see this be improved.
To obtain the surface are of an ellipsoid is no straightforward task, since there is no analytical formulas for this. One, of the many, approximations is given by Thomsen's formula,

$$S^i(t) = 4\pi\left(\frac{(L_k^i W_k^i)^p + (L_k^i H_k^i)^p + (H_k^i W_k^i)^p}{3}\right)^{1/p}, i = 1,\dots,C, \tag{A.89}$$

where we use $p \approx 1.6075$.

A.8.2. CELL FORCE

Due to the change in the definition of the intermediate length, we also have to adjust the definition of the growing force, given by equation 4.26. Recall that in the 2D case, we added a virtual height to the equation in order to satisfy the dimensions. In the 3D case, we no longer need this virtual height since we already satisfy the dimensions by using the following definition of the growing force

$$F^i_{j,J,G}(t) = \frac{E^i \Delta S^i_{j,J}(t)}{L^i_k(t)} \frac{\mathrm{d}}{\mathrm{d}t} L^i_k(t), j, J = 1, \ldots, L. \tag{A.90}$$

Besides this change in the force vector, we also extend the definition of the octahedral shear strain towards three dimensions. This quantity is then defined by

$$\phi(\underline{x}) = \frac{2}{3}\sqrt{(\varepsilon_1 - \varepsilon_2)^2 + (\varepsilon_2 - \varepsilon_3)^2 + (\varepsilon_1 - \varepsilon_3)^2}. \tag{A.91}$$

Further, the calculations that are accompanied with the octahedral shear strain remain the same.

A.8.3. CELL MOVEMENT

The movement of a cell is influenced by three factors: randomness, the chemical gradient and the mechanical gradient. Extending the first two factors towards three dimensions is a straightforward task. However, to extend the mechanical gradient, we need to present a new definition, since the mechanical strain energy in three dimensions is given by

$$M(\underline{x}, t) = \frac{1}{2}\left(\sigma_{11}\varepsilon_{11} + \sigma_{12}\varepsilon_{12} + \sigma_{22}\varepsilon_{22} + \sigma_{33}\varepsilon_{33} + \sigma_{13}\varepsilon_{13} + \sigma_{23}\varepsilon_{23}\right). \tag{A.92}$$

However, any further calculations remain unchanged.
We continue with the change in orientation of the cells, since this requires some more adaptations. We have already introduced the three rotations matrices $R_x(\theta), R_y(\theta), R_z(\theta)$, but in this section we will show how the rotation angles $\theta^i_x(t), \theta^i_y(t), \theta^i_z(t)$ will change over time. An important note here is that we reduce the 3D problem to three 2D versions, which are simpler because we already have an approach to deal with that situation. A key ingredient here is that we are able to project a 3D vector on three surfaces, as shown in Figure A.5.

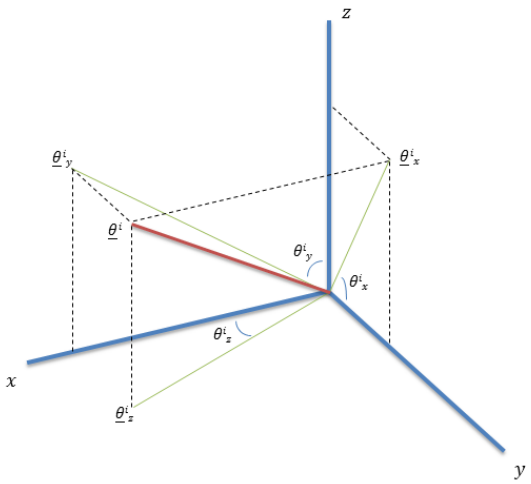

Figure A.5: Graphical representation of the projection of a vector on three different surfaces.

This method of decomposition can be applied to both the current orientation vector $\underline{\theta}^i(t)$ and the direction of movement vector $\underline{v}^i_k(t)$. Subsequently, we calculate the angles between these two vectors on all the three surfaces by using the same method as proposed in Section 4.3.1. Let $\underline{v}^i_k(t)$ denote the vector of change in

position for every cell boundary node in 3D, and let $\underline{\theta}^i(t)$ be the vector form of the current orientation of the cell. Then we denote the projection of the displacement vector on the $y-z$-plane by $\underline{v}^i_{x,k}(t)$, the projection on the $x-z$-plane is given by $\underline{v}^i_{y,k}(t)$ and the projection on the $x-y$-plane is $\underline{v}^i_{z,k}(t)$. In a similar manner we define the projections of $\underline{\theta}^i(t)$ on the three different planes.
The equation of change for the three angles is then given by the compact formulation

$$\begin{aligned} \frac{d}{dt}\theta^i_\alpha(t) &= \theta^{i,0}_\alpha(t)\cos^{-1}\left(\frac{\underline{v}^i_{\alpha,k}(t)\cdot\underline{\theta}^i_\alpha(t)}{\|\underline{v}^i_{\alpha,k}\|\|\underline{\theta}^i_\alpha\|}\right), i=1,\dots,C, k=1,2, \\ \theta^i_\alpha(0) &= 2\pi U(0,1), i=1,\dots,C, \end{aligned} \tag{A.93}$$

where $\alpha=\{x,y,z\}$, and to define $\theta^{i,0}_\alpha(t)$ we first define the following vectors

$$\underline{\hat{v}}^i_{\alpha,k}(t) = R_{cw}(\theta^i_\alpha(t))\underline{v}^i_{\alpha,k}(t). \tag{A.94}$$

Where $R_{cw}(\theta)$ is the clock-wise rotation matrix. With this new defined vector, we have that

$$\begin{aligned} \theta^{i,0}_x(t) &= \text{sgn}(\underline{\hat{v}}^i_{x,k}(t)\cdot\underline{e}_z), \\ \theta_y i,0(t) &= \text{sgn}(\underline{\hat{v}}^i_{y,k}(t)\cdot\underline{e}_z), \\ \theta^{i,0}_z(t) &= \text{sgn}(\underline{\hat{v}}^i_{z,k}(t)\cdot\underline{e}_y). \end{aligned} \tag{A.95}$$

Note that we have not implemented this rotation method into the 3D model. Thus the idea proposed here is only a theoretical approach for which we assume will work in practical applications as well. If this were to be implemented in the current model, we advice to write a small test script first to get a feeling for the rotations and to be sure that every rotation is done in a correct way.

A.8.4. DOMAIN CHANGES

The transform the 2D domain to a 3D one is straightforward, since all the calculations to find the weak form have already been executed in 3D, see Appendix A.3 and A.4. However, from a computational point of view there has been made some changes due to the use of a different kind of grid and node numbering, but this remark only concerns the one that works with the source code.
Further, the domain remained a cube, which is denoted by Ω, and the boundary $\partial\Omega$ is now defined by the six faces that make up the cube.

A.9. VALIDATION OF MODELS

A model is useless without validating the basics one is working with. In this thesis the basics are the time-dependent reaction diffusion equation, and the momentum equation.
In order to be sure that the answers we obtain are what we expect, we have constructed a validation technique. The trick is to propose a solution, i.e. a known concentration or displacement which satisfies the boundary conditions, and then solve for the appropriate source or force vector.
The obtained source and force vector are then implemented in the Finite Element Method, which gives our numerical answer. What we expect to see is that this numerical answer equals the proposed solution from which we started as time and spatial resolution increase.
This validation technique has been applied to the time dependent advection diffusion equation of the chemical mode, and the momentum equation of the mechanical model.

A.9.1. CHEMICAL MODEL

The chemical model is driven by the following set of equations

$$\begin{aligned} \frac{\partial c_k}{\partial t} - D_k \Delta c_k &= S(\underline{x}), \quad \underline{x} \in \Omega, \\ c_k(\underline{x}, 0) &= 0, \quad \underline{x} \in \Omega, \\ D_k \frac{\partial c_k}{\partial n} + \kappa c_k &= 0, \quad \underline{x} \in \partial\Omega. \end{aligned} \tag{A.96}$$

Here we have that c_k is the chemical concentration, D_k is the diffusion coefficient, $S(\underline{x})$ is the sourcing vector and κ is the rate of outsourcing at the boundary.
We now wish to find a sourcing vector that corresponds with the steady state solution

$$c(x, y, t) = x(l_0 - x)y(l_0 - y), \tag{A.97}$$

where l_0 is the length and width of the domain Ω. By setting $\kappa \gg 1$, equation A.97 will satisfy the boundary conditions. When equation *A.97* is substituted into equation A.96, we obtain the following sourcing function

$$S(x, y) = -2D_k(-l_0 y + y^2 - x l_0 + x^2). \tag{A.98}$$

In the left graph of Figure A.6 one can see a plot of the analytic solution proposed in equation *A.97*, where in the right graph of Figure A.6 we present the numerical approximation.

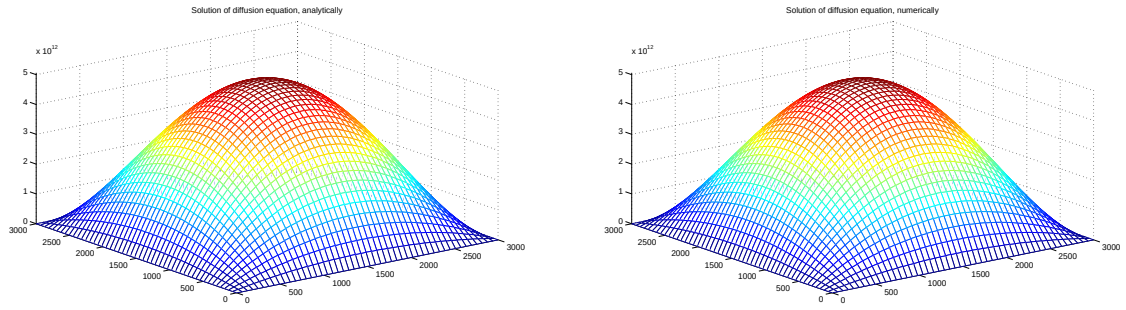

Figure A.6: Comparisson between analytic (left) and numerical (right) solution

In order to produce these results we have used the following parameters

Table A.1: Parameters used to calculate the numerical solution

Parameter	Value
D_k	135
M	50
l_0	2000
κ	$1 \cdot 10^{15}$
Δt	$1 \cdot 10^{8}$
T	2

By inspection one can already see the similarities, however inspection is not enough to see that the numerical approximation is a reasonable one. Therefore, in Figure A.7 one can see the relative absolute difference between the numerical and analytical solution.
This error is calculate by

$$\frac{|\tilde{c}(\underline{x}, t) - c(\underline{x}, t)|}{c(\underline{x}, t)}. \tag{A.99}$$

Where $\tilde{c}(\underline{x}, t)$ is the numerical solution and $c(\underline{x}, t)$ the analytical solution given by equation A.97.
From Figure A.7 we see that the error is of order 10^{-10} under the conditions posed in Table A.1
If we would take κ even larger, then we obtain a warning from Matlab saying that the mass matrix is close to singular. The large time step is taken such that we have to calculate fewer time steps.

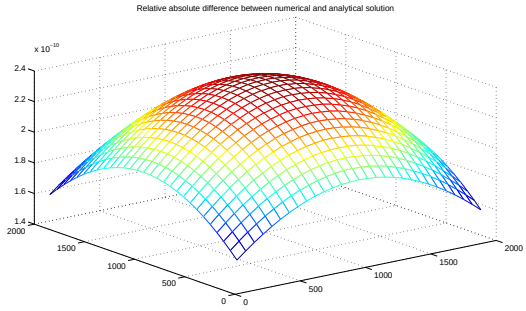

Figure A.7: Relative difference between the analytic and numerical solution

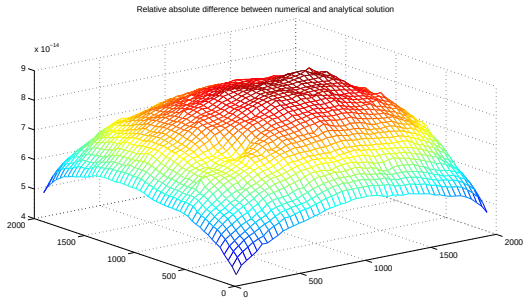

Figure A.8: Relative difference between the analytic and numerical solution

However, if we do take Δt larger, then something remarkable happens to the absolute difference. This phenomena is given in Figure A.8. We believe this behavior is caused by numerical errors. For this particular case we have used the same parameters, except set the time step $\Delta t = 1 \cdot 10^{15}$.

A.9.2. MECHANICAL MODEL

The mechanical model is driven by the equations

$$\begin{aligned} \nabla \cdot \underline{\underline{\sigma}} + \underline{F}_1 + \underline{F}_2 = 0, \quad \underline{x} \in \Omega, \\ \underline{\underline{\sigma}} \cdot \underline{n} + K\underline{u} = 0, \quad \underline{x} \in \partial\Omega. \end{aligned} \tag{A.100}$$

The proposed solution for this model is identical to that of the chemical model

$$\begin{aligned} u(x,y) = x(l_0 - x)y(l_0 - y) \\ v(x,y) = x(l_0 - x)y(l_0 - y) \end{aligned} \tag{A.101}$$

Hence, also in this situation we need that $K \gg 1$.
By substituting this solution into equation A.100, we get a force vector with the following x and y components

$$\begin{aligned} F_x(x,y) = -\frac{1}{2}E_\nu(4l_0\nu x + 4l_0\nu y - 4\nu x^2 - 4\nu y^2 + l_0^2 - 4l_0 x - 6l_0 y + 2x^2 + 4xy + 4y^2), \\ F_y(x,y) = -\frac{1}{2}E_\nu(4l_0\nu x + 4l_0\nu y - 4\nu x^2 - 4\nu y^2 + l_0^2 - 6l_0 x - 4l_0 y + 4x^2 + 4xy + 2y^2). \end{aligned} \tag{A.102}$$

Here l_0 is the length and width of the domain, ν is Poisson's ratio and E_ν is given by

$$E_\nu = \frac{E}{(1+\nu)(1-2\nu)}. \tag{A.103}$$

Implementing this in the FEM gives a vector plot of the numerically calculated displacement. In Figure A.9 we compare the analytical results with the numerical solution.

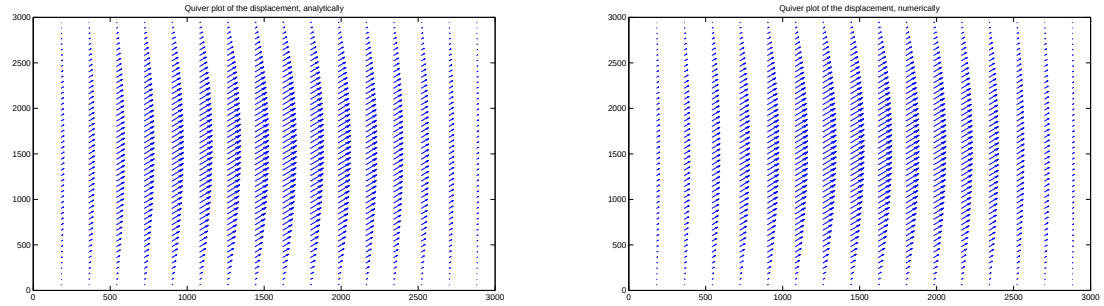

Figure A.9: Comparisson between analytic(left) and numerical(right) solution

From this quiver plot, we see by inspection that the numerical solution produces correct results. To see how precise our approximation is, we will analyze the displacement in the x-direction on $l_0/2$.
Since we have a strong elliptic problem, we have no need to also investigate the y-direction, since the problem is symmetric by definition of ellipticity.
In Figure A.10 the absolute relative difference between the numerical $\tilde{u}(\underline{x},t)$ and analytical solution $u(\underline{x},t)$ on the line $y = l_0/2$ is given. Hereby we mean that the graphs presented here are calculated by

$$\varepsilon_e = \frac{|\tilde{u}(\underline{x},t) - u(\underline{x},t)|}{u(\underline{x},t)} \tag{A.104}$$

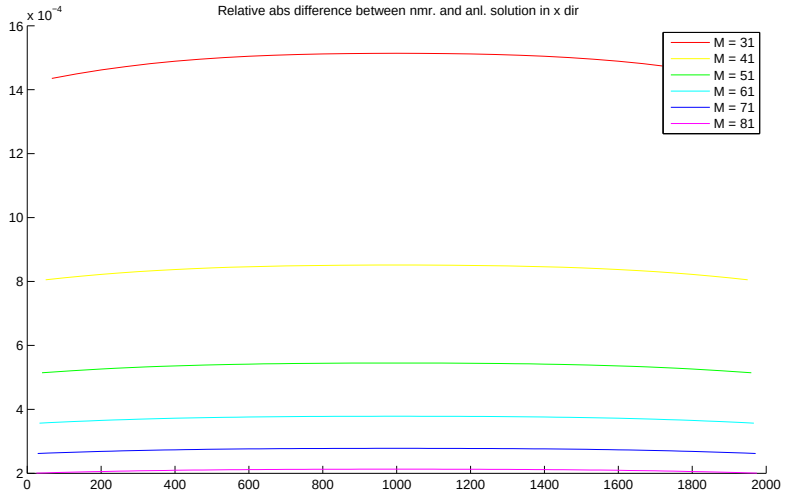

Figure A.10: Relative difference between analytic and numerical solution for different grid sizes M

However, from Figure A.10 we see that the relative difference is only of order 10^{-4} when $M = 31$, while for the validation of the chemical model we obtained a relative error of order 10^{-10}. Hence, we would like to know which value for M would produce a relative error of order 10^{-10} and if this is possible.
By taking the mean value of the relative error in equation A.104 we can assign one value that represents this error for each grid size, when we then increase the grid size M we expect that the relative error should decrease. This behavior can be seen in Figure A.11, we have taken the log scale of the absolute relative error and grid size M, since then we can easily observe of which order the error is in terms of M.

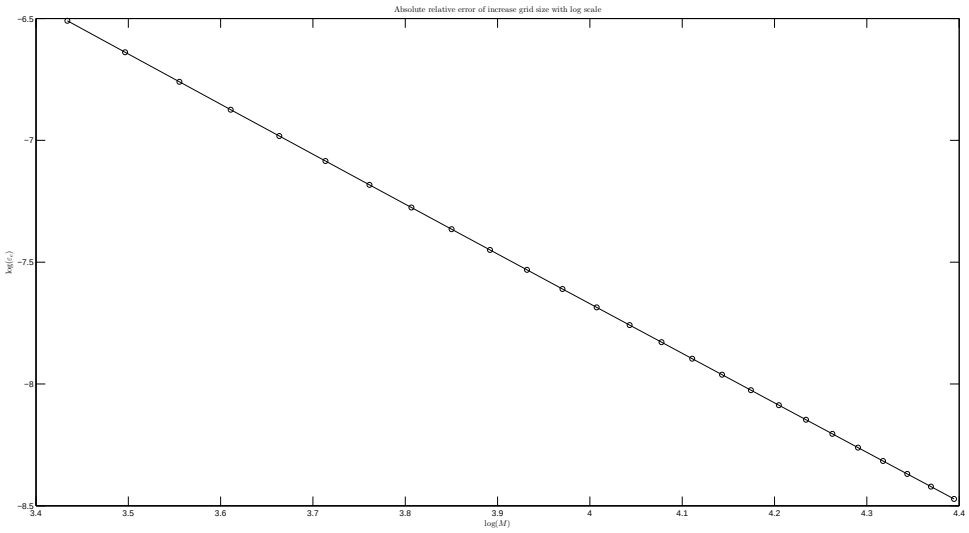

Figure A.11: Plot of equation A.104 with increasing grid size M using log scaled axis.

By inspection we see that the slope of the graph presented in Figure A.11 is ≈ -2. Since $M \sim \frac{1}{h}$, we can now say that the absolute relative error is of order $\mathcal{O}(h^2)$ which is what we expect when we are using the FEM with linear basis functions. However, this means that around $M \approx 1000$ we would obtain an absolute relative error of 10^{-10}.

A.10. COMPARING DIFFERENT SOURCE TECHNIQUES

In section 4.2.1 we described that cells secrete their cytokine into the domain via their cell boundary nodes, which act as source nodes for the domain. However, it is also *possible* to let cells secrete their cytokine from their cell center.
The difference between these two approaches could decide which approach is more favorable. But before we continue, we explain how for a general case the sourcing vector is created from the cell boundary nodes.
Figure A.12 shows a cell on the domain Ω, where the grid is represented by the triangular pattern and the ellipse-shape represents the cell on the domain. As explained before, we have approximated the domain by N points, and the cell boundary by L points. Due to this, we have that every cell boundary node will lie in a certain triangle.
This relation between the grid nodes and the cell boundary nodes is used to construct the sourcing vectors. A graphical representation of this relation is also given in Figure A.13.

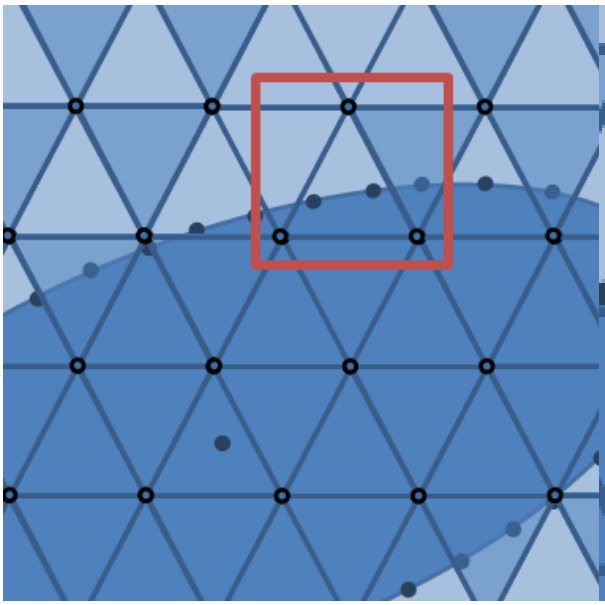

Figure A.12: Abstract display of cell and grid

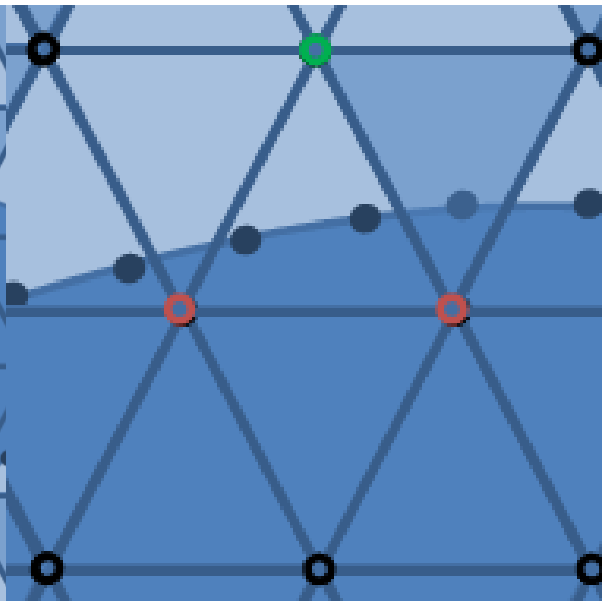

Figure A.13: Abstract display of cell and grid

To quantify the difference between the two sourcing techniques, we will solve the chemical model for one cell with either L boundary nodes, or none. Which results in the definition of two distinct sourcing functions.
The sourcing function that corresponds to the situation where we use L cell boundary-nodes, is given by equation A.105

$$\underline{\tilde{S}}(\underline{x}) = \sum_{j=1}^{L} \gamma^0 m^1(t)\delta(\underline{x} - \underline{x}_j^1)\Delta\Gamma_j^1, \tag{A.105}$$

where $m^i(t)$ is fixed, since we do not model the differentiation process in this case, and $\Delta\Gamma_j^1$ is the intermediate length between two successive cell boundary-nodes.
The sourcing function that corresponds to the situation where we source from the cell center-node, is given by equation A.106

$$\underline{\hat{S}}(\underline{x}) = \gamma^0 m^1(t)\delta(\underline{x} - \underline{x}^1)P^i(t), \tag{A.106}$$

where the last factor represents the approximation of the perimeter by Ramanujan of an ellipse, which is given by

$$\begin{aligned} h &= \frac{(L^i(t) - W^i(t))^2}{(L^i(t) + W^i(t))^2} \\ P^i(t) &= \pi(L^i(t) + W^i(t))\left(1 + \frac{3h}{10 + \sqrt{4 - 3h}}\right) \end{aligned} \tag{A.107}$$

and is of order $\mathcal{O}(h^5)$ [35].

In order to compare the two cases, we need to obey a certain mass balance between the two sourcing functions. Hence we want that

$$\begin{aligned}
\int_\Omega \underline{\hat{S}}(\underline{x})d\Omega &= \int_\Omega \underline{\tilde{S}}(\underline{x})d\Omega, \\
\int_\Omega \gamma^0 m^1(t)\delta(\underline{x}-\underline{x}_j^1)P^i(t)d\Omega &= \int_\Omega \sum_{j=1}^{L} \gamma^0 m^1(t)\delta(\underline{x}-\underline{x}_j^1)\Delta\Gamma_j^1 d\Omega, \\
\gamma^0 m^1(t)P^i(t) &= \sum_{j=1}^{L} \gamma^0 m^1(t)\Delta\Gamma_j^1, \\
P^i(t) &= \sum_{j=1}^{L} \Delta\Gamma_j^1,
\end{aligned} \tag{A.108}$$

where we have used the sifting property to simplify the domain integrals.
Hence, before we run the simulation, we need to be sure that we satisfy the constrain given in equation A.108. Since the order of the approximation depends on h, given in equation A.107, we will analyze a worst case scenario in which we a have a skew ellipse and then find a value for L which is sufficient for the approximation of the boundary of this ellipse.
The worst case scenario can be found by modeling a full grown myocyte, which has the poorest length-width ratio. In Figure A.14 we see the absolute error for different cell boundary-nodes, where we made a distinction between even and odd numbered cell boundary-nodes.

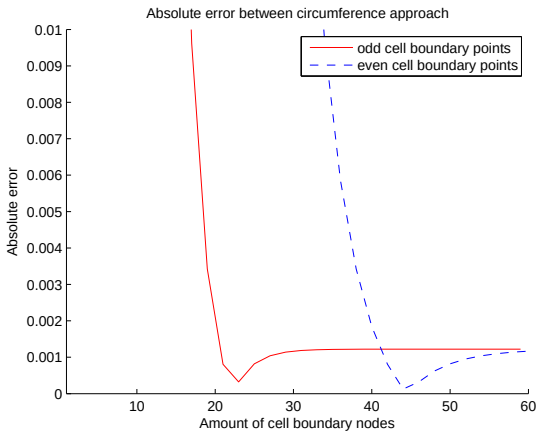

Figure A.14: Absolute difference between the circumference approach

From this analysis we see that $L = 44$ gives the smallest error and $L = 23$ the second smallest error. Continuing with this parameter, we analyze the difference in sourcing of both sourcing approaches.

In Figure A.15 we display the cell center-sourcing technique. Notice the big red dot around the cell center.

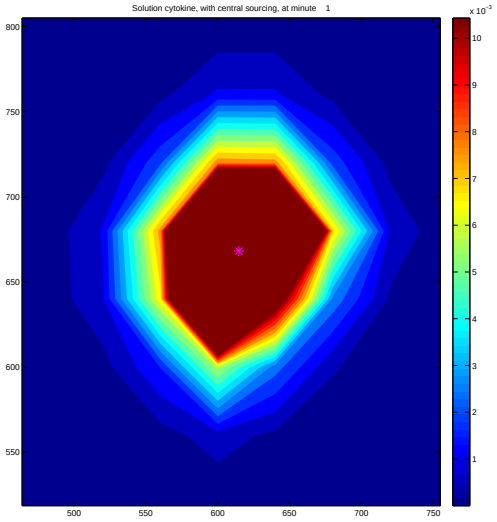

Figure A.15: Sourcing from cell center

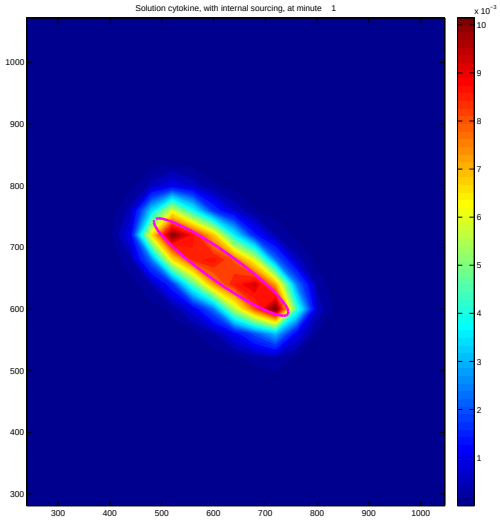

Figure A.16: Sourcing from cell boundary

Inspecting both figures, we see a clear distinction between the two approaches. This comes from two factors, the first is the short time of simulation and the second comes from the assumption that muscle cells are best modeled as ellipse-shaped cells. However, it is possible that this assumption is wrong and that a more plausible way of modeling muscle cells is by using many circle-shaped cells. Therefore we also investigate the case where we use circle-shaped cells, the result of this can be found in Figure A.17 and A.18

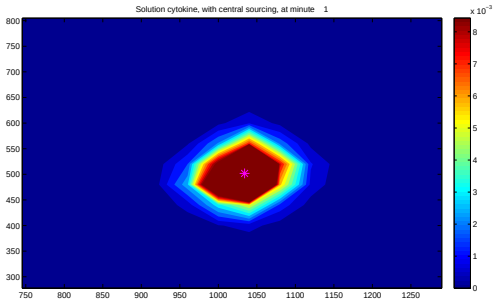

Figure A.17: Sourcing from cell center

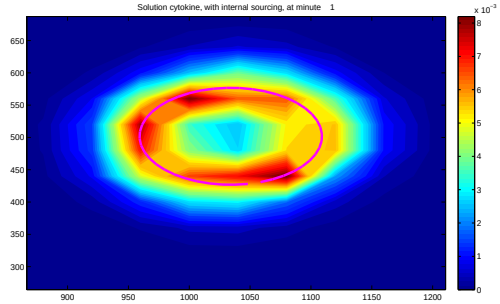

Figure A.18: Sourcing from cell boundary

This result would bring us again in the position that cell-center sourcing seems to be avoided, because of the large difference in the characteristic of the contour plot. However, note that these results display the chemical concentration after one time step. Therefore we also plot the chemical concentration over a longer period of time, these are shown in Figure A.19 and A.20.

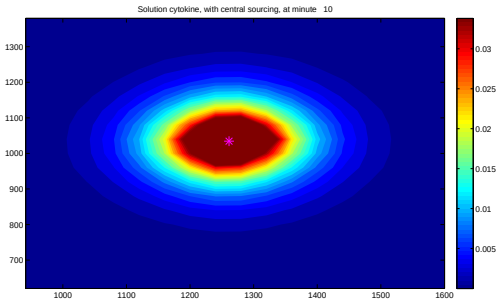

Figure A.19: Sourcing from cell center

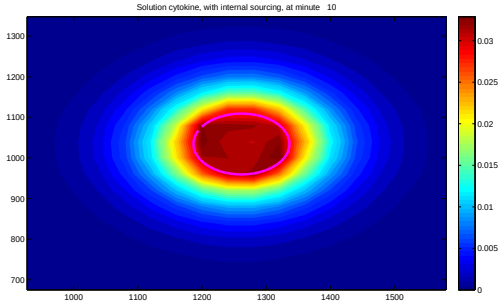

Figure A.20: Sourcing from cell boundary

This shows that eventually the two solutions will obtain the same characteristics over time, and eventually be equal in the sense of the equilibrium state, which is what we expect since we conserve mass. However, this does not give rise to the conclusion that, when we simulate only circular shaped cells, the central secretion method is more favorable than the cell boundary secretion method. This is because we are simulating a dynamic system that is sensitive to small amounts of chemical concentration and has no desire to obtain an overall equilibrium state, rather we would expect some sort of dynamic equilibrium state in the cell population due to the constant change of the cell population.

BIBLIOGRAPHY

[1] G. M. Ellison, *Adult c-kitpos cardiac stem cells are necessary and sufficient for functional cardiac regeneration and repair,* Cell **154** (2013).

[2] E. Martin-Rendon, *5-azacytidine-treated human mesenchymal stem/progenitor cells derived from umbilical cord, cord blood and bone marrow do not generate cardiomyocytes in vitro at high frequencies,* Vax Sanguinis **95** (2008).

[3] D. Baksh, L. Song, and R. Tuan, *Adult mesenchymal stem cells: characterization, differentiation, and application in cell and gene therapy,* Journal of Cellular and Molecular medicine **8** (2004).

[4] P. A. Prokharau, F. J. Vermolen, and J. M. Garcia-Aznar, *A mathematical model for cell differentiation, as an evolutionary and regulated process,* Computer Methods in Biomechanics and Biomedical Engineering **17** (2012).

[5] W. M. Boon, *Incorporation of contracture formation during dermal wound healing: a mathematical model,* (2014).

[6] G. Cooper and R. Hausman, The cell, a molecular approach (ASM press, 2007).

[7] T. Evans, E. T. Rosenthal, J. Youngblom, D. Distel, and T. Hunt, *Cyclin: A protein specified by maternal mrna in sea urchin eggs that is destroyed at each cleavage division,* Cell **33** (1983).

[8] S. van Nieuwenhuijze and A. van Lopik, *Time between onset of apoptosis and release of nucleosomes from apoptotic cells: putative implications for systemic lupus erythematosus.* Ann Rheum Dis. **62** (2003).

[9] S. Even-Ram, *Matrix control of stem cell fate,* Cell **126** (2006).

[10] A. I. Caplan, *Mesenchymal stem cells,* Journal of Orthopaedic Research **9** (1991).

[11] Z. Zhao and et. al., *Directed migration of human bone marrow mesenchymal stem cell in a physiological direct current electric field,* European Cells and Materials **22** (2011).

[12] A. Bertolo and et. al., *In vitro cell motility as a potential mesenchymal stem cell marker for multipotency.* Stem Cells Transl Med. **4** (2015).

[13] G. Hollway and P. Currie, *Myotome meanderings. cellular morphogenesis and the making of muscle.* EMBO Rep **9** (2003).

[14] G. Shefer, M. Wleklinski-Lee, and Z. Yablonka-Reuveni, *Skeletal muscle satellite cells can spontaneously enter an alternative mesenchymal pathway,* Cell Science **117** (2004).

[15] J. D. Starkey, M. Yamamoto, S. Yamamoto, and D. J. Goldhamer, *Skeletal muscle satellite cells are committed to myogenesis and do not spontaneously adopt nonmyogenic fates,* Journal of Histochemistry and Cytochemistry **59** (2011).

[16] E. Enwere, *Role of the signaling axis in the regulation of myogenesis and muscle homeostasis,* Front Immunol **5** (2014).

[17] M. I. Lefterova and M. A. Lazar, *New developments in adipogenesis,* Trends Endocrinol Metab **3** (2009).

[18] A. T. Ali, W. E. Hochfeld, R. Myburgh, and M. S. Pepper, *Adipocyte and adipogenesis,* European Journal of Cell Biology **92** (2013).

[19] Y. Deng and P. E. Scherer, *Adipokines as novel biomarkers and regulators of the metabolic syndrome,* Ann NY Acad. Sci **1** (2010).

[20] P. Macklin, M. E. Edgerton, A. M. Thompson, and V. Cristini, *Patient-calibrated agent-based modelling of ductal carcinoma in situ (dcis): From microscopic measurements to macroscopic predictions of clinical progression,* J. Theor. Biol. **301**, 122 (2012).

[21] F. J. Vermolen and A. Gefen, *A semi-stochastic cell-based formalism to model the dynamics of migration of cells in colonies,* Biomech Model Mechanobiol **11** (2012).

[22] M. Vable, Intermediate Mechanics of Materials (Oxford University Press, 2007).

[23] M. L. McCain, H. Yuan, F. S. Pasqualini, P. H. Campbell, and K. K. Parker, *Matrix elasticity regulates the optimal cardiac myocyte shape for contractility,* Am J Physiol Heart Circ Physiol **2014** (306).

[24] P. Bjorntorp and L. Sjostrom, Number and Size of Adipose Tissue Fat Cells in Relation to Metabolism in Human Obesity (Metabolism, 1971).

[25] X. Liang, A. L. Oldenburg, V. Crecea, S. Kalyanam, M. F. Insana, and S. A. Boppart, *Modeling and measurement of tissue elastic moduli using optical coherence elastography,* Optics in Tissue Engineering and Regenerative Medicine II **6858** (2008).

[26] M. Lopez-Garcia, D. Beebe, and W. Crone, *Young's modulus of collagen at slow displacement rates,* Bio-Medical Materials and Engineering **20** (2010).

[27] W. Boon, Incorporation of Contracture Formation during Dermal Wound Healing: a Mathematical Model (TU Delft, 2014).

[28] R. Enning, Contractile forces of myoblasts on functionalized micro-plates (Institute for Biomedical Engineering, 2006).

[29] N. E. Miller, C. C. Michel, and et. al., *Secretion of adipokines by human adipose tissue in vivo: partitioning between capillary and lymphatic transport,* Am J Physiol Endocrinol Metab **301** (2011).

[30] R. M. Ford and D. A. Lauffenburger, *Measurement of bacterial random motility and chemotaxis coefficients: Ii. application of single-cell-based mathematical model,* Biotechnology and Bioengineering **37** (1991).

[31] R. Van der Meijden, *Een semi-stochastisch cell-based model voor de ontwikkeling van een longcarcinoom,* (2013), bSc report.

[32] J. Van Kan, A. Segal, and F. J. Vermolen, Numerical Methods in Scientific Computing (VSSD, 2008).

[33] C. Vuik and D. Lahaye, Scientific Copmuting (WI4201) (TU Delft, 2012).

[34] O. Zienkiewicz and J. Zhu, *The superconvergent path recovery and a posteriori error estimates. part 1: The recovery technique.* International jounral for numerical methods in engineering **33** (1992).

[35] S. Ramanujan, *Modular equations and approximations to pi,* Quart. J. Pure App. Math. **45** (1914).